이학박사학위논문

Implementation of Comprehensive Cloud Microphysics in Global Climate Models

전지구기후모형에 포괄적인 구름미세물리과정의 접합

2017년 2월

서울대학교 대학원

지구환경과학부

안 민 섭

Abstract

Implementation of Comprehensive Cloud Microphysics in Global Climate Models

Min-Seop Ahn

School of Earth and Environmental Sciences

The Graduate School

Seoul National University

Implementation of comprehensive cloud microphysics in 50km resolution global climate models with appropriate vertical mixing is the main objective of this study. The comprehensive cloud microphysics was obtained from the Goddard Cumulus Ensemble (GCE) model which is a kind of Cloud Resolving Models (CRM). To implement the cloud microphysics to the global climate models, the resolution dependency of cloud microphysics was examined using CRM simulations with different resolutions, and it is improved by modifications of fractional saturation and terminal velocity.

Appropriate vertical mixing for 50km resolution global climate models was examined using General Circulation Model (GCM) simulations with different horizontal resolutions and a 3-dimensional CRM simulation. As the horizontal resolution of the GCM is increased, the resolved grid-scale vertical transport is increased. Accordingly, the sub-grid vertical transport parameterized by a convection scheme has to be decreased appropriately. Using the 3-dimensional CRM simulation with 1km horizontal resolution, the appropriate ratio of parameterized sub-grid scale vertical transport to total vertical transport is investigated as the horizontal resolution changes. The ratio obtained from the 3-dimensional CRM simulation is used as a guideline to decrease the parameterized sub-grid scale vertical transport in GCMs. The cumulus base mass flux is used as a control factor to decrease the parameterized sub-grid scale vertical transport.

The 50km global climate model with comprehensive cloud microphysics and appropriate vertical mixing was improved to simulate the vertical profiles of temperature and moisture, precipitation frequency as a function of precipitation strength, and Madden-Julian Oscillation (MJO). The MJO simulation diagnostics developed by MJO Working Group and the process-

oriented MJO simulation diagnostics developed by MJO Task Force were applied to developed model in this study and the model intercomparison with CMIP5 models was conducted. The developed model relatively well simulates the MJO propagation, the convective-moisture coupling and the longwave radiation feedback processes.

Keywords:

High-resolution Global Climate Modeling, Global Climate Models, Cloud Resolving Models, Cloud Microphysics, Scale-Adaptive Parameterization, Madden-Julian Oscillation (MJO)

***Student Number*:** 2012-30894

Contents

List of figures

List of tables

1 Introduction

1.1 Backgrounds and motivation

The high impact weather on the human, such as typhoon and heavy precipitation, is hard to simulate in most current general circulation models (GCMs) because of its coarse resolution (Chen and Knutson 2008, Wehner et al. 2010, Boyle and Klein 2010) and imperfect physics parameterization (Lorant et al. 2006, Wilcox and Donner 2007, DeMott et al. 2007). The next generation GCMs must have a high resolution and appropriate physical parameterization for high resolution. In the high resolution GCMs, portion of the resolved grid-scale precipitation process (large-scale condensation) becomes lager and the parameterized sub-grid scale precipitation process (convective precipitation) becomes smaller. Therefore, implementation of cloud microphysics of cloud resolving model (CRM) and reduction of convective parameterization should be appropriated for next generation high resolution GCMs.

Grabowski (2001) developed the multi-scale modeling framework (MMF) that is a GCM with a two-dimensional CRM physics in place of a conventional parameterization. The MMF shows that the improvements of the MJO

simulation (Benedict and Randall 2009, Zhu et al. 2009) and the frequency of heavy precipitation (Iorio et al. 2004, DeMott et al 2007, Li et al. 2012) when compared to those of the GCM with a conventional parameterization. The limitation of MMF is a lack of interaction between clouds represented by embedded CRM and the adjacent GCM grids.

Satoh et al. (2005) developed the global CRM. It is conducted a 3.5-km resolution global simulation using the nonhydrostatic icosahedral atmospheric model. The model successfully reproduces the eastward propagation of the observed MJO (Miura et al. 2007, Liu et al. 2009) and typhoon genesis (Oouchi et al. 2009). However, these approach is computationally two or three order of magnitude more expensive than that of a conventional GCM.

Kang et al. (2015) developed the 50km resolution GCM with CRM cloud microphysics. They removed deep convection scheme and added diffusion-type non-precipitating shallow convection scheme, and replaced the large-scale condensation scheme by cloud microphysics of CRM. Based on the CRM simulations with different horizontal resolutions, the cloud microphysics is modified to overcome the resolution dependency problems of cloud microphysics. The 50km resolution GCM with CRM cloud microphysics shows

improvement of simulation in the precipitation frequency, especially in the heavy precipitation. Kang et al. (2016) also showed that the developed model simulates the MJO propagation reasonably well compared to the model with conventional parameterization.

1.2 Objectives and research strategies

This study is aimed to develop the 50km resolution global climate models with comprehensive cloud microphysics and appropriate vertical mixing. The research strategies are described below:

1) Resolution dependency of CRM cloud microphysics

The CRM is developed to simulate the mesoscale cloud system, thus their horizontal resolution is the order of 1km. For the implementation of CRM cloud microphysics to the 50km GCM, the resolution dependency of cloud microphysics must be improved. In this study, the resolution dependency of cloud microphysics is identified using CRM simulations with different horizontal resolution (1km, 5km, 10km, 50km) and several modifications are applied to improve the resolution dependency of cloud microphysics. The RH

criteria for condensation and the terminal velocity are key parameters to improve the resolution dependency of cloud microphysics.

2) Optimal parameter of cloud microphysics in 50km GCM

Based on experiments of 50km GCM with CRM cloud microphysics developed by Kang et al. (2015), the sub-time scale of cloud microphysics, RH criteria for condensation, and terminal velocity are found as the key parameters of cloud microphysics in GCM to control the precipitation rate, precipitation spatial pattern, vertical profile of hydrometeor, and Madden-Julian oscillation (MJO) simulation. The optimal parameter of cloud microphysics in 50km GCM is found using intensive experiments.

3) Optimal parameterization of vertical mixing that appropriated to 50km

The 50km resolution GCM with CRM cloud microphysics developed by Kang et al. (2015) improves the simulation of vertical profile of hydrometeors with including diffusion-type non-precipitating shallow convection scheme. But, the vertical profile of moisture is still concentrated in the low-level compared to observations. It indicates that more additional vertical mixing like

a deep convection is required. Because many conventional deep convection schemes are developed for the low resolution GCMs, order of a hundred resolutions, the conventional deep convection scheme must be modified to apply to the 50km resolution GCM. Using the 3-dimensional CRM experiment with 1km horizontal resolution, the scale-adaptive deep convection scheme is developed.

4) 6 hydrometeors-radiation interaction

Conventional GCM contains 3 hydrometeors (water vapor, cloud liquid water, cloud ice water), but GCM with CRM cloud microphysics contains 6 hydrometeors (water vapor, cloud liquid water, cloud ice water, rain, snow, graupel). Therefore, the 6 hydrometeors-radiation interaction is implemented based on CRM radiation scheme.

5) Coupled GCM with cloud microphysics

The final goal of this study is development of a coupled GCM with comprehensive cloud microphysics. Based on understanding of cloud microphysics in AGCM, the CRM cloud microphysics is implemented in coupled GCM.

2 Model description

2.1 SNUAGCM (Seoul National University AGCM)

The Atmospheric General Circulation Model (AGCM) used in this study is the Seoul National University AGCM (SNUAGCM). The model has a finite volume dynamical core (Lin 2004) with a hybrid sigma-pressure vertical coordinate. The model is represented at 50km horizontal resolution and 20 vertical levels. The deep convection scheme is based on a bulk mass flux scheme developed by Kim and Kang (2012) and a cumulus momentum transports (Kim et al. 2008). Cumulus cloudiness and cumulus cloud water are simply estimated as a function of cumulus updraft mass flux. The large-scale condensation scheme consists of a prognostic microphysics parameterization for total cloud liquid water (Le Treut and Li 1991) with a diagnostic cloud fraction parameterization. This scheme converts the relative humidity exceeding 75% to precipitation with a certain relaxation time scale 3600s. A non-precipitating diffusion-type shallow convection scheme (Tiedtke 1984) is also implemented in the model for the mid-tropospheric moist convection. The

boundary layer scheme is a non-local diffusion scheme based on Holtslag and Boville (1993). Atmospheric radiation processes are parameterized by a two-stream k distribution scheme as in Nakajima et al. (1995). The land surface processes use the land surface model (Bonan 1996). Other details of the model physics are described in Kang et al. (2015).

2.2 SNUCGCM (Seoul National University coupled GCM)

The Atmosphere-Ocean coupled GCM (CGCM) used in this study is the Seoul National University CGCM (SNUCGCM). The atmospheric component is SNU AGCM with 50km horizontal resolution. The oceanic component is version 2.2 of MOM2 Ocean GCM developed at Geophysical Fluid Dynamic Laboratory. The model is a finite difference treatment of the primitive equations of motion using the Boussinesq and hydrostatic approximation in spherical coordinates. The model domain includes most global oceans and the coastline and bottom topography are realistic. The zonal resolution is 1.0 degrees, and the meridional grid spacing is 1/3 between 8S and 8N, gradually increasing to 3.0 at 30S and 30N and fixed at 3.0 in the extratropics. There are

32 vertical levels with 23 levels in the upper 450m. The model uses Noh and Kim (1999) mixed layer model for vertical diffusion to improve the climatological vertical structure of the upper ocean. This scheme is based on Mellor and Yamada scheme (Noh and Kim 1999). The major distinguish of this scheme is that role of vertical shear production on diffusive mixing is considered unimportant but turbulent kinetic energy (TKE) flux plays an important role determining vertical diffusion. Therefore, the Richardson number which is important parameter for eddy diffusivity is dependent on turbulent kinetic energy (TKE), instead of vertical temperature shear.

In this model, to further reduce coupled model biases, diurnal coupling (2-hour air-sea coupling) is recently implemented (Ham et al. 2010, Danabasoglu et al. 2006, Bernie et al. 2008). Two component models exchange SST, wind stress, freshwater flux, long wave and shortwave radiation, and turbulent fluxes of sensible and latent heat. Any flux correction is not applied.

2.3 GCE (Goddard Cumulus Ensemble) Model

The Cloud Resolving Model (CRM) used in this study for implementing

cloud microphysics to a GCM is the Goddard Cumulus Ensemble (GCE) model developed at the National Aeronautic Space Administration/Goddard Space Flight Center (Tao 1993; 2003). The governing equation of the GCE model is non-hydrostatic that vertical and horizontal scales are appropriate to simulate the convection explicitly. The GCE model allows the gravity wave that triggers clouds and can simulate the growth, mature and decay process (life cycle) of clouds. The GCE model is organized by the process of dynamical core, microphysics, radiation, surface flux and sub-grid turbulence scheme.

The GCE model uses the compressible equations (Klemp and Wilhelmson 1978) with periodic lateral boundary conditions. Besides basic prognostic variables (u, v, w, θ, q_v), GCE has prognostic equations for cloud liquid water, cloud ice water, rain, snow and graupel. Those equations contain microphysical transfers between hydrometeor species, advection of species by large scale motions and linkage to the thermodynamics and moisture equations by a phase change between species, such as condensation, deposition, accretion, autoconversion, melting, freezing, evaporation, sublimation, etc.

The GCE model has been used to investigate the interactions of clouds

with each other cloud (Tao and Simpson 1984, Tao and Simpson 1989), with their surroundings (Tao and Soong 1986), with long wave radiative transfer processes (Tao et al. 1991), with ocean surfaces (Tao et al. 1991, Lau et al. 1993), and with trace gas distributions (Scala et al. 1990).

3 Cloud microphysics of the GCE

3.1 Description of GCE cloud microphysics

The description of GCE cloud microphysics is mainly contributed by Ildae Choi who introduced the GCE model from the NASA and made a model description. The GCE cloud microphysics includes a parameterized Kessler-type two-category liquid water scheme (cloud water and rain), and three-category ice-phase schemes (cloud ice, snow and graupel) mainly based on Lin et al. (1983) and Rutledge and Hobbs (1983, 1984). The cloud microphysics of GCE used in this study is bulk type single moment scheme. The cloud microphysical processes are formulated based on integration of all size droplets, and the shapes of liquid and ice are assumed to be spherical. Size distributions of rain, snow and graupel are taken to be inverse-exponential with to diameter (D) such that $N(D) = N_0 \exp(-\lambda D)$, where $N(D)$ is the number of drops of diameter between D and $D + \delta D$ in unit volume of space, N_0 is the value of $N(D)$ for $D = 0$ (called intercept parameter), and

$\lambda = \left(\frac{\pi \rho_x N_0}{\rho q_x} \right)^{0.25}$ is the slope of the particle size distribution. The density and mixing ratio of the hydrometeors are ρ_x and q_x, respectively. The dominant cloud microphysics are described below:

1) Autoconversion

The autoconversion is growing process of liquid/ice particles by collision between each other liquid/ice particle. For example, cloud liquid/ice water can be grown to rain/snow droplets by autoconversion. Rutledge and Hobbs (1983, 1984) represents this process using observed criteria value of autoconversion.

$$\mathbf{P_{RAUT}} = 10^{-3} \times \left(\mathbf{q_c} - \left(1.5 \times 10^{-3} \right) \right)$$

$$\mathbf{P_{SAUT}} = 10^{-3} \times \exp\left(0.025 \times \left(\mathbf{T_{air}} - \mathbf{T_0} \right) \right) \times \left(\mathbf{q_i} - \left(6 \times 10^{-4} \right) \times \left(\frac{\boldsymbol{\rho}_0}{\boldsymbol{\rho}} \right) \right)$$

Where $\mathbf{P_{RAUT}}$ and $\mathbf{P_{SAUT}}$ indicate the autoconversion of cloud liquid water and cloud ice water to rain droplets and snow droplets, $\mathbf{q_c}$ and $\mathbf{q_i}$ are mixing ratio of cloud liquid water and cloud ice water, $\mathbf{T_{air}}$ is air temperature, $\mathbf{T_0}$ is melting temperature (273.16K), $\boldsymbol{\rho}$ is air density, $\boldsymbol{\rho}_0$ is surface air density.

2) Accretion

The accretion is growing process of falling cloud droplets by capturing environmental liquid/ice particles. For example, falling rain droplets can be grown by capturing environmental cloud liquid water. Rutledge and Hobbs (1983) represents this process using observed terminal velocity of rain droplets.

$$\mathbf{P_{RACW}} = \frac{\pi}{4}\mathbf{q_c}\mathbf{E_{RW}}\mathbf{n_{0R}}\left(\frac{\rho_0}{\rho}\right)^{1/2}\left[\frac{\mathbf{a_0}\Gamma(3)}{\lambda_R^3}+\frac{\mathbf{a_1}\Gamma(4)}{\lambda_R^4}+\frac{\mathbf{a_2}\Gamma(5)}{\lambda_R^5}+\frac{\mathbf{a_3}\Gamma(6)}{\lambda_R^6}\right]$$

where $\mathbf{P_{RACW}}$ indicates the growth of rain droplets by the accretion of cloud liquid particles, $\mathbf{q_c}$ is mixing ratio of cloud liquid water, $\mathbf{E_{RW}}$ is collection coefficient, $\mathbf{n_{0R}}$ is intercept parameter of the raindrop size distribution, $\boldsymbol{\rho}$ is air density, $\boldsymbol{\rho}_0$ is surface air density, $\mathbf{a}_0$ - $\mathbf{a}_3$ are coefficient in polynomial terminal velocity relation for rain, Γ is Gamma function, $\boldsymbol{\lambda}_\mathbf{R}$ is slope of raindrop size distribution. Beside the $\mathbf{P_{RACW}}$, other accretion processes are represented as similar form with $\mathbf{P_{RACW}}$.

3) Evaporation and Sublimation

The evaporation and sublimation are conversion process of rain droplets

and snow/graupel droplets into water vapor with temperature change. Rutledge and Hobbs (1983, 1984) represents this process using the saturation ratio, ventilation factor, etc.

$$\mathbf{P_{REVP}} = \frac{2\pi \mathbf{N_{0R}}(\mathbf{S}-1)}{\boldsymbol{\rho}} \times \left[\frac{\mathbf{L_v}}{\mathbf{K_a T}} \left(\frac{\mathbf{L_v M_w}}{\mathbf{R^* T}} - 1 \right) + \frac{\mathbf{R^* T}}{\boldsymbol{\psi_d} \mathbf{M_w e_s(T)}} \right]^{-1} \times \left[0.78 \times \frac{\Gamma(2)}{\boldsymbol{\lambda}_\mathbf{R}^2} + 0.31 \times \left(\frac{\mathbf{a'}\boldsymbol{\rho}}{\boldsymbol{\mu}} \right) \times \left(\frac{\boldsymbol{\rho}_0}{\boldsymbol{\rho}} \right)^{1/4} \times \frac{\Gamma(3)}{\boldsymbol{\lambda}_\mathbf{R}^3} \right]$$

Where $\mathbf{P_{REVP}}$ indicates evaporation process of rain droplets, $\mathbf{N_{0R}}$ is Intercept parameter of the raindrop size distribution (0.08 cm^{-4}), $\mathbf{S}$ is saturation ratio, $\boldsymbol{\rho}$ is air density, $\boldsymbol{\rho}_0$ is surface air density, $\mathbf{L_v}$ is Latent heat of vaporization (2.5×10^{10} erg g^{-1}), $\mathbf{K_a}$ is thermal conductivity ($2.43 \times 10^3\ erg\ cm^{-1}s^{-1}\ K^{-1}$), $\mathbf{T}$ is air temperature, $\mathbf{M_w}$ is molecular weight of water (18.016 g mol^{-1}), $\mathbf{R^*}$ is universal gas constant (8.314×10^7 erg mol^{-1} K^{-1}), $\boldsymbol{\psi_d}$ is diffusivity of water vapor in air ($0.226\ cm^2\ s^{-1}$), $\mathbf{e_s(T)}$ is saturated vapor pressure at given air temperature, Γ is Gamma function, $\boldsymbol{\lambda_R}$ is slope of raindrop size distribution, $\mathbf{a'}$ is Constant in empirical formula for fall speed ($3x10^3$ s^{-1}), $\boldsymbol{\mu}$ is dynamic viscosity ($1.718 \times 10^{-4}\ g\ cm^{-1}\ s^{-1}$).

4) Melting and Freezing

The melting and freezing are state change process between water and ice. Rutledge and Hobbs (1983) represents this process using the melting temperature, ventilation factor, thermal conductivity, etc.

$$\mathbf{P_{SMLT}} = \frac{2\pi \mathbf{N_{0S}}(\mathbf{T}-\mathbf{T_0})}{\mathbf{L_f}\boldsymbol{\rho}} \times \left[0.78 \times \frac{\Gamma(2)}{\boldsymbol{\lambda}_\mathbf{S}^2} + 0.31 \mathbf{S_c}^{1/3} \times \mathbf{c}^{1/2} \left(\frac{\boldsymbol{\rho}_0}{\boldsymbol{\rho}} \right)^{1/4} \boldsymbol{\nu}^{-1/2} \times \frac{\Gamma\left(\frac{5+\mathbf{d}}{2}\right)}{\boldsymbol{\lambda}_\mathbf{S}^{\frac{5+\mathbf{d}}{2}}} \right]$$

$$\mathbf{P_{GFR}} = \frac{1}{36}\pi^2 \mathbf{B'} \mathbf{N_{0R}} \left(\frac{\boldsymbol{\rho}_\mathbf{w}}{\boldsymbol{\rho}} \right) \{\exp[\mathbf{A'}(\mathbf{T_0}-\mathbf{T})]-1\} \frac{\Gamma(7)}{\boldsymbol{\lambda}_\mathbf{R}^7}$$

Where $\mathbf{P_{SMLT}}$ and $\mathbf{P_{GFR}}$ indicate melting of snow droplets and freezing of rain droplets, $\mathbf{N_{0S}}$ is Intercept parameter of the snowflake size distribution (0.16 cm^{-4}), $\mathbf{T}$ is air temperature, $\mathbf{T_0}$ is melting temperature (273.16K), $\mathbf{L_f}$ is Latent heat of fusion (3.336×10^9 erg g^{-1}), $\boldsymbol{\rho}$ is air density, Γ is Gamma function, $\boldsymbol{\lambda_S}$ is slope of snowflake size distribution, $\mathbf{S_c}$ is Schmidt number $(=\boldsymbol{\nu}/\boldsymbol{\psi})$, $\boldsymbol{\nu}$ is kinematic viscosity $(=\boldsymbol{\mu}/\boldsymbol{\rho})$, $\boldsymbol{\mu}$ is dynamic viscosity ($1.718\times10^{-4}\ g\ cm^{-1}\ s^{-1}$), $\boldsymbol{\psi}$ is diffusivity, $\mathbf{c}$ and $\mathbf{d}$ are Constant in empirical formula for fall speed (78.63 $cm^{1-d}\ s^{-1}$ and 0.11), $\mathbf{A'}$ and $\mathbf{B'}$ are empirical

constant ($0.66K^{-1}$ and $10^{-4}\ cm^{-3}\ s^{-1}$), $\mathbf{N_{0R}}$ is Intercept parameter of the raindrop size distribution (0.08 cm^{-4}), $\boldsymbol{\rho_w}$ is density of water (1.0 g cm^{-3}), $\boldsymbol{\lambda_R}$ is slope of raindrop size distribution.

5) Bergeron-Findeisen process

The Bergeron-Findeisen process is growing process of ice particles by autoconversion of cloud liquid/ice particles. This process is represented using observed time scale of ice particle growth, mass, number concentration, terminal velocity, etc.

$$\mathbf{P_{SFW}} = \mathbf{N_{I50}}\left(\mathbf{a_1 m_{I50}^{a_2}} + \boldsymbol{\pi} \mathbf{E_{IW}} \boldsymbol{\rho} \mathbf{q_c} \mathbf{R_{I50}^2} \mathbf{U_{I50}}\right)$$

$$\mathbf{P_{SFI}} = \mathbf{q_i} \Big/ \boldsymbol{\Delta} \mathbf{t_1}$$

Where $\mathbf{P_{SFW}}$ and $\mathbf{P_{SFI}}$ indicate the Bergeron-Findeisen process by autoconversion of cloud liquid and ice particles, $\mathbf{N_{I50}}$ is number concentration of hypothetical 50 μm size ice crystal (g^{-1}), $\mathbf{m_{I50}}$ is mass of a hypothetical 50 μm size ice crystal (3.84×10^{-6}g), $\mathbf{R_{I50}}$ is radius of hypothetical ice crystal ($2\times5\times10^{-3}$cm), $\mathbf{U_{I50}}$ is terminal velocity of hypothetical ice crystal

(100cm s^{-1}), $\mathbf{a}_1$ and $\mathbf{a}_2$ are temperature-dependent parameters in the Bergeron process, $\mathbf{E_{IW}}$ is collection efficiency of cloud ice for cloud water (approximate to 1), $\boldsymbol{\rho}$ is air density, $\mathbf{q_c}$ and $\mathbf{q_i}$ are mixing ratio of cloud liquid water and cloud ice water, $\Delta \mathbf{t}_1$ is the time needed for a crystal to grow from 40 to 50 μm.

3.2 Resolution dependency of cloud microphysics

The resolution dependency of cloud microphysics is examined using GCE simulation with 1km, 5km, 10km, and 50km horizontal resolutions, which is mainly conducted by Yang (2014). This study succeeds the framework of Yang (2014) and more develops it. Figure 3.1. (a) shows that the specific humidity in middle-level becomes smaller and the specific humidity in low-level becomes larger as the horizontal resolution becomes coarse. It indicates that the vertical transport of specific humidity by grid-mean upward motion becomes smaller as the horizontal resolution becomes coarse. Figure 3.1. (b) shows that the vertical velocity over all vertical levels becomes weaker as the horizontal resolution becomes coarse.

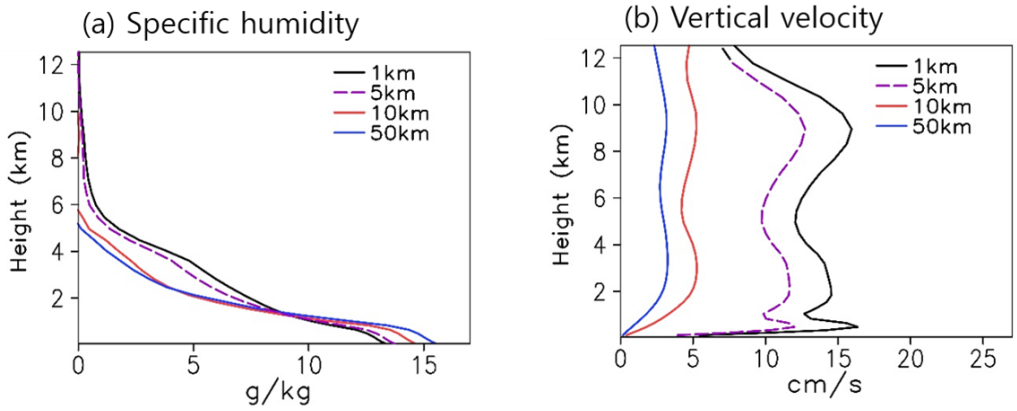

Figure 3.1. Vertical profiles of domain averaged (a) specific humidity and (b) vertical velocity from the CRM with 1km, 5km, 10km, and 50km resolutions. The vertical velocity is averaged by using the grid where vertical velocity is positive.

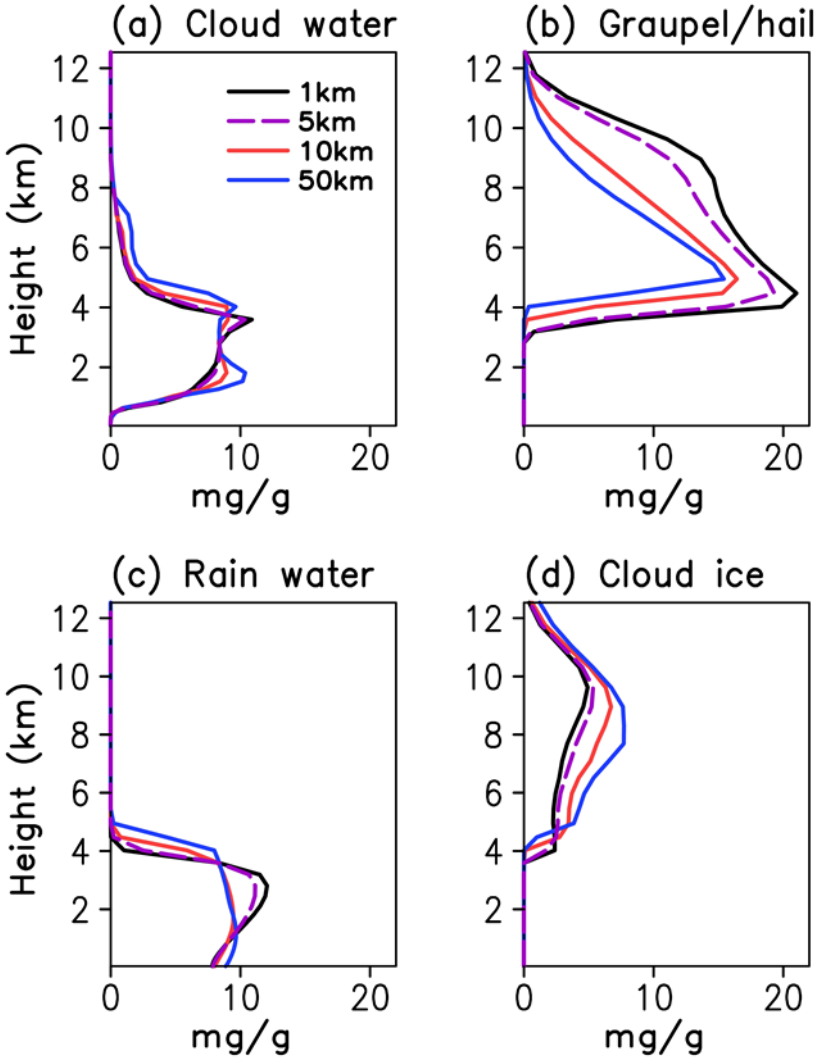

Figure 3.2. Vertical profiles of domain averaged (a) cloud liquid water, (b) graupel/hail, (c) rain water, and (d) cloud ice water from the CRM with 1km, 5km, 10km, and 50km resolutions.

The vertical profiles of cloud water, graupel/hail, rain water, and cloud ice from the different horizontal resolutions are shown in Fig. 3.2. Among the hydrometeors, larger horizontal resolution dependency is appeared in the graupel/hail. Figure 3.1. (b) showed that vertical velocity becomes smaller as the horizontal resolution becomes coarse. Because of the horizontal resolution dependency of the vertical velocity, the processes related with vertical velocity should be modified appropriated for the 50km GCM with GCE cloud microphysics. Figure 3.3 shows the vertical profiles of the accretion of cloud water by rain water, accretion of cloud water by graupel, melting of graupel, and condensation from the different horizontal resolutions. As the horizontal resolution becomes coarse, most cloud microphysics processes become smaller, especially in the accretion and condensation processes.

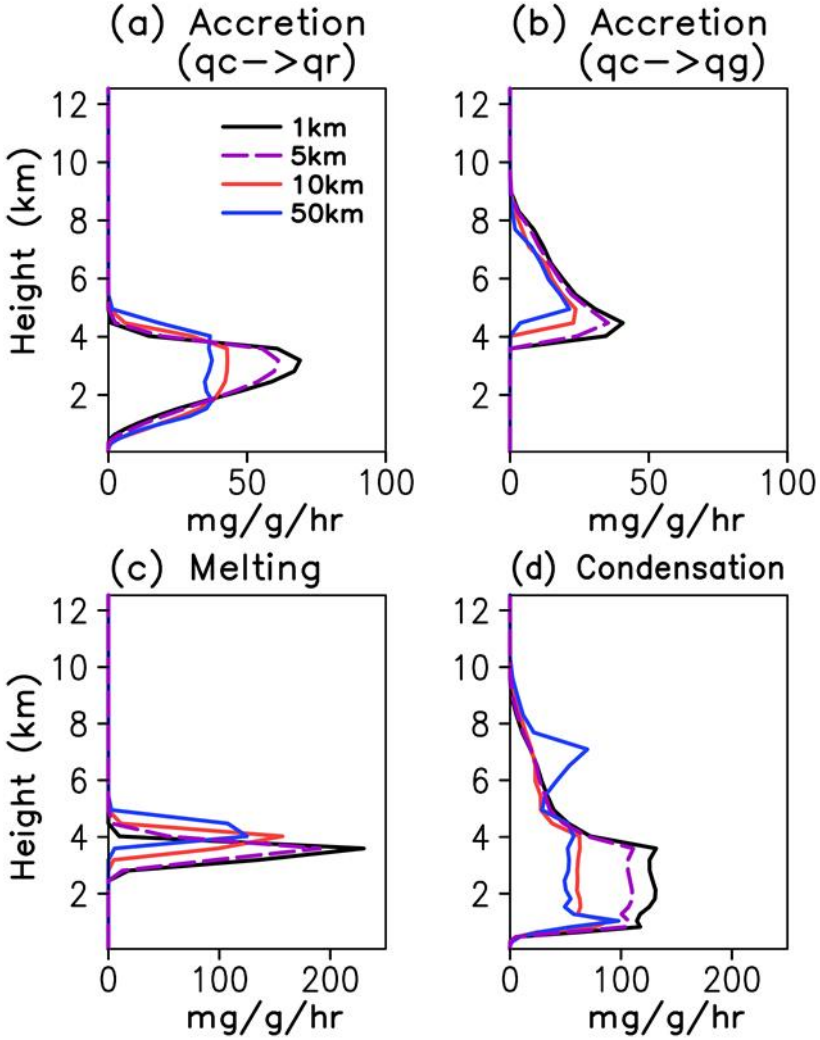

Figure 3.3. Vertical profiles of domain averaged cloud microphysical processes from the CRM with 1km, 5km, 10km, and 50km resolutions. (a) accretion of cloud water by rain water, (b) accretion of cloud water by graupel, (c) melting of graupel, and (d) condensation.

3.3 Improvement of resolution dependency for cloud microphysics

The improvement of resolution dependency for cloud microphysics is mainly conducted by Yang (2014) and Kang et al. (2015). In the 50km horizontal resolution, the sub-grid fractional condensation is required because the grid-mean RH is rarely exceeded 100%. The sub-grid fractional condensation concept is adapted from Le Treut and Li (1991). Figure 3.4 shows the vertical profiles of cloud microphysics processes like the figure 3.3, but for the 1km resolution, 50km resolution, and 50km resolution with modification of condensation RH criteria. As the condensation RH criteria becomes smaller, the 50km resolution with modification becomes similar to 1km resolution in the accretion of cloud water by rain water, the accretion of cloud water by graupel, and the condensation processes.

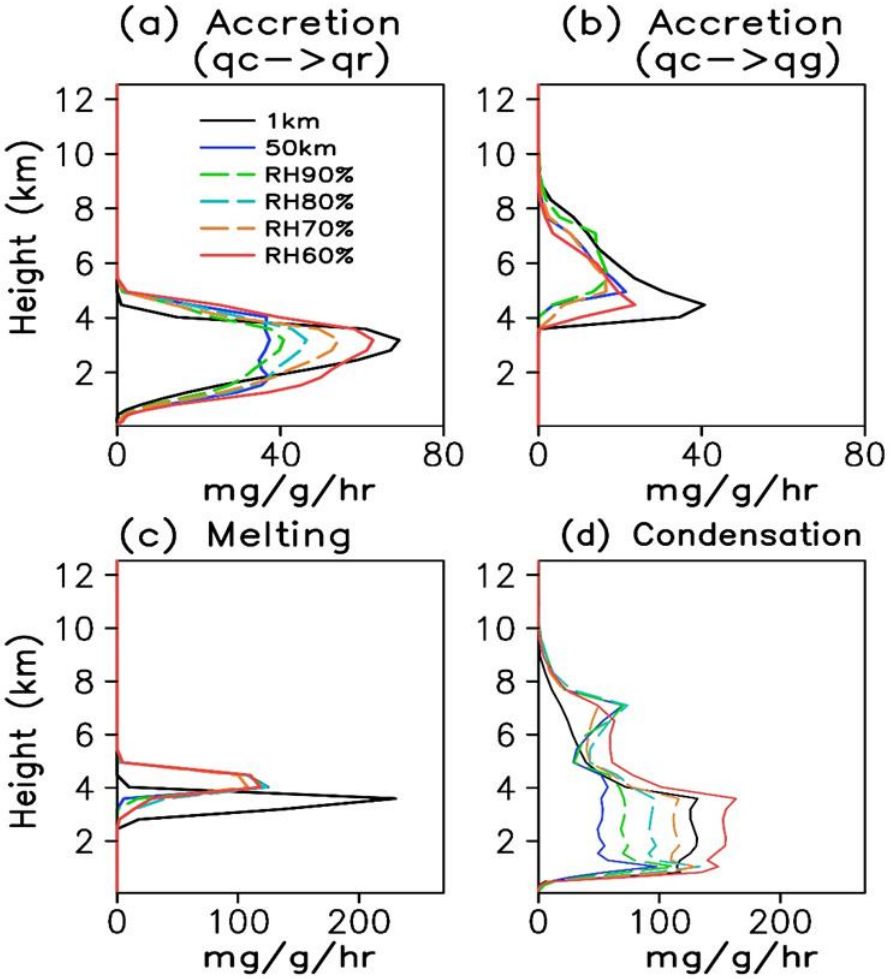

Figure 3.4. Vertical profiles of domain averaged cloud microphysical processes from the CRM with 1km horizontal resolution (black solid line), 50km horizontal resolution (blue solid line), and modified 50km horizontal resolution with different condensation RH criteria (different color dashed line). (a) accretion of cloud water by rain water, (b) accretion of cloud water by graupel, (c) melting of graupel, and (d) condensation.

In the 50km horizontal resolution, a reduction of terminal velocity is required because the terminal velocity should be balanced with grid-mean vertical velocity which is reduced in coarse resolution. Figure 3.5 shows the vertical profiles of cloud microphysics processes like the figure 3.3, but for the 1km resolution, 50km resolution, and 50km resolution with reduced terminal velocity. As the terminal velocity is reduced more strongly, the 50km resolution with reduced terminal velocity becomes similar to 1km resolution in the accretion of cloud water by rain water and the accretion of cloud water by graupel. However, the validity of reduction of terminal velocity is needed to more examine because mesoscale models usually do not modify the terminal velocity.

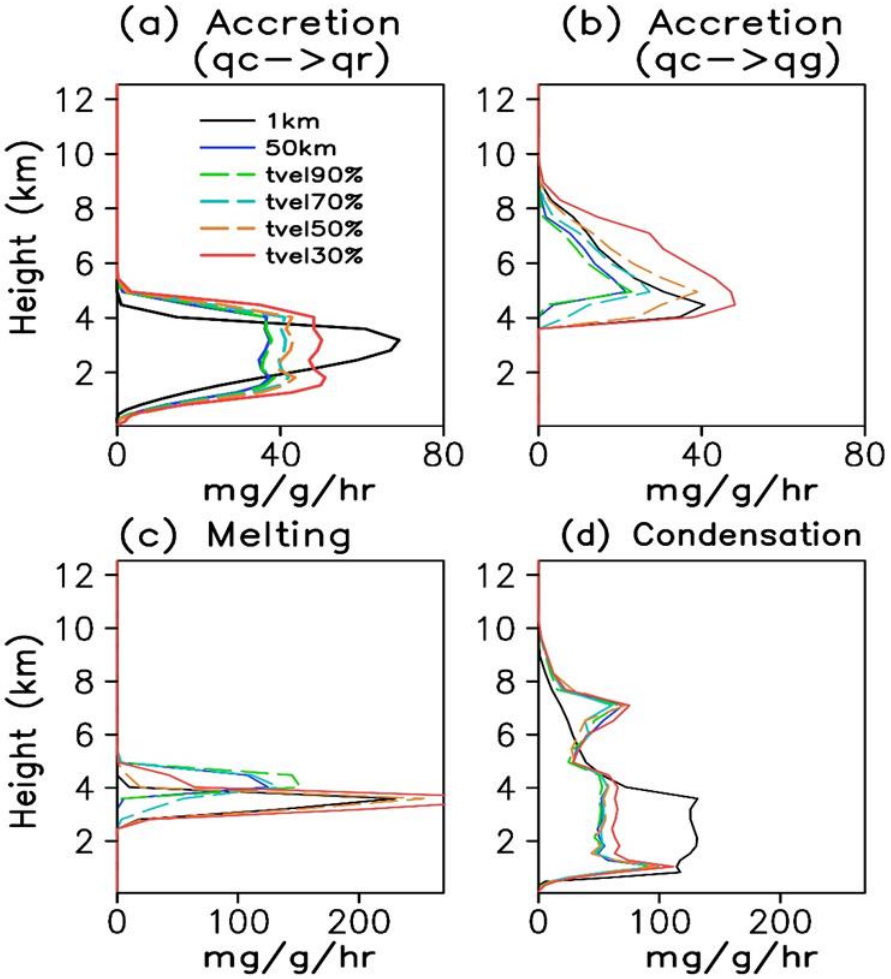

Figure 3.5. Vertical profiles of domain averaged cloud microphysical processes from the CRM with 1km horizontal resolution (black solid line), 50km horizontal resolution (blue solid line), and modified 50km horizontal resolution with different reduction of terminal velocity (different color dashed line). (a) accretion of cloud water by rain water, (b) accretion of cloud water by graupel, (c) melting of graupel, and (d) condensation.

To improve the resolution dependency of cloud microphysics, both of the modifications for the condensation RH criteria and the terminal velocity are considered. Figure 3.6 shows the vertical profiles of cloud water, graupel/hail, rain water, and cloud ice from the 1km resolution, 50km resolution, and 50km resolution with modification of condensation RH criteria 75% and reduced terminal velocity by 50%. The 50km resolution with both modifications is similar to 1km resolution in simulation of hydrometeors.

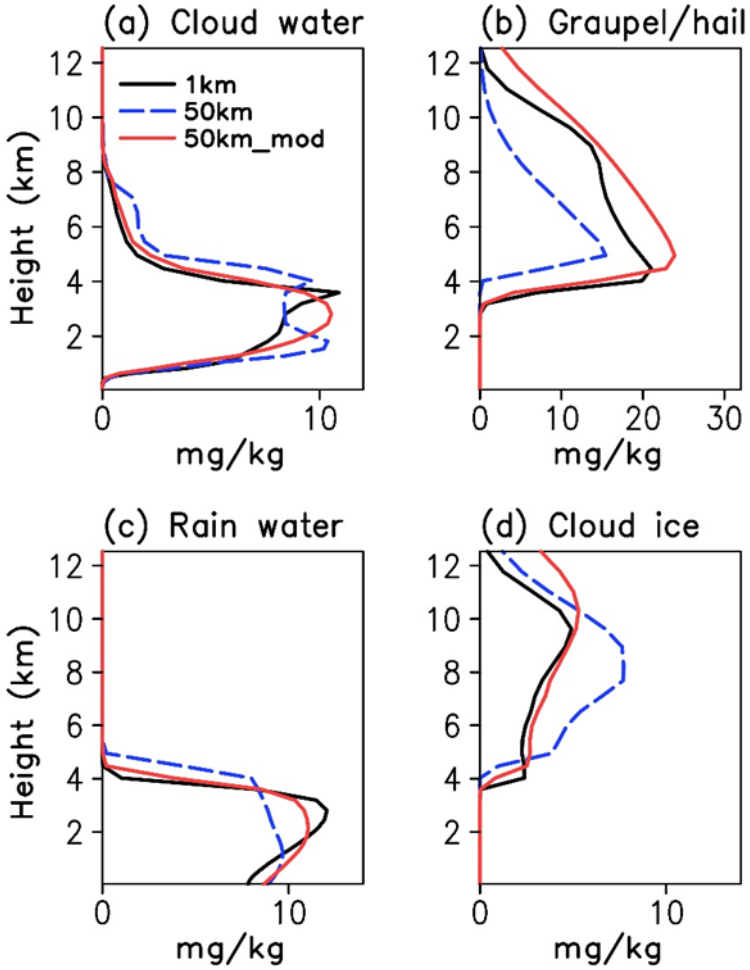

Figure 3.6. Vertical profiles of domain averaged (a) cloud liquid water, (b) graupel/hail, (c) rain water, and (d) cloud ice water from the CRM with 1km horizontal resolution (black solid line), 50km horizontal resolution (blue dashed line), and modified 50km horizontal resolution with condensation RH criteria 75% and terminal velocity 50% (red solid line).

To examine which cloud microphysical processes are influenced by the both modifications, vertical profile of each cloud microphysical process is examined. Figure 3.7 shows the vertical profiles of cloud microphysics processes like the figure 3.3, but for the 1km resolution, 50km resolution, and 50km resolution with modification of condensation RH criteria 75% and reduced terminal velocity by 50%. The 50km resolution with modification is similar to 1km resolution in simulation of accretion, melting, and condensation. Based on this results, the modifications of condensation RH criteria and terminal velocity reduction are applied to GCM with comprehensive cloud microphysics.

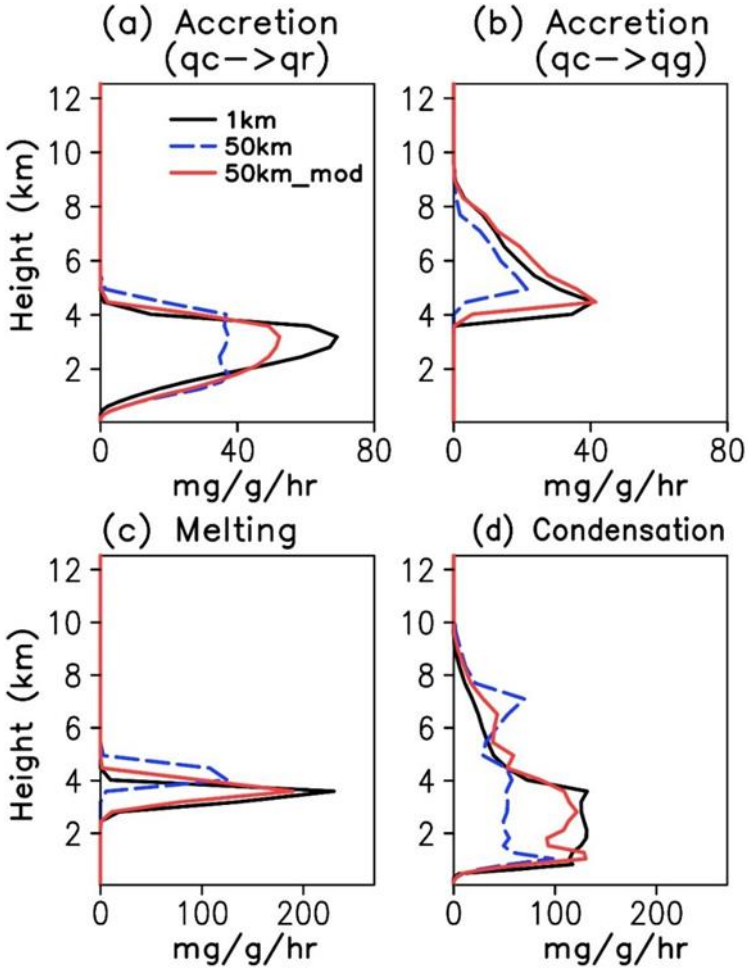

Figure 3.7. Vertical profiles of domain averaged cloud microphysical processes from the CRM with 1km horizontal resolution (black solid line), 50km horizontal resolution (blue dashed line), and modified 50km horizontal resolution with condensation RH criteria 75% and terminal velocity 50% (red solid line). (a) accretion of cloud water by rain water, (b) accretion of cloud water by graupel, (c) melting of graupel, and (d) condensation.

4 Implementation of GCE cloud microphysics in 50km resolution GCM

4.1 50km GCM with modified cloud microphysics

The implementation of comprehensive cloud microphysics in 50km resolution GCM is carried out by Kang et al. (2015) for the first time and it is more developed by Kang et al. (2016) and this study. In the 50km resolution GCM, the deep convection and large-scale condensation are replaced by modified cloud microphysics as the schematic diagram of Fig.4.1. For the calculation of cloud microphysical processes appropriately, the calculation time step is required a smaller value rather than other GCM processes like advection, sub-grid vertical transport, and radiation. Therefore, the 50km resolution GCM with modified cloud microphysics used a 300s sub-time step for the cloud microphysics and a 1800s time step for the other processes in Kang et al. (2015). However, Kang et al. (2016) used same small time step of 900s for the cloud microphysics and the other processes for the more consistency.

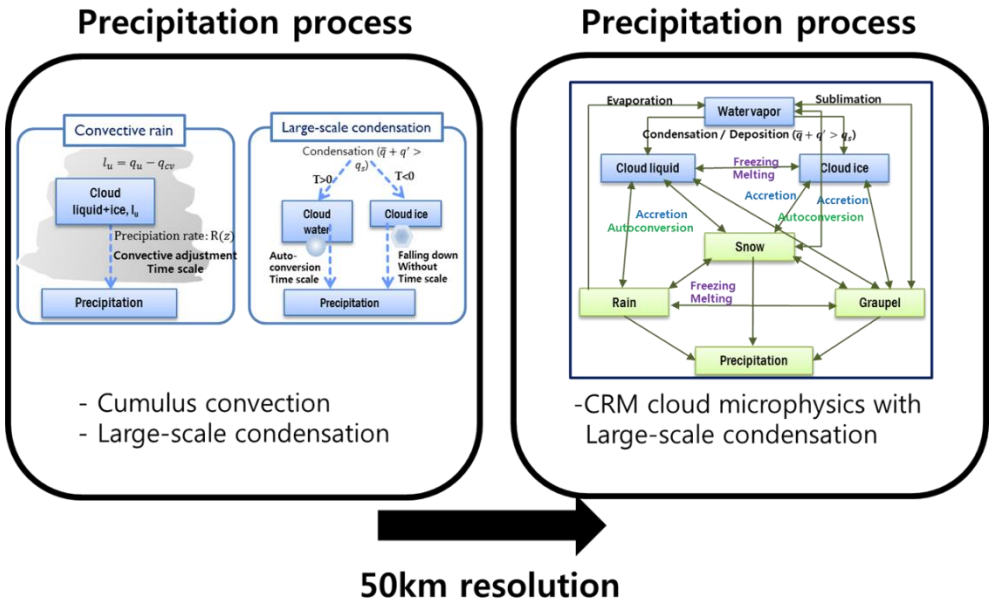

Figure 4.1. Schematic diagram for implementation of CRM cloud microphysics to 50km resolution GCM. Left panel is precipitation process of conventional GCM, and right panel is precipitation process of 50km resolution GCM with CRM cloud microphysics.

The governing equations for a thermodynamic and hydrometeors (water vapor and cloud water) in a conventional GCM are described as below.

$$\frac{d\overline{T}}{dt} = -\frac{\partial}{\partial p}\left(\overline{\omega' T'}\right) + \left[\frac{L_v}{C_p}\left(\overline{c} - \overline{e}\right)\right] + Q_R$$

$$\frac{d\overline{q_v}}{dt} = -\frac{\partial}{\partial p}\left(\overline{\omega' q_v'}\right) - \left(\overline{c} - \overline{e}\right)$$

$$\frac{d\overline{q_c}}{dt} = -\frac{\partial}{\partial p}\left(\overline{\omega' q_c'}\right) + \left(\overline{c} - \overline{e}\right)$$

where T, q_v, q_c indicate the air temperature, water vapor, and cloud water consisted of liquid and ice phase, respectively. ω indicates the pressure velocity. c and e indicate the condensation and evaporation. Q_R indicates the radiative heating. C_p and L_v indicate the specific heat and latent heat. Overbar indicates grid-mean.

On the other hand, the governing equations for a thermodynamic and hydrometeors in a GCM with comprehensive cloud microphysics contain more hydrometeors (water vapor, cloud liquid water, cloud ice water, rain, snow, and graupel) and cloud microphysical processes as below.

$$\frac{d\overline{T}}{dt} = -\frac{\partial}{\partial p}(\overline{\omega' T'}) + \left[\frac{L_v}{C_p}(\overline{c} - \overline{e_l}) + \frac{L_s}{C_p}(\overline{d_l} + \overline{d_s} + \overline{d_g} - \overline{s_l}) + \frac{L_f}{C_p}(\overline{f} - \overline{m})\right]$$

$$-\left[\frac{L_v}{C_p}\overline{e_r} + \frac{L_s}{C_p}(\overline{s_s} + \overline{s_g})\right] + Q_R$$

$$\frac{d\overline{q_v}}{dt} = -\frac{\partial}{\partial p}(\overline{\omega' q_v'}) - (\overline{c} + \overline{d_l} + \overline{d_s} + \overline{d_g} - \overline{e_l} - \overline{s_l}) + (\overline{e_r} + \overline{s_s} + \overline{s_g})$$

$$\frac{d\overline{q_l}}{dt} = -\frac{\partial}{\partial p}(\overline{\omega' q_l'}) + (\overline{c} - \overline{e_l}) + \overline{T_{ql}}$$

$$\frac{d\overline{q_l}}{dt} = -\frac{\partial}{\partial p}(\overline{\omega' q_l'}) + (\overline{d_l} - \overline{s_l}) + \overline{T_{ql}}$$

$$\frac{d\overline{q_r}}{dt} = -\frac{\partial}{\partial p}(\overline{\omega' q_r'}) - \overline{V_r}\frac{\partial \overline{q_r}}{\partial p} + (\overline{m_s} + \overline{m_g} - \overline{f_s} - \overline{f_g}) - \overline{e_r} + \overline{T_{qr}}$$

$$\frac{d\overline{q_s}}{dt} = -\frac{\partial}{\partial p}(\overline{\omega' q_s'}) - \overline{V_s}\frac{\partial \overline{q_s}}{\partial p} + (\overline{d_s} - \overline{m_s} + \overline{f_s}) - \overline{s_s} + \overline{T_{qs}}$$

$$\frac{d\overline{q_g}}{dt} = -\frac{\partial}{\partial p}(\overline{\omega' q_g'}) - \overline{V_g}\frac{\partial \overline{q_g}}{\partial p} + (\overline{d_g} - \overline{m_g} + \overline{f_g}) - \overline{s_g} + \overline{T_{qg}}$$

where T, q_v, q_l, q_i, q_r, q_s, q_g indicate the air temperature, water vapor, cloud liquid water, cloud ice water, rain, snow, graupel, respectively. ω indicates the pressure velocity. V_r, V_s, V_g indicate the terminal velocity for rain, snow, and graupel, respectively. c, d, e, s indicate the condensation, deposition, evaporation, and sublimation, respectively. f and m indicate the

freezing and melting. Q_R indicates the radiative heating. C_p, L_v, L_s, L_f indicate the specific heat and latent heat for vaporization, sublimation, and fusion, respectively. T_q indicates the phase change among hydrometeors. Overbar indicates grid-mean. Subscripts of cloud microphysical processes indicate each hydrometeor.

Figure 4.2 shows the spatial distribution of annual mean precipitation for the TRMM, GCM with original cloud microphysics, and GCM with modified cloud microphysics (RH criteria 75% and terminal velocity 50%). The GCM with original microphysics underestimated a simulation of precipitation in Indian Ocean, Western Pacific, and ITCZ. But, the GCM with modified cloud microphysics shows improvement of the precipitation simulation in Indian Ocean, Western Pacific, and ITCZ. It indicates that the comprehensive cloud microphysics improves the precipitation over the warm pool region in GCMs.

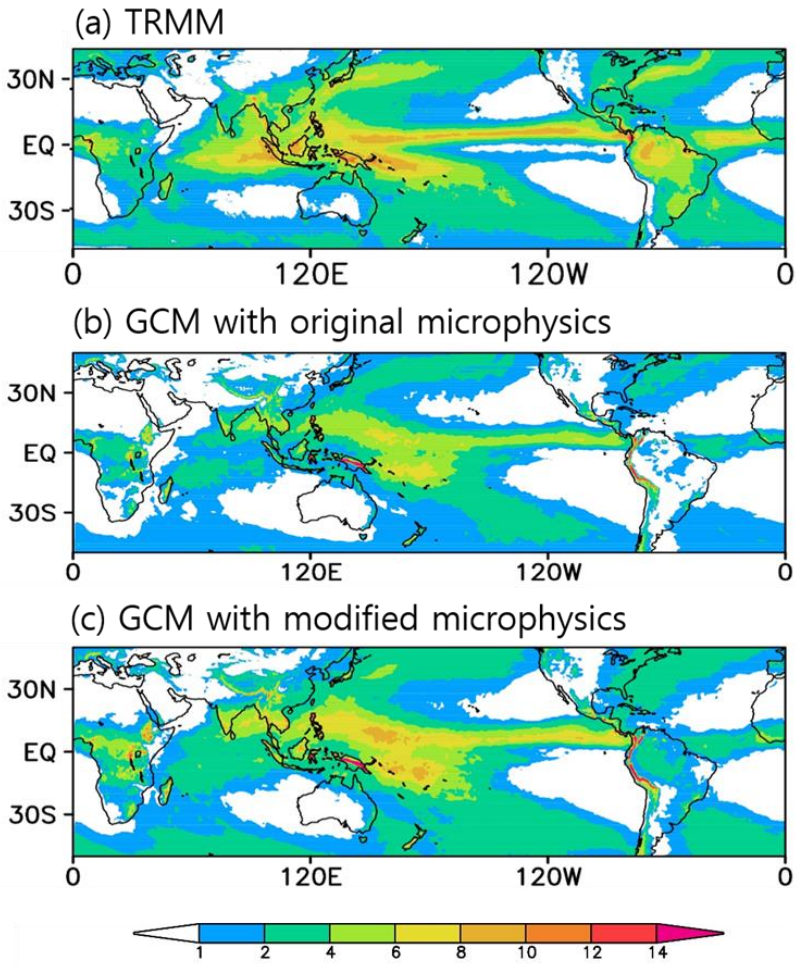

Figure 4.2. Spatial distributions of annual-mean precipitation (mm day^{-1}) for (a) TRMM observation, (b) GCM with original microphysics, and (c) GCM with modified microphysics (RH criteria 75% and terminal velocity 50%). Two-year simulations are used for the model case, and a ten-year mean of 2000-2009 is used for the TRMM. The TRMM data was interpolated to the model horizontal grid with 50 km resolution using an area-weighted method.

4.2 Additional vertical mixing to 50km GCM with comprehensive cloud microphysics

A 50km GCM with comprehensive cloud microphysics overestimated the low-level moisture. Figure 4.3 shows the vertical profiles of the bias of simulated annual mean cloud water content (cloud liquid water and cloud ice water) with respect to the CloudSat observations from Su et al. (2008). The cloud water content in the low-level is largely overestimated in the GCM with modified cloud microphysics (red line). It means that additional vertical mixing is required for the GCM with modified cloud microphysics. To improve the vertical mixing of GCM with modified cloud microphysics, a diffusion type non-precipitating shallow convection scheme based on Tiedtke (1989) is implemented. The GCM with modified cloud microphysics and shallow convection (blue line) shows an improvement in simulation of low-level cloud water content.

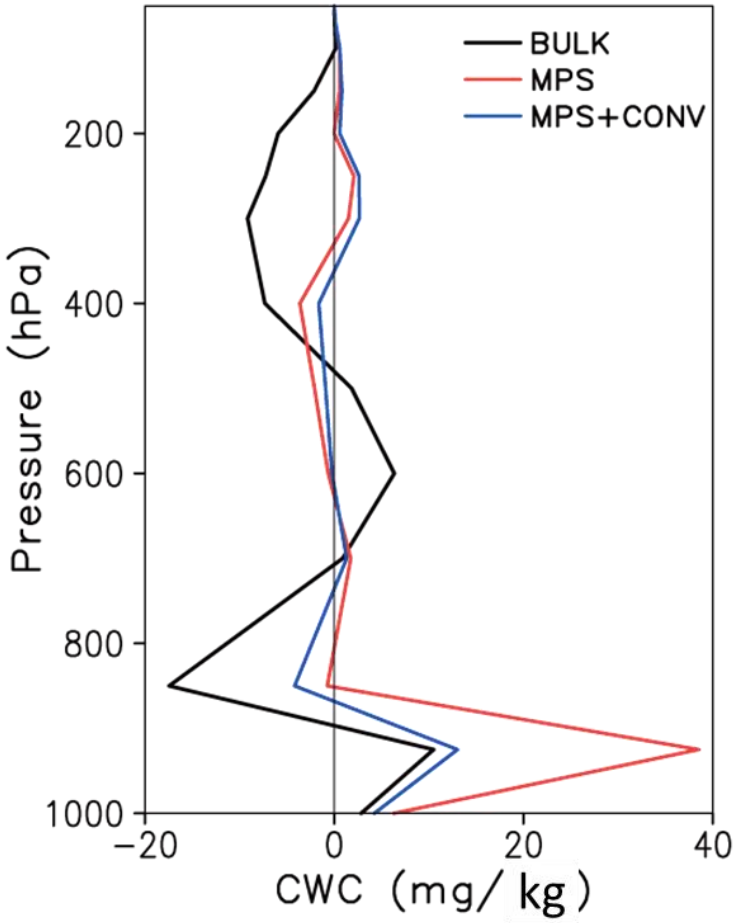

Figure 4.3. Vertical profiles of the bias of simulated annual-mean cloud water content (CWC; cloud liquid water + cloud ice water) with respect to the observation obtained from Su et al. (2008). The black, red and blue lines, respectively, are for the GCM with Bulk scheme, the GCM with modified microphysics, and the GCM with modified microphysics and a shallow convection. The CWC value is the horizontal average over the tropics between 30°S and 30°N.

4.3 Simulation results

1) Mean precipitation

To examine the basic property of the developed model, the mean precipitation is diagnosed. Figure 4.4 shows the spatial distribution of annual mean precipitation for the TRMM, GCM with modified cloud microphysics (RH criteria 75% and terminal velocity 50%), and GCM with modified cloud microphysics and shallow convection. The GCM with modified cloud microphysics and shallow convection shows improvements in simulation of precipitation over the Western Pacific, SPCZ, and ITCZ. But, the simulation of precipitation over the Indian Ocean is still remained in a problem.

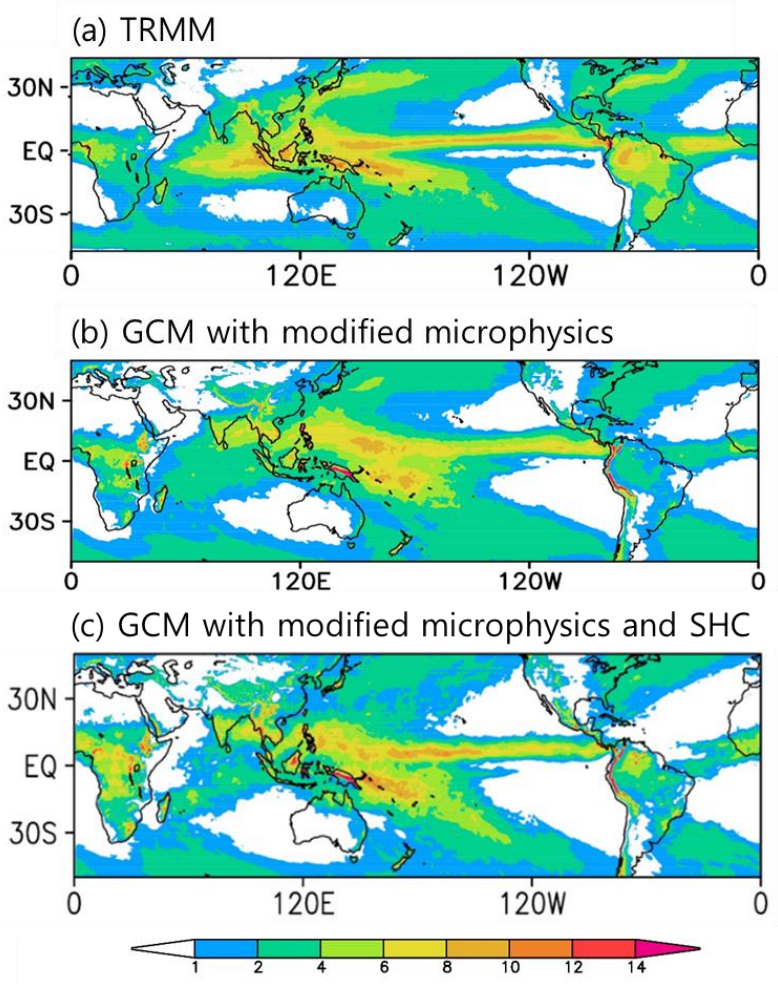

Figure 4.4. Spatial distributions of annual-mean precipitation (mm day^{-1}) for (a) TRMM observation, (b) GCM with modified microphysics (RH criteria 75% and terminal velocity 50%), and (c) GCM with modified microphysics and shallow convection. Two-year simulations are used for the model case, and a ten-year mean of 2000-2009 is used for the TRMM. The TRMM data was interpolated to the model horizontal grid with 50 km resolution using an area-weighted method.

The simulation of mean precipitation as a function of precipitation intensity is important because the weak and heavy precipitation is related to drought and flood which is the high impact weather on humans. In conventional GCMs, however, the weak precipitation was overestimated and the strong precipitation was underestimated compared to observations. Figure 4.5 shows the spatial distribution of light precipitation (<10mm day^{-1}), heavy precipitation (>60mm day^{-1}), and total precipitation for the TRMM, the GCM with bulk convection scheme, and the GCM with modified microphysics and shallow convection. The GCM with bulk convection scheme shows the overestimated light precipitation and the underestimated heavy precipitation compared to the TRMM. It is a common problem in the conventional parameterized GCMs (Dai 2006, Sun et al. 2006). The GCM with modified microphysics and shallow convection shows improvements in simulation of light precipitation and heavy precipitation. It indicates that cloud microphysics is required to simulate the light and heavy precipitation realistically.

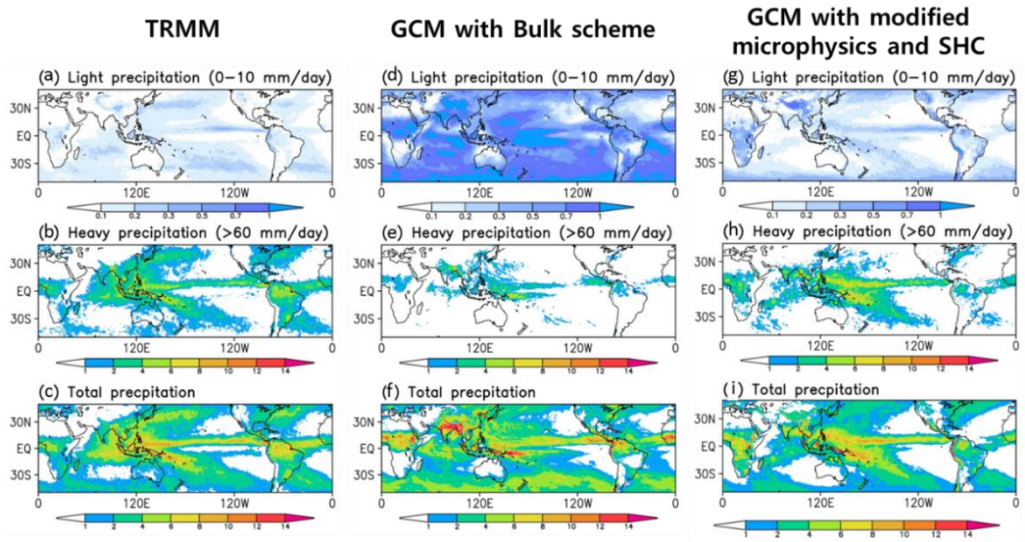

Figure 4.5. Spatial distribution of light precipitation (<10 mm day^{-1}, upper panel), heavy precipitation (>60 mm day^{-1}, middle panel), and total precipitation (lower panel) for the TRMM (a-c), the GCM with the bulk scheme (d-f), and the GCM with modified microphysics and shallow convection (g-i). Three-hourly precipitation data are used for classifying the light and heavy precipitation.

2) Precipitation frequency as a function of precipitation intensity

The precipitation frequency for the weak and heavy precipitation is examined more specifically. Figure 4.6 shows the frequency distribution of three-hourly mean precipitation over the Tropics (0°E-360°E, 30°S-30°N) as a function of precipitation intensity from the TRMM (black line), the GCM with modified cloud microphysics (purple line), the GCM with modified cloud microphysics and shallow convection (red line), and the GCM with bulk scheme (blue line). The GCM with bulk scheme shows the overestimated light precipitation and the underestimated heavy precipitation. The GCM with modified cloud microphysics and shallow convection shows the improvement in simulation of all precipitation frequencies, especially in simulation of heavy precipitation frequencies. The graupel/hail process of CRM cloud microphysics mainly influences the heavy precipitation simulation to improve (Kang et al. 2015).

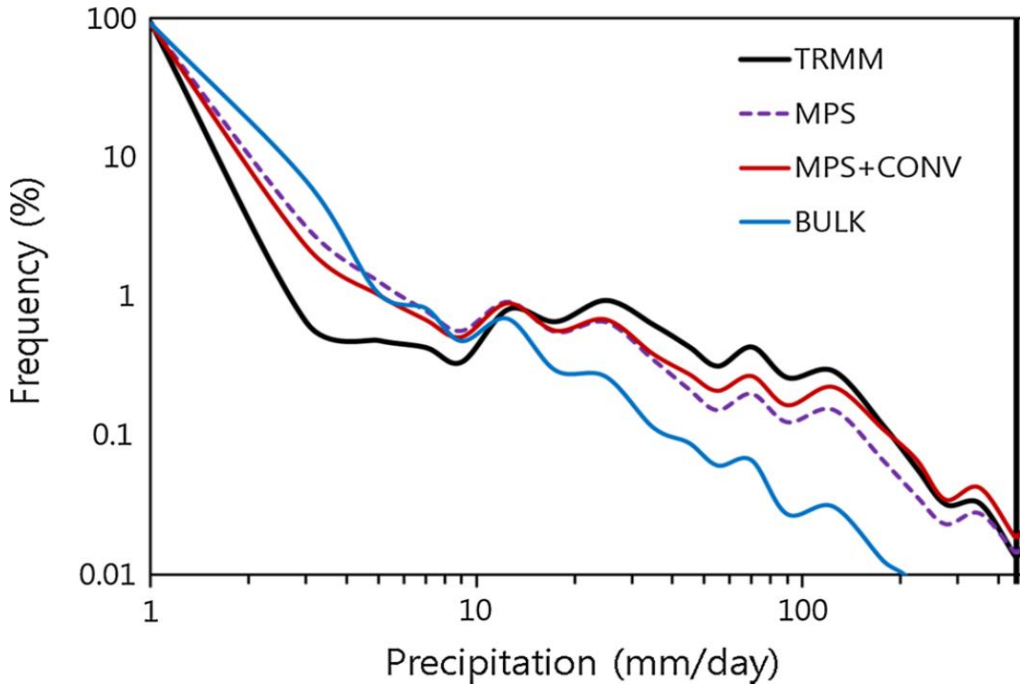

Figure 4.6. Frequency distribution of three-hourly precipitation over the Tropics (0°E-360°E, 30°S-30°N) as a function of precipitation intensity from the TRMM (black solid line), the GCM with modified microphysics (purple dashed line), the GCM with modified microphysics and shallow convective scheme (red solid line), and the GCM with the bulk scheme (blue solid line). The bin size is 1 mm day^{-1} for 0–60 mm day^{-1} of precipitation and increases gradually to 20 mm day^{-1} at 200 mm day^{-1}. Note the logarithmic scale.

3) MJO simulation

The Madden-Julian Oscillation (MJO) is dominant variability in the tropics with intraseasonal time scale. The MJO interacts with a wide range of tropical weather and climate phenomena. However, many conventional GCMs exhibit shortcomings to simulate the MJO. Figure 4.7 shows the longitude-time diagrams of daily mean precipitation averaged over 10°S-10°N for the TRMM, GCM with bulk scheme (PC-GCM; Parameterized Convection GCM), GCM with modified cloud microphysics (CM-GCM; Cloud Microphysics GCM), and GCM with modified cloud microphysics and shallow convection (MS-GCM; Cloud Microphysics and Shallow convection GCM). The GCM with bulk scheme shows weak eastward propagation and strong westward propagation. The GCM with modified cloud microphysics shows strong eastward propagation, but weak organization of precipitation. The GCM with modified cloud microphysics and shallow convection relatively well simulates the eastward propagation and organization of precipitation compared to the TRMM. It indicates that additional vertical mixing is required for organization of convection.

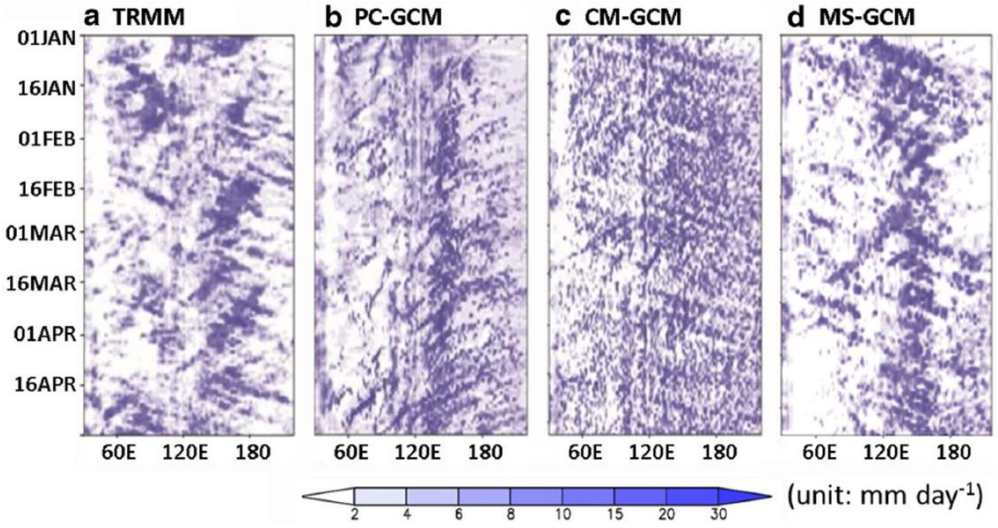

Figure 4.7. Longitude-time diagram of the daily mean precipitation averaged over 10°S–10°N from (a) TRMM, (b) GCM with parameterized convection, (c) GCM with modified cloud microphysics, and (d) GCM with modified cloud microphysics and shallow convection.

To examine the MJO simulation more specifically, the wavenumber-frequency power spectra of 10°S~10°N averaged 850hPa zonal wind is diagnosed (Fig 4.8). Five-year boreal winter (NOV-APR) is used for the model, and a ten-year boreal winter (NOV-APR) is used for the TRMM. In observation, the spectral power is concentrated in the MJO band (wavenumber 1-3 and period 30-90days). PC-GCM and CM-GCM poorly simulate spectral power in the MJO band, but MS-GCM simulates spectral power similar to observation. However, the wavenumber-frequency power spectra of 10°S~10°N averaged precipitation was still remained to improve more.

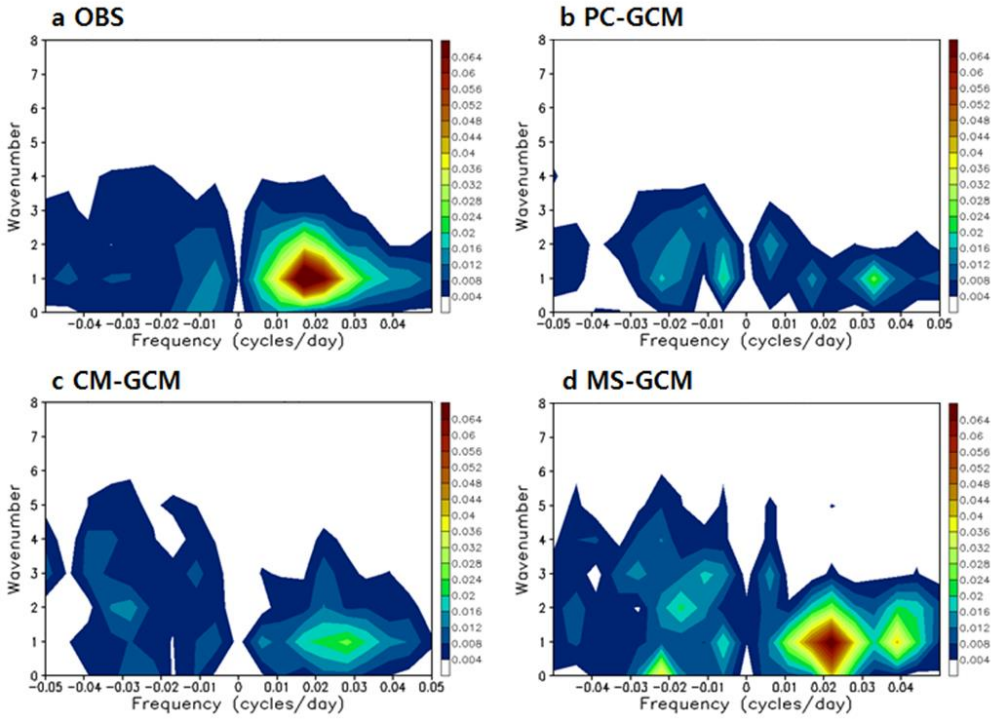

Figure 4.8. Wavenumber-frequency power spectra of 10°S~10°N averaged 850hPa zonal wind from (a) NCEP, (b) GCM with parameterized convection, (c) GCM with modified cloud microphysics, and (d) GCM with modified cloud microphysics and shallow convection. Five-year boreal winter (NOV-APR) is used for the model, and a ten-year boreal winter (NOV-APR) is used for the TRMM.

The MJO simulation is closely related to the moisture simulation. Therefore, the vertical profile of moisture is diagnosed. Figure 4.9 shows the vertical profiles of 30- to 90-day filtered specific humidity composite when the area average of 30- to 90-day filtered precipitation over the Indian Ocean (60°E–90°E, 10°S–10°N) is positive and larger than one standard deviation from observations (gray), GCM with parameterized convection (black), GCM with modified cloud microphysics (red), and GCM with modified cloud microphysics and shallow convection (blue). In observations, the positive anomaly appeared for the whole troposphere when 30- to 90-day filtered precipitation is activated. PC-GCM and CM-GCM poorly simulate this feature, but MS-GCM simulates it reasonable well. Added shallow convection improves the simulation of moisture profile varied with MJO time scale. It indicates that the shallow convection improves the coupling between convection and environmental moisture, which is important process to simulate the realistic MJO (Kim et al. 2014).

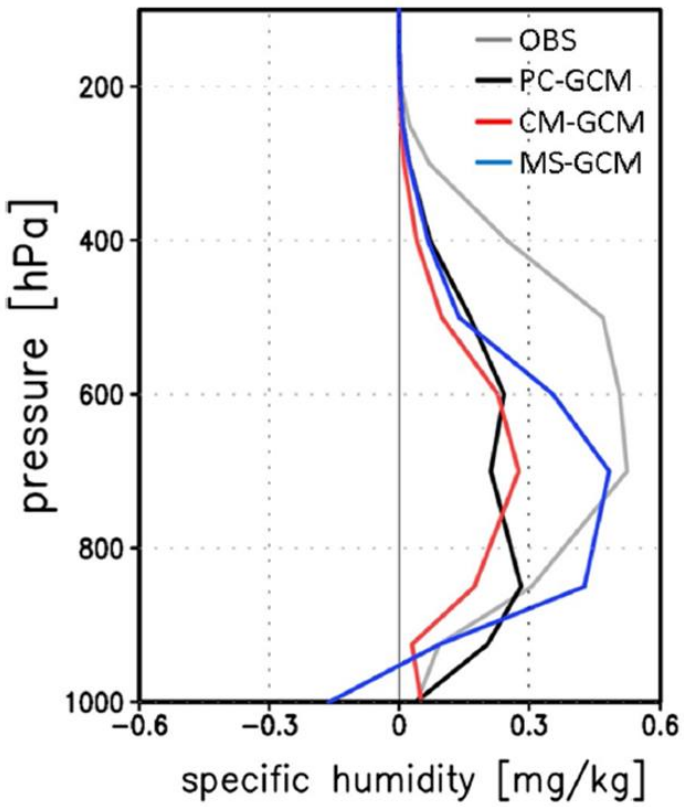

Figure 4.9. Vertical profile of 30- to 90-day filtered specific humidity composite when the area average of 30- to 90-day filtered precipitation over the Indian Ocean (60°E–90°E, 10°S–10°N) is positive and larger than one standard deviation from observations (gray), GCM with parameterized convection (black), GCM with modified cloud microphysics (red), and GCM with modified cloud microphysics and shallow convection (blue).

To examine the moisture simulation related to MJO simulation more specifically, the moisture spatial pattern is diagnosed. Figure 4.10 shows the Composite maps of 30- to 90-day filtered specific humidity averaged over the lower level (850–700 hPa) when the area average of 30- to 90-day filtered precipitation over the Indian Ocean (60°E–90°E, 10°S–10°N) is positive and larger than one standard deviation. In observations, the positive anomaly appeared over the Indian Ocean and the Western Pacific when 30- to 90-day filtered precipitation is activated on the Indian Ocean. The positive anomaly on the Western Pacific is important to the MJO eastward propagation from the Indian Ocean to the Western Pacific. PC-GCM and CM-GCM poorly simulate the positive anomaly over the Indian Ocean and the Western Pacific, but MS-GCM simulates this feature reasonably well.

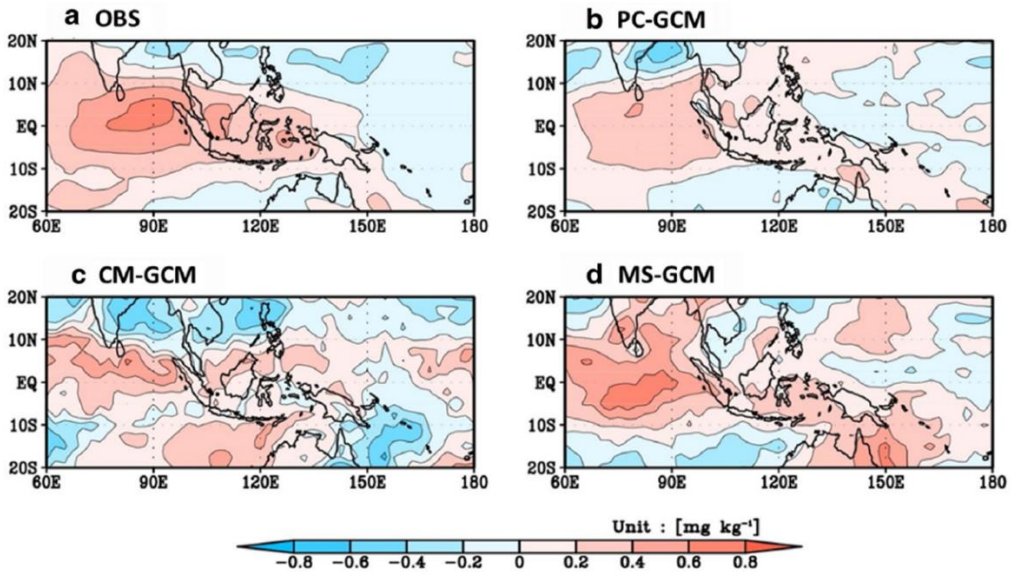

Figure 4.10. Composite map of 30- to 90-day filtered specific humidity averaged over the lower level (850–700 hPa) when the area average of 30- to 90-day filtered precipitation over the Indian Ocean (60°E–90°E, 10°S–10°N) is positive and larger than one standard deviation from (a) observations, (b) GCM with parameterized convection, (c) GCM with modified cloud microphysics, and (d) GCM with modified cloud microphysics and shallow convection.

5 Improvement of vertical mixing appropriated to 50km GCM with cloud microphysics

The conventional general circulation models (GCMs) have two processes to produce total precipitation. One is the resolved grid-scale cloud scheme (or large-scale condensation scheme) and another is the unresolved sub-grid scale convection scheme. The main role of convection scheme is parameterization of unresolved sub-grid scale vertical transport, accompanying the convective condensation and precipitation process. Since 1960s, many convection schemes were developed based on several different concepts, such as the moist-convective adjustment (Manabe et al. 1965), the moisture convergence (Kuo 1974), and the cumulus mass flux (Arakawa and Schubert 1974). More detail review for different types of convection scheme is described in Arakawa (2004). The convection schemes based on the cumulus mass flux have been developed by many modeling groups (Arakawa and Schubert 1974, Tiedtke 1989, Gregory and Rowntree 1990, Moorthi and Suarez 1992, Zhang and McFarlane 1995, Pan and Randall 1998, Chikira and Sugiyama 2010, Kim and Kang 2012). This

paper focused on cumulus mass flux type convection scheme, the simplified Arakawa-Schubert cumulus convection scheme based on Relaxed Arakawa-Schubert scheme (Moorthi and Suarez 1992).

Recently, the horizontal resolution of GCMs have been increasing as the development of computing power. Therefore, the GCMs have capability to simulate more resolved grid-scale vertical transport. As the horizontal resolution of GCMs becomes higher than order of 10km, convections can be partly resolved by grid-scale vertical transport. The order of 10km GCMs is faced the problem of how represent the convection in GCMs, which is so called "Grey Zone" problem. More details for this issue are in "The Grey Zone Project" webpage (http://projects.knmi.nl/greyzone). To overcome this problem, Arakawa and Wu (2013) presented a scale-adaptive deep convection scheme which is formulated to reduce the sub-grid scale vertical transport as the horizontal resolution increases. They controlled the cumulus base mass flux using the convective cloud fraction (σ). For this method, the parameterization of convective cloud fraction (σ) is required. But, additional parameterization of convective cloud fraction (σ) is possible to increase uncertainty in convection scheme. Kwon and Hong (2016) showed that the scale-adaptive deep

convection scheme by controlling the cloud base mass flux, convective inhibition, and convective detrainment as a function of convective cloud fraction (σ) simulates well a heavy rainfall case over Korea in WRF model simulation. The parameterization of convective cloud fraction (σ) in Kwon and Hong (2016) was somewhat different from that of Arakawa and Wu (2013).

However, the necessity of formulating the scale-adaptive convection is still debatable. Zhang et al. (2015) insisted that reducing the sub-grid scale vertical transport as the horizontal resolution increases is already implicitly parameterized in deep convection scheme. After that, Arakawa and Wu (2015) insisted that the parameterization of the convective cloud fraction (σ) to make the scale-adaptive deep convection scheme is necessary although it is implicitly parameterized. For understanding the necessity of the scale-adaptive convection more practically, it is required to examine the inherent change of the sub-grid scale vertical transport by deep convection scheme as the horizontal resolution increases.

There are three objectives in this study. 1) Examining the inherent change of the unresolved sub-grid scale vertical transport as the horizontal resolution increases using GCMs with different horizontal resolution simulations. 2)

Finding the appropriate decrease ratio of the unresolved sub-grid scale vertical transport as the horizontal resolution increases using 3-D CRM simulations. 3) Application of the appropriate decrease ratio of the unresolved sub-grid scale vertical transport obtained from CRM simulation to the GCMs.

5.1 Conventional GCM simulations with different horizontal resolutions

The GCMs with different horizontal resolutions (280km, 100km, 50km) and same parameterization are simulated to examine inherent changes of the GCM as the horizontal resolution increases. The model time steps for different horizontal resolution simulations are used same value of 1800 second because the model time step can induce the inherent changes in GCMs. We designed the experiments to examine only the influence of horizontal resolution change.

The spatial patterns of precipitation mean states from GCMs with different horizontal resolutions are similar, but the intensities of precipitation mean states are somewhat increased as the horizontal resolution increases in the SPCZ and ITCZ regions (Fig. 5.1).

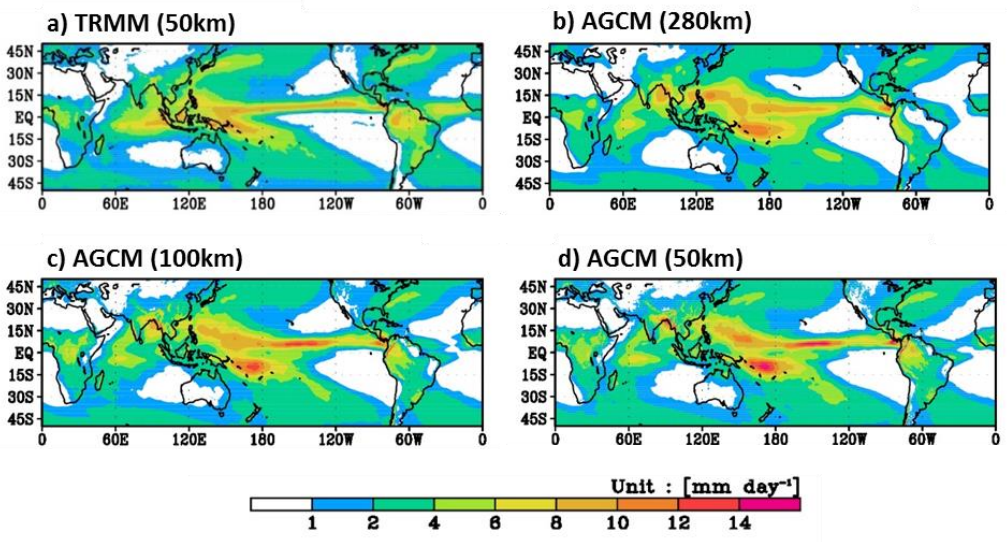

Figure 5.1. Precipitation mean state for a) TRMM, b) AGCM with 280km resolution, c) AGCM with 100km resolution, and d) AGCM with 50km resolution. Δt of all simulations are same with 30 minutes. 10 years data used for the TRMM and 5 years data used for the AGCM. TRMM was interpolated to 50km resolution.

The ratio of convective precipitation generated by deep convection scheme to total precipitation is somewhat increased as the horizontal resolution increases in the Tropics (Fig. 5.2). This result implies that the increased total precipitation in SPCZ region as the horizontal resolution increased is due to the increased convective precipitation generated by convection scheme.

The convective precipitation generated by convection scheme is proportional to intensity of cumulus mass flux. Figure 5.3 shows the vertical profiles of omega and cumulus mass flux composite for the GCM with 280km, 100km, and 50km resolutions. Composite is conducted over the Tropics (0E-360E, 30S-30N) using the grids that precipitation and upward vertical motion occur (prcp>0 and omega<0). As the horizontal resolution increases, both of the omega and cumulus mass flux increase. It indicates that the parameterized sub-grid scale vertical transport should be decreased according to appropriate rate.

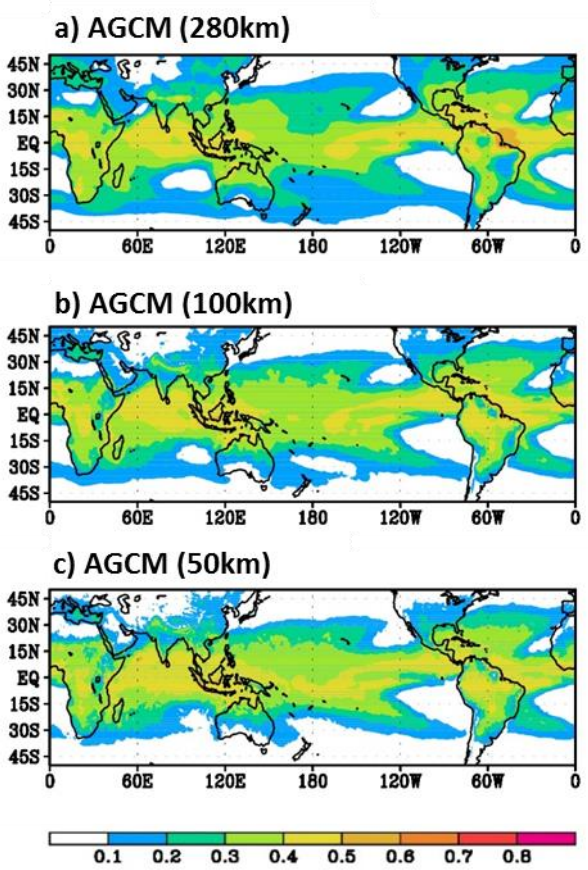

Figure 5.2. Ratio of convective precipitation generated by deep convection scheme to total precipitation for a) AGCM with 280km resolution, b) AGCM with 100km resolution, and c) AGCM with 50km resolution. 5 years data used for the AGCM.

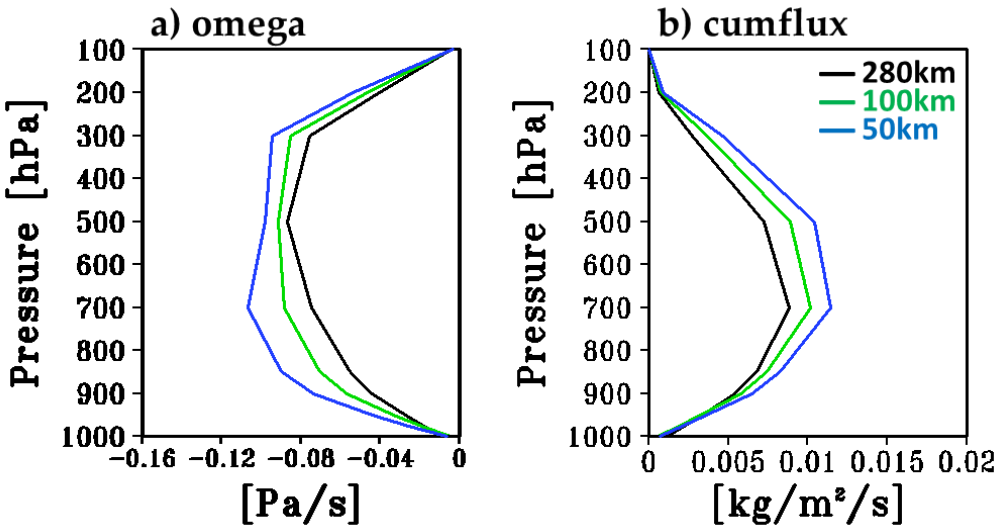

Figure 5.3. Vertical profiles of a) omega and b) cumulus mass flux composite for AGCM with 280km (black curve), 100km (green curve), and 50km(blue curve) resolutions. Composite is conducted over the Tropics (0E-360E, 30S-30N) using the grids that precipitation and upward vertical motion occur (prcp>0 and omega<0).

5.2 3-dimensional CRM simulations

The 3-dimensional CRMs with 1km horizontal resolution are simulated to examine the appropriate decrease ratio of sub-grid scale vertical transport as the horizontal resolution increases. The CRM is designed for the radiative-convective equilibrium (RCE) experiment which is a kind of idealized experiment using prescribed SST and radiative cooling. The RCE experiments have used for idealization of the mean tropical climate, especially in the mean feature of tropical convections (Held et al. 1993, Tao et al. 1999, Bretherton et al. 2005, Muller and Held 2012, Khairoutdinov and Emanuel 2013). In this study, we used the prescribed SST with 302K and the radiative cooling with -1.5K/day. These prescribed SST and radiative cooling are favorable condition for successive construction of convection.

The moist static energy (h) tendency equation is useful for examination of simulated vertical transport because the moist static energy (h) is conserved physical quantity for condensation and height change.

$$\frac{\partial h}{\partial t} = -\mathrm{u}\frac{\partial \mathrm{h}}{\partial \mathrm{x}} - \mathrm{v}\frac{\partial \mathrm{h}}{\partial \mathrm{y}} - \mathrm{w}\frac{\partial \mathrm{h}}{\partial \mathrm{z}} + \mathrm{R}$$

Where $h = \mathrm{CpT} + \mathrm{gz} + \mathrm{Lq}$ is moist static energy. u, v, w are zonal wind, meridional wind, vertical wind, respectively. R is radiative forcing.

After Reynolds Averaging, the moist static energy (h) tendency equation becomes below.

$$\frac{\partial \bar{h}}{\partial t} = -\bar{u}\frac{\partial \bar{h}}{\partial \mathrm{x}} - \bar{v}\frac{\partial \bar{h}}{\partial \mathrm{y}} - \bar{w}\frac{\partial \bar{h}}{\partial \mathrm{z}} - \frac{\partial\left(\overline{w'h'}\right)}{\partial \mathrm{z}} + \bar{R}$$

Here, overbar and prime indicate the grid mean and the anomaly removed grid mean, respectively. For the sub-grid vertical mixing, the anomaly $\left(\overline{\mathrm{w}'\frac{\partial \mathrm{h}'}{\partial \mathrm{z}}}\right)$ mixing term instead of anomaly flux $\frac{\partial\left(\overline{\mathrm{w}'\mathrm{h}'}\right)}{\partial \mathrm{z}}$ mixing is considered because the incompressible assumption, the anomaly $\left(\overline{\mathrm{w}'\frac{\partial \mathrm{h}'}{\partial \mathrm{z}}}\right)$ form can transform to the anomaly flux $\frac{\partial\left(\overline{\mathrm{w}'\mathrm{h}'}\right)}{\partial \mathrm{z}}$ form in which assumption, is not used in CRM. Therefore, the budget of $\overline{w\frac{\partial \mathrm{h}}{\partial \mathrm{z}}} = \bar{w}\frac{\partial \bar{h}}{\partial \mathrm{z}} + \frac{\partial\left(\overline{w'h'}\right)}{\partial \mathrm{z}}$ is not conserved, while $\overline{w\frac{\partial \mathrm{h}}{\partial \mathrm{z}}} = \bar{w}\frac{\partial \bar{h}}{\partial \mathrm{z}} + \overline{w'\frac{\partial h'}{\partial \mathrm{z}}}$ is conserved in analysis results.

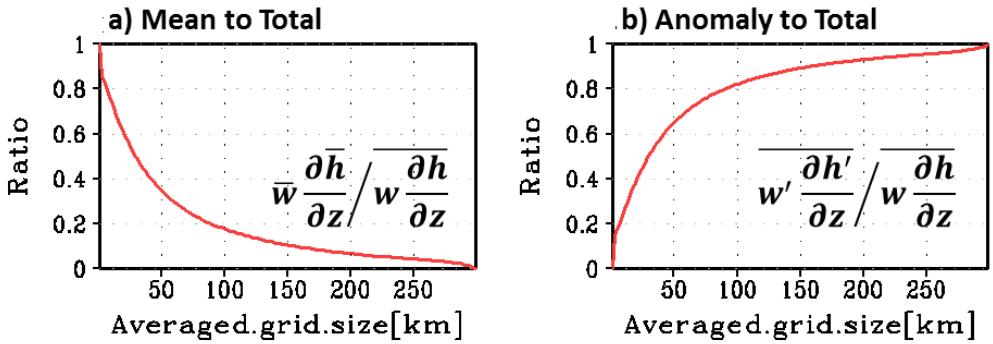

Figure 5.4. Resolution dependency of 850hPa moist static energy vertical mixing ratio based on averaged gird size for a) ratio of mean vertical mixing to total mixing b) ratio of anomaly vertical mixing to total mixing. The area averaged is conducted over the only updraft domains ($\overline{w} > 0$ and $\frac{\partial \overline{h}}{\partial z} < 0$) .

Figure 5.4. shows the ratio of area averaged vertical mixing of moist static energy (h) at 850hPa level for the mean ($\overline{w}\frac{\partial \overline{h}}{\partial z}$) to the total ($\overline{w\frac{\partial h}{\partial z}}$) and the anomaly ($\overline{w'\frac{\partial h'}{\partial z}}$) to the total ($\overline{w\frac{\partial h}{\partial z}}$) as a function of averaged grid size. The area averaged is conducted over the only updraft domains ($\overline{w} > 0$ and $\frac{\partial \overline{h}}{\partial z} < 0$). The ratio of the mean ($\overline{w}\frac{\partial \overline{h}}{\partial z}$) mixing decreases as the averaged grid size becomes larger, and the ratio of the anomaly ($\overline{w'\frac{\partial h'}{\partial z}}$) mixing increases as the averaged grid size becomes larger, indicating the role of anomaly ($\overline{w'\frac{\partial h'}{\partial z}}$) mixing is small in high resolution and large in low resolution. It indicates that the conventional deep convection scheme should reduce their role as the model resolution becomes higher.

5.3 Conventional GCM with scale-adaptive deep convection scheme

The cumulus base mass flux is a key factor to control the intensity of the convection because the convective structure is constructed based on the cumulus mass flux normalized by the cumulus base mass flux. Therefore, the cumulus base mass flux is considered as the closure in convection scheme (Arakawa and Schubert 1974) and is used as a control factor to develop the scale-adaptive convection scheme (Arakawa and Wu 2013, Kwon and Hong 2016). This study also used the cumulus base mass flux as a control factor to decrease the ratio of sub-grid scale vertical transport appropriated to the ratio obtained from the CRM simulation. Figure 5 shows ratio of domain averaged (0°E-360°E, 30°S-30°N) sub-grid scale vertical transport to total vertical transport for moist static energy at 850hPa level. The reason for using 850hPa level is that the 850hPa level is the bass level of the convection usually. Only updraft domains ($\overline{\omega} < 0$ and $\frac{\partial \overline{h}}{\partial p} > 0$) are used for calculation in GCMs. The ratio for GCM is normalized by 280km simulation result. To obtain the sub-

grid scale vertical mixing for moist static energy in GCMs, the tendencies of temperature and specific humidity obtained from deep convection, shallow convection, and PBL scheme are used.

$$\frac{\partial\left(\overline{\omega'\mathrm{T}'}\right)}{\partial \mathrm{p}} \approx \left(\frac{\partial \mathrm{T}}{\partial \mathrm{t}}\right)_{\mathrm{DC,SC,PBL}}$$

$$\frac{\partial\left(\overline{\omega'\mathrm{q}'}\right)}{\partial \mathrm{p}} \approx \left(\frac{\partial \mathrm{q}}{\partial \mathrm{t}}\right)_{\mathrm{DC,SC,PBL}}$$

$$\frac{\partial\overline{\omega'(\mathrm{CP}\cdot \mathrm{T}' + \mathrm{L}\cdot \mathrm{q}' + \mathrm{g}\cdot z')}}{\partial \mathrm{p}} \approx \mathrm{CP}\left(\frac{\partial \mathrm{T}}{\partial \mathrm{t}}\right)_{\mathrm{DC,SC,PBL}} + \mathrm{L}\left(\frac{\partial \mathrm{q}}{\partial \mathrm{t}}\right)_{\mathrm{DC,SC,PBL}}$$

$$= \left(\frac{\partial\overline{\omega'\mathrm{h}'}}{\partial \mathrm{p}}\right)_{\mathrm{DC,SC,PBL}}$$

Here, T, q, and ω indicate the temperature, specific humidity, and pressure vertical velocity, respectively. CP and L indicate the specific heat of dry air at constant pressure (1004J/K/kg) and the latent heat of condensation (2.5×10^6J/kg), respectively. DC, SC, and PBL indicate the deep convection, shallow convection, and planetary boundary layer, respectively. Overbar and prime indicate the grid mean and the anomaly removed grid mean. The $\frac{\partial\overline{\omega' z'}}{\partial \mathrm{p}}$ term is zero in hydrostatic GCM.

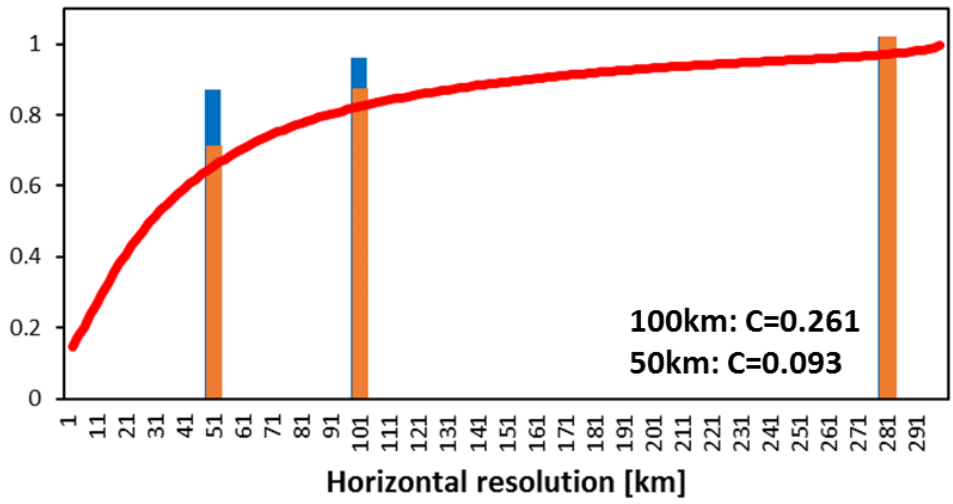

Figure 5.5. Ratio of domain averaged (0E-360E, 30S-30N) sub-grid scale vertical mixing to total vertical mixing for moist static energy at 850hPa level. Blue bars indicate original simulation, and orange bars indicate scale-adaptive simulation using cumulus base mass flux control. Red curves indicate the ratio of sub-grid scale vertical mixing to total vertical mixing for moist static energy obtained from 3d-CRM simulation. Only updraft domains ($\bar{\omega} < 0$ and $\frac{\partial \bar{h}}{\partial p} > 0$) are used for calculation in GCMs. The ratio for GCM is normalized by 280km simulation result.

In figure 5.5, original GCM simulations (blue bars) show little decrease of the ratio as the horizontal resolution increases, but it is not appropriated to the ratio obtained from the CRM simulation (red curve). To reduce the parameterized sub-grid scale vertical mixing in GCM, the cumulus base mass flux is used for a control parameter. It is a similar framework with other scale-adaptive convection studies (Arakawa and Wu 2013, Kwon and Hong 2016). But, they used the parameterized convective cumulus fraction (σ) and we used the sub-grid scale vertical mixing ratio to total ratio. In this study, the reduced factors of cloud base mass flux are 0.261 and 0.093 for the 100km and 50km simulations, respectively. These values are obtained from sensitivity tests. The GCM with cloud base mass flux modification simulations (orange bars) are fitted to the ratio of CRM simulation.

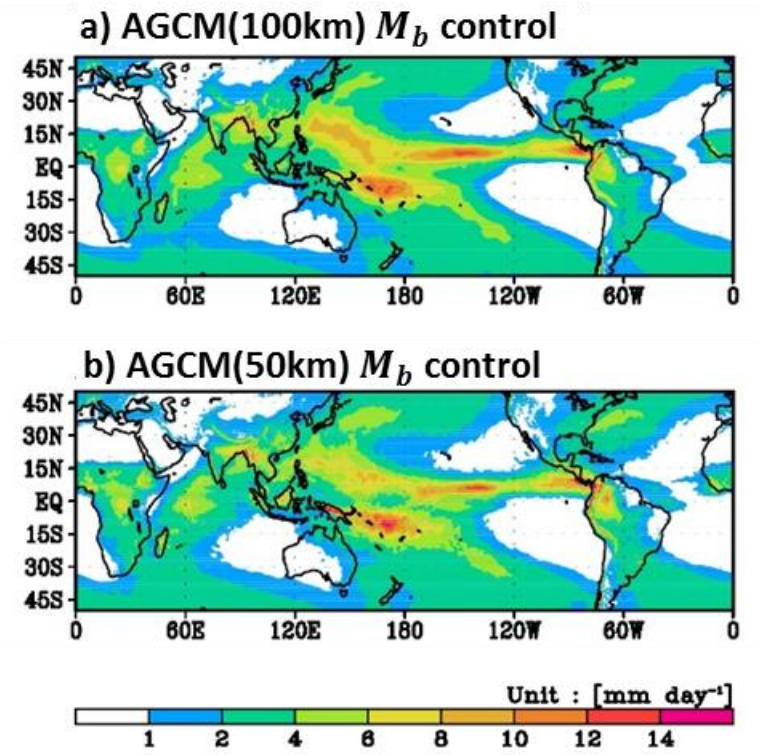

Figure 5.6. Precipitation mean state of AGCM simulation for a) 100km resolution and b) 50km resolution with cumulus base mass flux control.

To examine the basic property of the developed model, the mean precipitation is diagnosed. Figure 5.6 shows the spatial pattern of precipitation mean state from 100km AGCM and 50km AGCM simulation with scale-adaptive convection. The spatial patterns are similar to original simulation, but the intensity is somewhat decreased over the SPCZ and ITCZ regions. The ratio of convective precipitation generated by deep convection scheme to total precipitation is decreased globally in 100km AGCM and 50km AGCM simulation with scale-adaptive convection (Fig. 5.7). Although the precipitation mean state is not much changed, the convective precipitation generated by deep convection scheme is much changed.

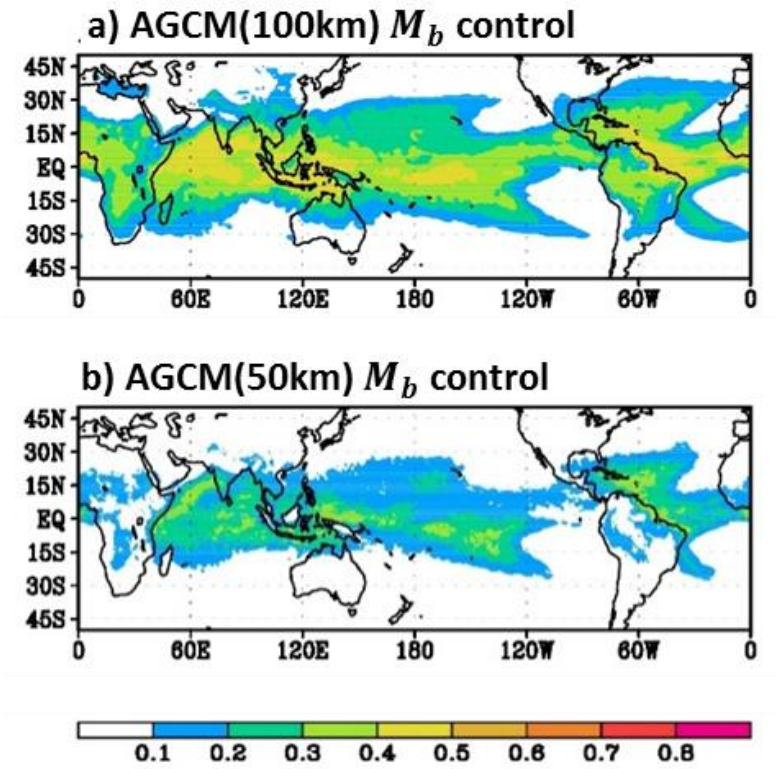

Figure 5.7. Ratio of convective precipitation generated by deep convection scheme to total precipitation from AGCM simulation for a) 100km resolution and b) 50km resolution with cumulus base mass flux control.

The resolved grid-scale precipitation is influenced by grid-scale vertical motion (omega) and the parameterized sub-grid scale precipitation is influenced by cumulus mass flux. Figure 5.8 shows the vertical profiles of omega and cumulus mass flux composite from AGCM with cumulus base mass flux control simulations for 100km, and 50km resolutions. Composite is conducted over the Tropics (0E-360E, 30S-30N) using the grids that precipitation and upward vertical motion occur (prcp>0 and omega<0). As the horizontal resolution increases, the omega increases and the cumulus mass flux decreases. It indicates that the convective precipitation is formulated by resolved grid-scale vertical transport and large-scale condensation to some extent, which is convection permitting models.

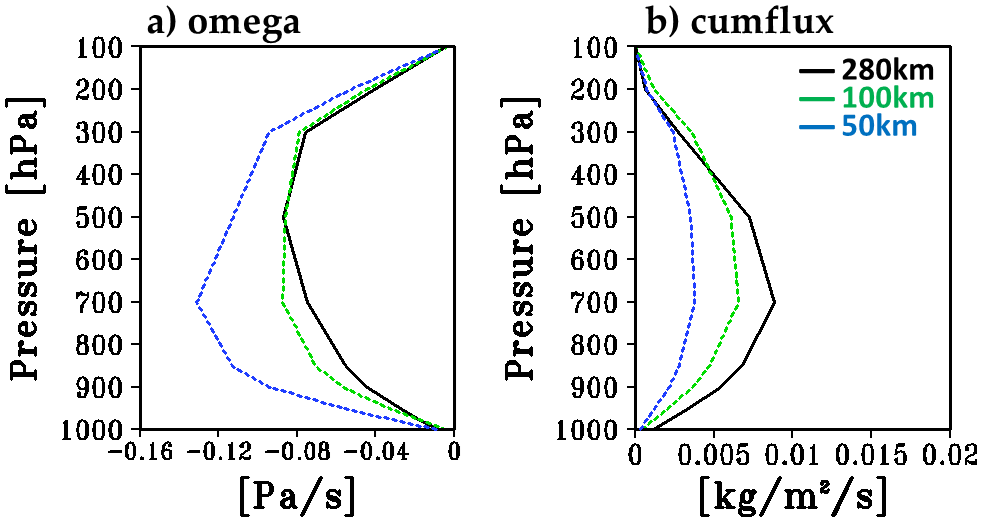

Figure 5.8. Vertical profiles of a) omega and b) cumulus mass flux composite from AGCM with cumulus base mass flux control simulations for 100km (green curve) and 50km(blue curve) resolutions, and AGCM with original parameterization for 280km (black curve) resolution. Composite is conducted over the Tropics (0E-360E, 30S-30N) using the grids that precipitation and upward vertical motion occur (prcp>0 and omega<0).

To examine the basic property of the developed model, the precipitation variability is diagnosed. Figure 5.9 shows the standard deviation of daily mean precipitation. Although the precipitation mean state is not much changed, the precipitation variance is increased in 100km AGCM and 50km AGCM simulation with scale-adaptive convection. Figure 5.10 shows that frequency distribution of 3-hourly mean precipitation based on precipitation strength. The original AGCMs tends to simulate strong precipitation less and weak precipitation more. But, the AGCMs with scale-adaptive convection simulate the strong precipitation and weak precipitation reasonably well compared to the original AGCMs. It is related to the strong variability of precipitation shown in Fig. 5.9.

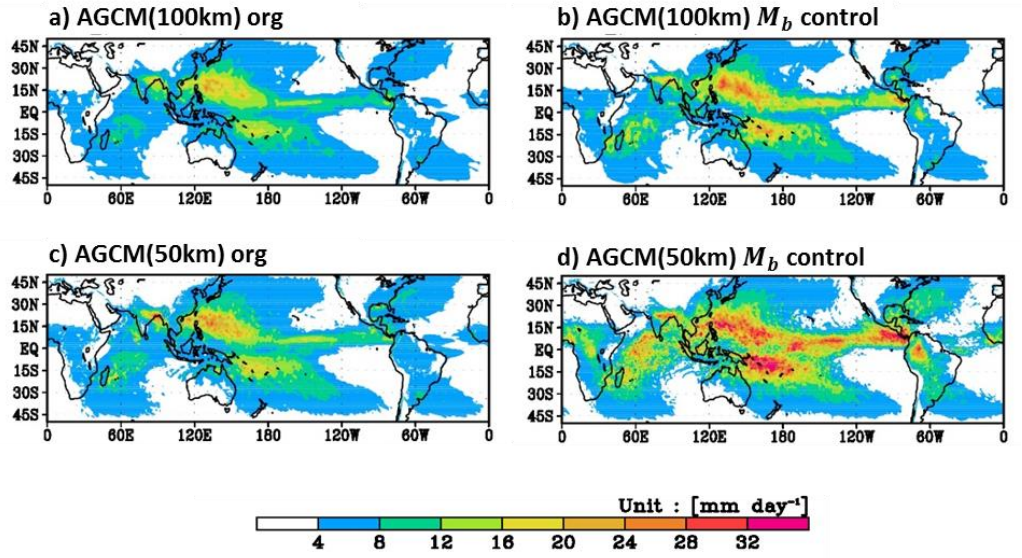

Figure 5.9. Standard deviation of daily mean precipitation for AGCM simulation with different resolutions (100km, 50km) from a),c) original simulation, b),d) scale-adaptive simulation using cumulus base mass flux control.

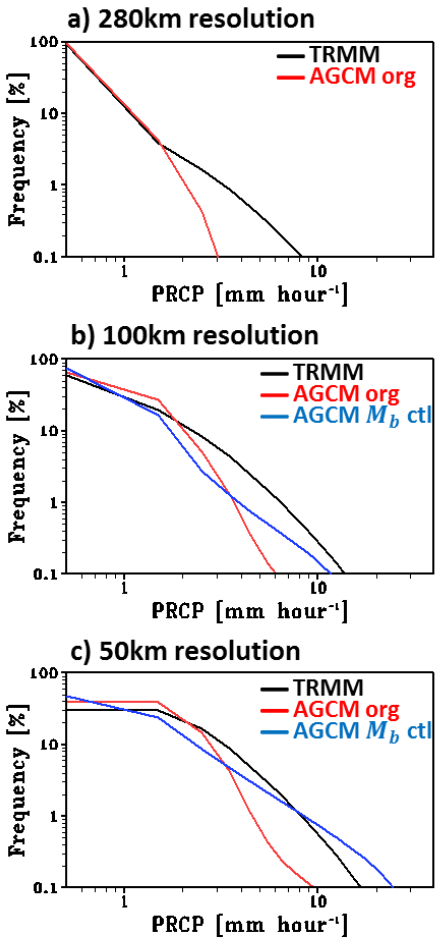

Figure 5.10. Frequency distribution of 3hourly mean precipitation based on precipitation strength from TRMM and AGCM simulation with scale-adaptive controls for a) 280km resolution, b) 100km resolution, and c) 50km resolution. Domain of 0°E-360°E and 30°S-30°N is used for calculation. TRMM data was interpolated to each target grid.

To examine the MJO simulation, the Lag-longitude diagram of 10S-10N averaged U850 over the Indian Ocean is used (Fig.5.11). In observation, eastward propagations are clearly appeared, whereas the eastward propagations in the original GCMs are poorly simulated. However, the 50km AGCM with cumulus base mass flux control simulates the eastward propagation reasonably well, but propagation speed is somewhat faster than that of observation.

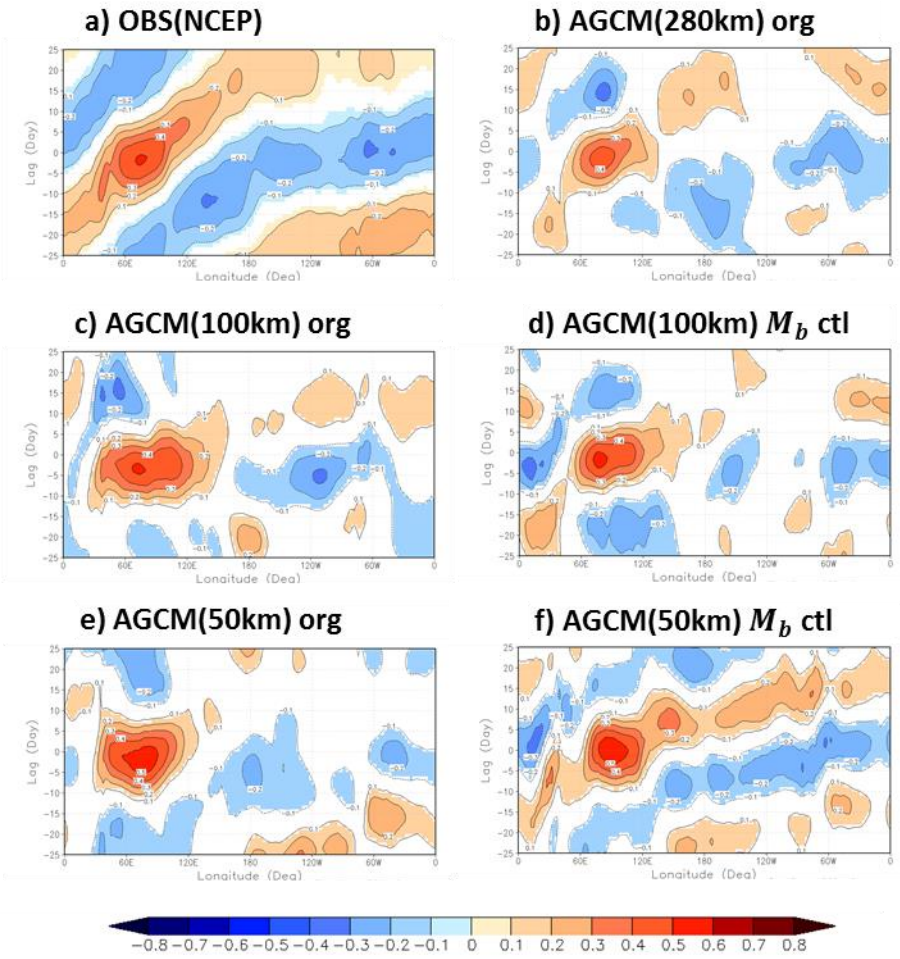

Figure 5.11. Lag-longitude diagram of 10S-10N averaged U850 over the Indian Ocean from a) NCEP, b),c),e) original AGCM simulation with 280km, 100km and 50km resolutions, d),f) scale-adaptive AGCM simulation with 100km and 50km resolutions using cumulus base mass flux control. Wavenumber-frequency power spectra was calculated for each year of boreal winter (NOV-APR) and then averaged over all years of data.

5.4 MP-GCM with scale-adaptive deep convective mixing

The Relaxed version of Arakawa-Shubert deep convection scheme (RAS scheme; Moorthi and Suarez 1992) is used to improve the vertical mixing appropriated to 50km GCM with cloud microphysics. In the RAS scheme, the closure is the cloud base mass flux. Therefore, we can control the strength of deep convection as the control the cloud base mass flux. Figure 5.12 shows that the spatial distributions of annual-mean precipitation for TRMM, MP-GCM with shallow convection, MP-GCM with shallow convection and deep convection, and MP-GCM with shallow and scale-adaptive deep convection. The MP-GCM with shallow convection and deep convection overestimates the precipitation strength on the north of equator Western Pacific compared to observation, whereas the MP-GCM with shallow and scale-adaptive deep convection overcomes this problem. But, the precipitation simulation on the Indian Ocean should be improved more.

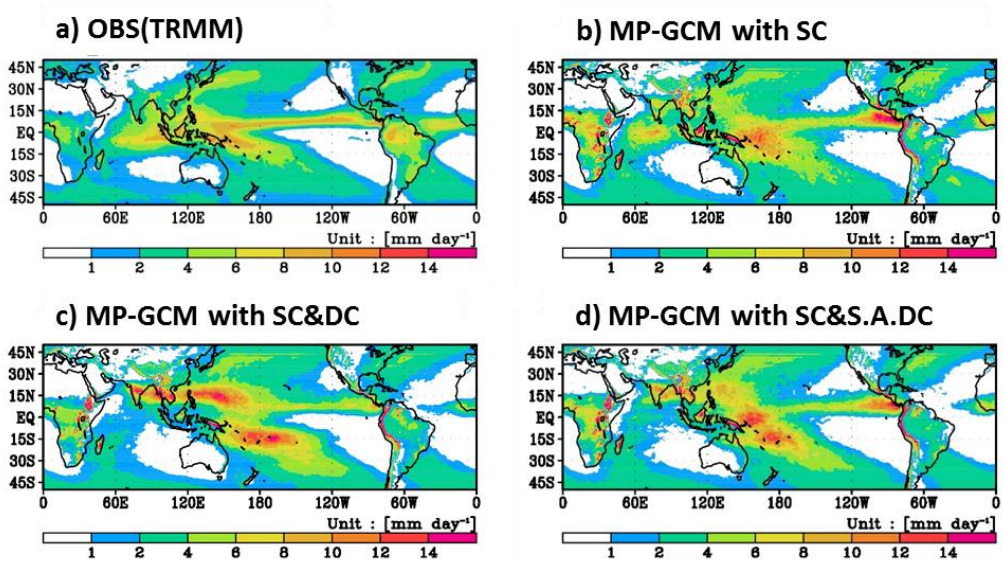

Figure 5.12. Spatial distributions of annual-mean precipitation for (a) TRMM, (b) MP-GCM with shallow convection, (c) MP-GCM with shallow convection and deep convection, and (d) MP-GCM with shallow and scale-adaptive deep convection. 5-year simulation are used for the model case, and a 10-year mean of 2000-2009 is used for the TRMM.

To examine the basic property of the developed model, the vertical profile of specific humidity is diagnosed. Figure 5.13 shows that the vertical profiles of specific humidity and specific humidity bias from the observation for MP-GCM with shallow convection (red), MP-GCM with shallow convection and deep convection (blue), and MP-GCM with shallow convection and scale-adaptive deep convection (green). The MP-GCM with shallow convection underestimates the specific humidity in middle troposphere, whereas the MP-GCM with shallow convection and deep convection is improved to simulate the specific humidity in middle troposphere. Although the MP-GCM with shallow convection and scale-adaptive deep convection reduced the strength of deep convection, the simulation of specific humidity in middle troposphere is improved compared to the MP-GCM with shallow convection.

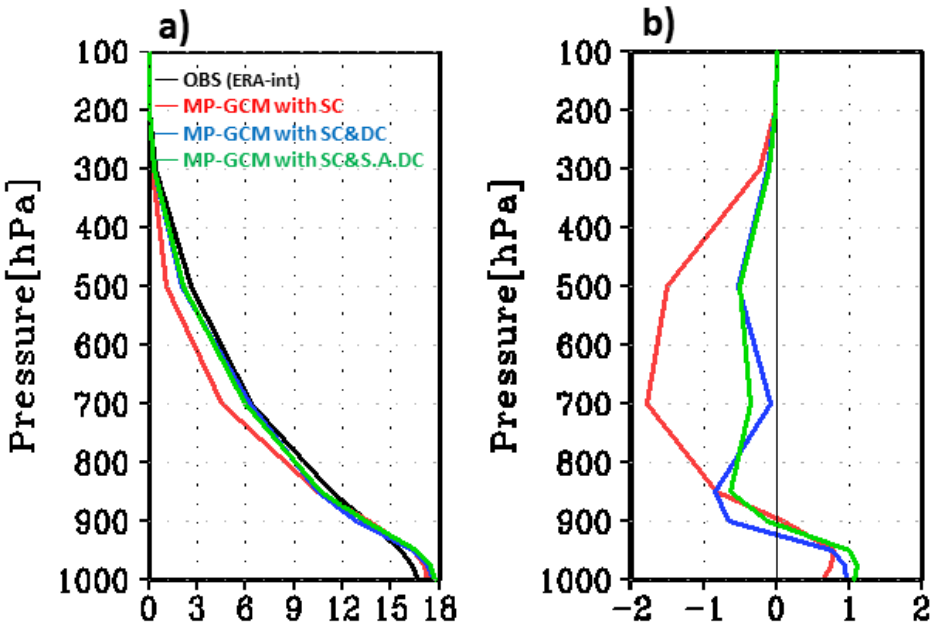

Figure 5.13. Vertical profiles of (a) specific humidity and (b) specific humidity bias from observation for MP-GCM with shallow convection (red), MP-GCM with shallow convection and deep convection (blue), and MP-GCM with shallow convection and scale-adaptive deep convection (green).

To examine the MJO simulation, the longitude-time diagram of precipitation is diagnosed. Figure 5.14 shows that the longitude-time diagram of the daily mean precipitation averaged over 10°S–10°N from the TRMM, MP-GCM with shallow convection, MP-GCM with shallow convection and deep convection, and MP-GCM with shallow and scale-adaptive deep convection. In the MP-GCM with shallow convection, fast eastward propagation and scattered pattern appeared. The MP-GCM with shallow convection and deep convection shows the slowed down eastward propagation and organized pattern, but the organization is excessive. The MP-GCM with shallow and scale-adaptive deep convection shows improvement of eastward propagation speed and organized pattern similar to the observation.

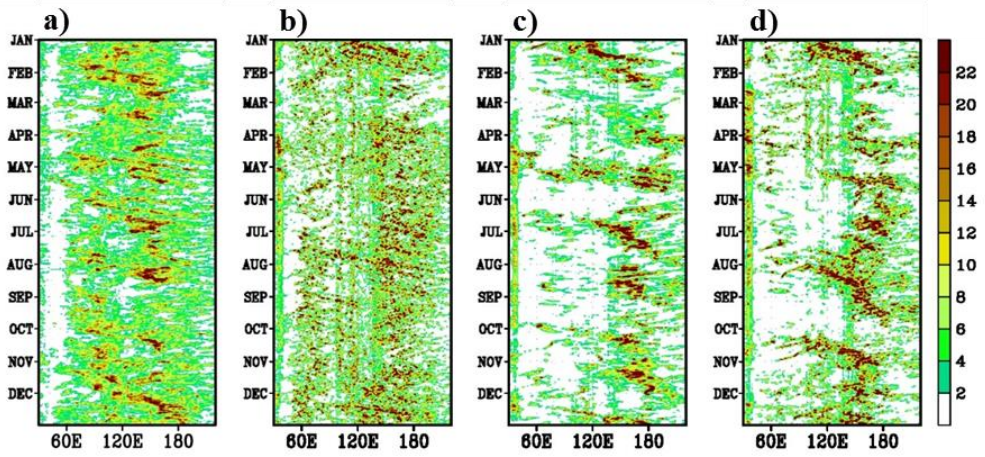

Figure 5.14. Longitude-time diagram of the daily mean precipitation averaged over 10°S–10°N from (a) TRMM, (b) MP-GCM with shallow convection, (c) MP-GCM with shallow convection and deep convection, and (d) MP-GCM with shallow and scale-adaptive deep convection.

6 MJO simulation intercomparison of developed MP-CGCM with CMIP5 models

6.1 MJO simulation in CMIP5 Climate Models

The MJO is analyzed using 20 years (1985-2004) of daily mean data from the historical runs obtained from the CMIP5 data portal (http://pcmdi9.llnl.gov). The MJO simulation diagnostics are applied to 37 models, while the process-oriented diagnostics are applied to a subset of these models because of limited data availability. The model designation, host institution, convection scheme, and stratiform cloud scheme are given in Table 1. The reader is referred to Taylor et al. (2012) for a more detailed description of the CMIP5 models.

	Model	Institution	Convection scheme / Modification	Cloud scheme / Modification
1	ACCESS1.0	CSIRO and BOM, Australia	Gregory and Rowntree (1990)	Smith (1990)/Wilson et al. (2004)
2	ACCESS1.3	CSIRO and BOM, Australia	Gregory and Rowntree (1990)/Hewitt et al. (2011)	Wilson et al. (2008)/Franklin et al. (2012)
3	BCC-CSM1.1	Beijing Climate Center, China	Zhang and McFarlane (1995)/Zhang and Mu (2005)	Rasch and Kristjansson (1998)
4	BCC-CSM1.1.m	Beijing Climate Center, China	Zhang and McFarlane (1995)/Zhang and Mu (2005)	Rasch and Kristjansson (1998)
5	BNU-ESM	BNU, China	Zhang and McFarlane (1995)/Neale et al. (2008);Richter and Rasch (2008)	Rasch and Kristjansson (1998)
6	CanCM4	CCCma, Canada	Zhang and McFarlane (1995)	McFarlane et al. (2005)
7	CanESM2	CCCma, Canada	Zhang and McFarlane (1995)	McFarlane et al. (2005)
8	CCSM4	NCAR, USA	Zhang and McFarlane (1995)/Neale et al.(2008);Richter and Rasch (2008)	Rasch and Kristjansson (1998)
9	CESM1-CAM5	NSF/DOE NCAR, USA	Zhang and McFarlane (1995)/Neale et al. (2008);Richter and Rasch (2008)	Morrison and Gettelman (2008).
10	CESM1-FASTCHEM	NSF/DOE NCAR, USA	Zhang and McFarlane (1995)/Neale et al. (2008);Richter and Rasch (2008)	Morrison and Gettelman (2008).
11	CMCC-CESM	CMCC, Italy	Tiedtke (1989)/Nordeng (1994)	Lohmann and Roeckner (1996)/ Tompkins (2002).
12	CMCC-CM	CMCC, Italy	Tiedtke (1989)/Nordeng (1994)	Lohmann and Roeckner (1996)/ Tompkins (2002).
13	CMCC-CMS	CMCC, Italy	Tiedtke (1989)/Nordeng (1994)	Lohmann and Roeckner (1996)/ Tompkins (2002).
14	CNRM-CM5	CNRM and CERFACS, France	Bougeault (1985)	Ricard and Royer (1993)
15	CSIRO-Mk3.6.0	CSIRO and QCCCE, Australia	Gregory and Rowntree (1990)/Gregory (1995)	Rotstayn (1997, 1998)/Rotstayn et al. (2000)
16	EC-EARTH	European Earth System	Tiedtke (1989)/Nordeng (1994)	Tiedtke (1993)
17	FGOALS-g2	IAP and THU, China	Zhang and McFarlane (1995)/Zhang and Mu (2005)	Rasch and Kristjansson (1998)/Morrison and Gettleman (2008)
18	FGOALS-s2	IAP and CAS, China	Tiedtke (1989)/Nordeng (1994)	Liu and Wu (1997)
19	GFDL-CM3	NOAA GFDL, USA	Donner (1993)/ Donner et al. 2001; Wilcox and Donner 2007	Tiedtke (1993)/Anderson et al. (2004).
20	GFDL-ESM2G	NOAA GFDL, USA	Moorthi and Suarez (1992)	Rotstayn (1997, 1998);Tiedtke (1993)/Rotstayn et al. (2000)
21	GFDL-ESM2M	NOAA GFDL, USA	Moorthi and Suarez (1992)	Rotstayn (1997, 1998);Tiedtke (1993)/Rotstayn et al. (2000)
22	HadCM3	Met Office Hadley Centre, UK	Gregory and Rowntree (1990)/Gregory and Allen (1991)	Rotstayn (1997, 1998)/Rotstayn et al. (2000)
23	HadGEM2-CC	Met Office Hadley Centre, UK	Gregory and Rowntree (1990)/Derbyshire et al. (2011)	Smith (1990)/Wilson and Ballard (1999).
24	HadGEM2-ES	Met Office Hadley Centre, UK	Gregory and Rowntree (1990)/Derbyshire et al. (2011)	Smith (1990)/Wilson and Ballard (1999).
25	INM-CM4	INM, Russia	Betts (1986)	Diagnostic calculation of cloud fraction
26	IPSL-CM5A-LR	IPSL, France	Emanuel (1991)	Bony and Emanuel (2001)
27	IPSL-CM5A-MR	IPSL, France	Emanuel (1991)	Bony and Emanuel (2001)
28	IPSL-CM5B-LR	IPSL, France	Grandpeix and Lafore (2010);Grandpeix et al., (2010)	Bony and Emanuel (2001)
29	MIROC4h	AORI, NIES, JAMSTEC, Japan	Arakawa and Schubert (1974);Pan and Randall (1998)/Emori et al. (2001)	Le Treut and Li (1991)
30	MIROC5	AORI, NIES, JAMSTEC, Japan	Chikira and Sugiyama (2010)	Watanabe et al. 2009; Wilson and Ballard (1999)
31	MIROC-ESM	AORI, NIES, JAMSTEC, Japan	Pan and Randall (1998)/Emori et al. (2001)	Le Treut and Li (1991)
32	MIROC-ESM-CHEM	AORI, NIES, JAMSTEC, Japan	Pan and Randall (1998)/Emori et al. (2001)	Le Treut and Li (1991)

33	MPI-ESM-LR	MPI, Germany	Tiedtke (1989)/Nordeng (1994)	Sundqvist et al. (1989),
34	MPI-ESM-MR	MPI, Germany	Tiedtke (1989)/Nordeng (1994)	Sundqvist et al. (1989),
35	MPI-ESM-P	MPI, Germany	Tiedtke (1989)/Nordeng (1994)	Sundqvist et al. (1989),
36	MRI-CGCM3	MRI, Japan	Tiedtke (1989)/Nordeng (1994);Yukimoto et al. (2011)	Tiedtke 1993;ECMWF 2004;Jakob 2000
37	NorESM1-M	Norwegian Climate Centre	Zhang and McFarlane (1995)/Neale et al.(2008);Richter and Rasch (2008)	Rasch and Kristjansson (1998)

Table 6.1. Description of CMIP5 models used in this study.

6.1.1 MJO simulation diagnostics and MJO skill metrics

The MJO simulation diagnostics developed by MJOWG are applied to 37 CMIP5 models and MJO skill metrics are formulated to capture a model's ability to simulate prominent features of the MJO, and report this ability in the form of a scalar. Statistical methods that have been employed to diagnose the realism of spatial and temporal scales and propagation characteristics of the MJO include 1) wavenumber-frequency power spectra (Hayashi 1982; Salby and Hendon 1990; Wheeler and Kiladis 1999), and 2) combined EOF (CEOF) analysis (Wheeler and Hendon 2004). These methods are components of the CLIVAR MJO simulation diagnostics (CLIVAR MJOWG 2009).

1) Wavenumber-frequency power spectrum analysis

The wavenumber-frequency power spectrum analysis assesses the distribution of variance (i.e. power) in the wavenumber-frequency domain and provides a convenient diagnostic of planetary-scale structure and behavior of the MJO. Figure 6.1 shows the wavenumber-frequency power spectra and the "MJO band" (eastward propagating, periods of 30-60 days, and wavenumbers

1-3) averaged coherence-squared (coh^2) of 10°S-10°N averaged precipitation (shaded) and U850 (contoured) obtained from observations and 37 CMIP5 models. The power spectra and coh^2 were calculated for each year and then averaged over all years. The observed spectral power of precipitation and the U850 are concentrated at the MJO band, whereas most CMIP5 models show a diverse range of spectral power over a broader range of periods and wavenumbers. In observations, the consistency between the space-time characteristics of precipitation and U850 is clear (coh^2 of observation is about 0.71), whereas most CMIP5 models show a lack of correspondence (the average coh^2 across models is about 0.6).

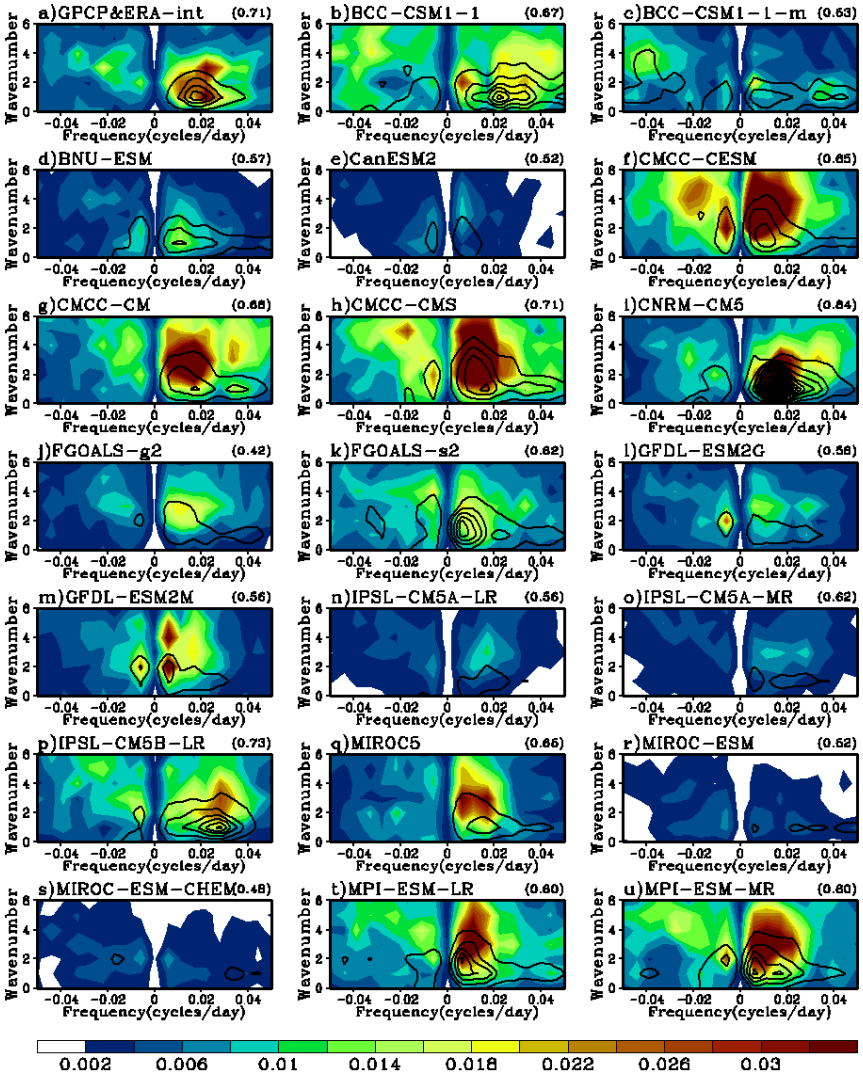

Figure 6.1. November-April wavenumber-frequency power spectra of 10°S-10°N averaged precipitation (shaded) and 850hPa zonal wind (contoured with 0.015 interval) and coh^2 (texted on the upper right of each plot) averaged over MJO band (period 30-60days and wavenumber 1-3). Power spectra and coh^2 were calculated for each year and then averaged over all years of data. Units of power spectra for the precipitation and 850hPa zonal wind are $mm^2\ day^{-2}$ and $m^2\ s^{-2}$ per frequency interval per wavenumber interval, respectively.

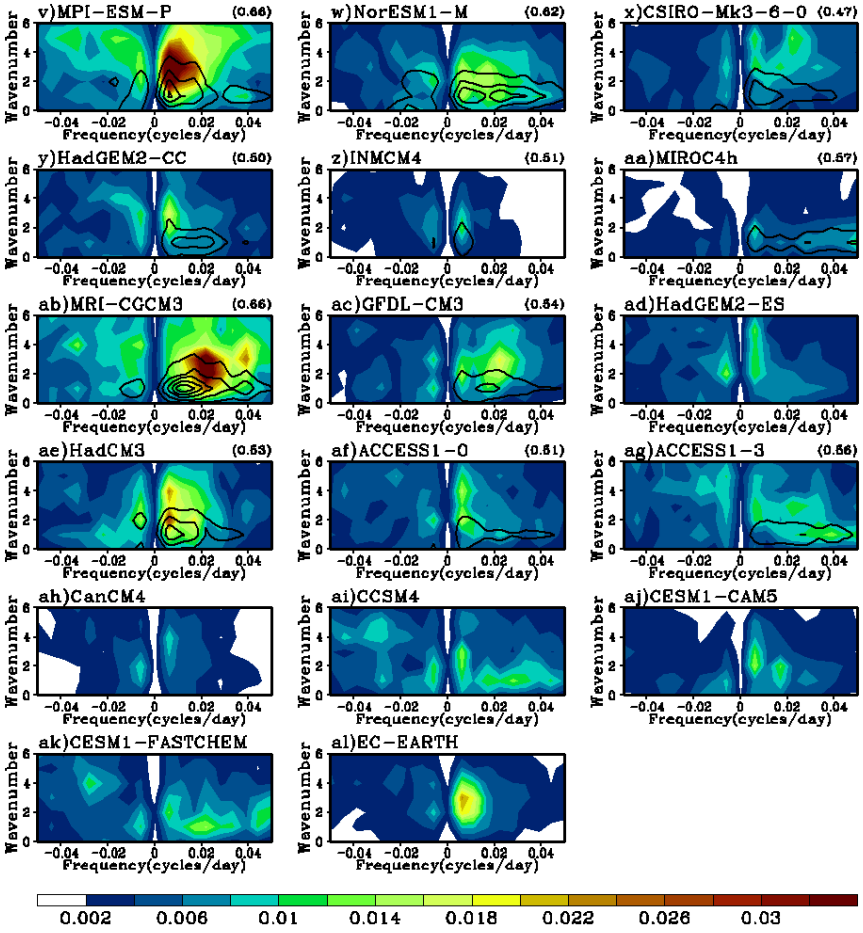

Figure 6.1. (continued).

For a quantitative evaluation of model simulations, four MJO simulation skill metrics are formulated from the wavenumber-frequency power spectra and the coh^2. The first skill metric is obtained by dividing the sum of spectral power over the MJO band by that of its westward propagating counterpart. This metric, which is often called as the Eastward/Westward power ratio (E/W ratio hereafter), indicates the robustness of eastward propagating feature of the MJO (Zhang and Hendon 1997) and has been frequently used in observational (e.g., Zhang and Hendon 1997; Hendon et al. 1999) and modeling studies (e.g., Lin et al. 2006; Kim et al. 2009).

The observed E/W ratio is about 2.3, 4.0, 4.2, and 2.8 for precipitation, OLR, U850, and U250, respectively (Figure 6.2a). This suggests that the observed MJO's eastward propagation is more robust in OLR and U850 than that in precipitation and U250. Most CMIP5 models underestimate the E/W ratio of all variables, especially that of OLR. As an exception, CNRM-CM5 shows outstandingly strong E/W ratios compared to other models, with that of U850 (11.1) out of range in the figure. A majority of the models exhibit E/W ratios of U850 that are greater than that of other variables, consistent with the

finding of Zhang et al. (2006). IPSL-CM5A-LR and IPSL-CM5B-LR are developed from same modeling center, but they exhibit substantially different E/W ratios, particularly in wind fields (difference between two models is about 3.2 and all CMIP5 inter-model spread is about 2 for the U850 E/W ratio). The change in MJO performance across models from the same center could be related to impacts from changing parameterization schemes among model versions. IPSL-CM5A-LR and IPSL-CM5B-LR use different convection and stratiform cloud schemes (Table 6.1). Kim et al. (2015) attributed the stronger MJO in IPSL-CM5B-LR to the stronger cloud-longwave radiation feedback in that model, likely due to the difference in parameterization schemes.

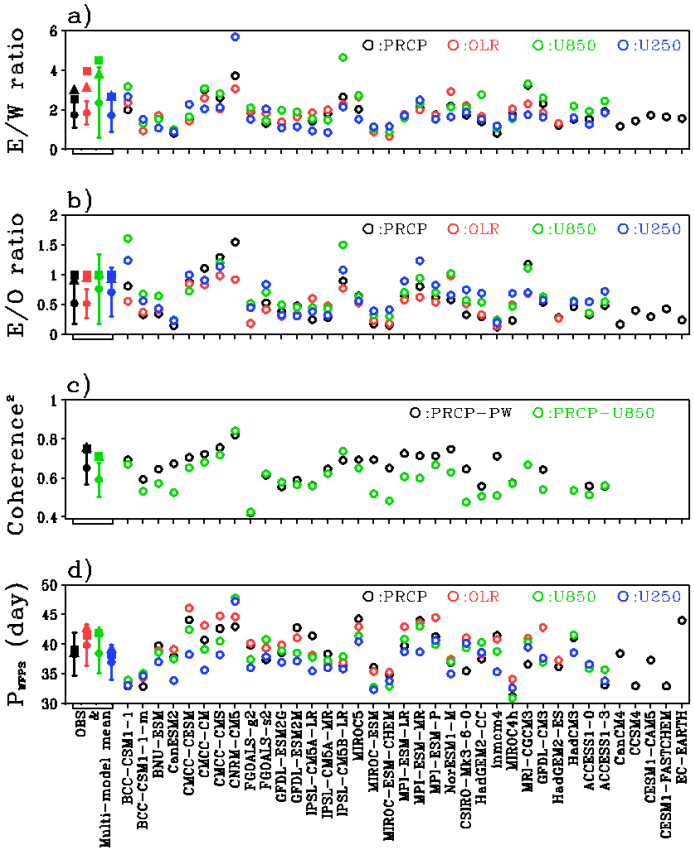

Figure 6.2. a) East/West power ratio (E/W ratio), b) Normalized East power by observation (E/O ratio), c) coh² of precipitation with precipitable water and U850, and d) dominant eastward period from the wavenumber-frequency power spectra (P_{WFPS}). Closed squares, closed triangles, closed circles, and open circles indicate observations (GPCP(1997-2010), AVHRR(1985-2004), ERA-int(1985-2004)), additional observations (TRMM(1998-2010), CERES(2001-2010), NCEP1(1984-2010)), multi-model means, and CMIP5 models, respectively. Vertical lines indicate inter-model spreads. Different color indicates each variable. The observed East powers for normalization of models are $0.02mm^2\ day^{-2}$, $1.20W^2\ m^{-4}$, $0.026m^2\ s^{-2}$, and $0.10m^2\ s^{-2}$ for the PRCP (GPCP), OLR (AVHRR), U850 and U250 (ERA-int), respectively. The value of CNRM-CM5's E/W ratio of U850 (11.1) and E/O ratio of U850 (3.44) and U250 (2.33) are out of range in the figure.

The second skill metric from the wavenumber-frequency power spectrum, which we refer to as the E/O ratio, is formulated by normalizing the sum of spectral power within the MJO band by the observed value. The observed values are $0.02\,mm^2\ day^{-2}$, $1.20\,W^2\ m^{-4}$, $0.026\,m^2\ s^{-2}$, and $0.10 m^2\ s^{-2}$ for precipitation, OLR, U850, and U250, respectively. The use of the second metric is complementary to the E/W ratio and it is motivated by the possibility that a model with large E/W ratio could still exhibit unrealistically small eastward propagating power. Figure 6.2b shows that most CMIP5 models underestimate the E/O ratios, especially for variables that are more directly related to convection (precipitation and OLR). As for the E/W ratio, CNRM-CM5 shows an excessively strong E/O ratio compared to other models, with the E/O ratio of U850 (3.44) and U250 (2.33) off scale in the figure. Models that show superior skill in the E/O ratio also perform better in the E/W ratio. Table 6.2 shows the correlation coefficient between the E/W ratios and the E/O ratios among the models. The correlation coefficient is especially high for U850 (0.93) and U250 (0.96). The high correlation between the E/W ratio and E/O ratio suggests that the E/W ratio is well correlated with eastward propagation

within MJO band. Thus, the E/W power ratio that has been used in many studies is a reasonable choice to assess how well a model captures the robust eastward propagation of the MJO.

		E/W ratio				E/O ratio				Coh^2		CEOF percent				Phase hov corr	CEOF EV corr			CEOF max corr.	Mean
		PRCP	OLR	U850	U250	PRCP	OLR	U850	U250	PRCP-PW	PRCP-U850	All	OLR	U850	U250	PRCP	OLR	U850	U250		
E/W ratio	PRCP		0.85	0.76	0.67	0.88	0.78	0.76	0.70	0.41	0.74	0.63	0.59	0.67	0.37	0.55	0.19	0.15	0.19	0.64	0.59
	OLR	0.85		0.63	0.57	0.67	0.73	0.64	0.59	0.32	0.63	0.61	0.60	0.68	0.32	0.47	0.21	0.16	0.16	0.65	0.53
	U850	0.76	0.63		0.90	0.73	0.52	0.93	0.82	0.40	0.69	0.73	0.51	0.75	0.57	0.41	0.15	0.19	0.23	0.67	0.59
	U250	0.67	0.57	0.90		0.76	0.57	0.93	0.96	0.50	0.68	0.80	0.51	0.72	0.77	0.51	0.16	0.12	0.28	0.71	0.62
E/O ratio	PRCP	0.88	0.67	0.73	0.76		0.80	0.81	0.81	0.58	0.84	0.66	0.52	0.61	0.55	0.62	0.21	0.09	0.24	0.61	0.61
	OLR	0.78	0.73	0.52	0.57	0.80		0.63	0.68	0.60	0.78	0.55	0.62	0.51	0.36	0.69	0.40	0.07	0.14	0.55	0.55
	U850	0.76	0.64	0.93	0.93	0.81	0.63		0.91	0.54	0.80	0.82	0.56	0.81	0.69	0.49	0.20	0.13	0.21	0.73	0.64
	U250	0.70	0.59	0.82	0.96	0.81	0.68	0.91		0.55	0.75	0.78	0.53	0.72	0.72	0.58	0.21	0.00	0.20	0.73	0.62
Coh^2	PRCP-PW	0.41	0.32	0.40	0.50	0.58	0.60	0.54	0.55		0.70	0.48	0.49	0.42	0.37	0.62	0.55	-0.12	0.00	0.41	0.44
	PRCP-U850	0.74	0.63	0.69	0.68	0.84	0.78	0.80	0.75	0.70		0.63	0.60	0.61	0.44	0.59	0.39	-0.06	-0.01	0.68	0.58
CEOF percent	All	0.63	0.61	0.73	0.80	0.66	0.55	0.82	0.78	0.48	0.63		0.76	0.93	0.86	0.64	0.40	0.36	0.49	0.85	0.66
	OLR	0.59	0.60	0.51	0.51	0.52	0.62	0.56	0.53	0.49	0.60	0.76		0.67	0.44	0.75	0.69	0.24	0.21	0.72	0.56
	U850	0.67	0.68	0.75	0.72	0.61	0.51	0.81	0.72	0.42	0.61	0.93	0.67		0.68	0.50	0.30	0.30	0.41	0.79	0.62
	U250	0.37	0.32	0.57	0.77	0.55	0.36	0.69	0.72	0.37	0.44	0.86	0.44	0.68		0.50	0.21	0.36	0.56	0.68	0.52
Phase hov corr	PRCP	0.55	0.47	0.41	0.51	0.62	0.69	0.49	0.58	0.62	0.59	0.64	0.75	0.50	0.50		0.80	0.29	0.34	0.60	0.55
CEOF EV corr	OLR	0.19	0.21	0.15	0.16	0.21	0.40	0.20	0.21	0.55	0.39	0.40	0.69	0.30	0.21	0.80		0.23	0.10	0.37	0.32
	U850	0.15	0.16	0.19	0.12	0.09	0.07	0.13	0.00	-0.12	-0.06	0.36	0.24	0.30	0.36	0.29	0.23		0.84	0.11	0.19
	U250	0.19	0.16	0.23	0.28	0.24	0.14	0.21	0.20	0.00	-0.01	0.49	0.21	0.41	0.56	0.34	0.10	0.84		0.19	0.27
CEOF PC max corr.		0.64	0.65	0.67	0.71	0.61	0.55	0.73	0.73	0.41	0.68	0.85	0.72	0.79	0.68	0.60	0.37	0.11	0.19		0.59

Table 2. Correlation coefficient between MJO skill metrics representing MJO propagation, coh^2, and amplitude in CMIP5 models.

The third skill metric is obtained by the MJO band averaged coh^2 of precipitation with U850 and precipitable water. The observed values of the coh^2 of precipitation with U850 and precipitable water are about 0.7 and 0.75, respectively. It indicates the strong coupling of precipitation with U850 and precipitable water. These results are consistent with those of Yasunaga and Mapes (2012) who also showed the coh^2 of precipitation with precipitable water in observations. Most CMIP5 models underestimate the coh^2 of precipitation with U850 and precipitable water. The CNRM-CM5, which simulated excessively strong E/W ratio and E/O ratio, shows larger coh^2 than other models and even observations. Table 6.2 shows the correlation between coh^2 and other MJO skill metrics. The coh^2 between precipitation and U850 is well correlated with the E/W ratio and the E/O ratio of all variables, especially the E/O ratio of precipitation and U850 that have a correlation greater than 0.8.

For the fourth skill metric we estimate the MJO periodicity (P_{WFPS}, Fig. 6.2d) by dividing the sum of power-weighted period (i.e. 1/frequency) by the sum of power over the period of 20-100 days and for each of these sums, considering only wavenumbers 1-3. In observations, the P_{WFPS} obtained from

the four variables used in this study ranges from 38 days (U250) to 42 days (U850). Some models (BCC-CSM1-1, BCC-CSM1-1-m, MIROC-ESM, MIROC-ESM-CHEM, and MIROC4h) exhibit shorter-than-observed periodicity across all four variables. These models also tend to show the E/W ratio and the E/O ratio that are smaller than that of other models. The CMCC model group (CMCC-CESM, CMCC-CM, CMCC-CMS) exhibits relatively large spread (~10 days) in P_{WFPS} estimated from different variables, with longer and shorter periodicity in OLR and U250, respectively. Overall, P_{WFPS} from U250 is shorter than those from other variables.

2) CEOF analysis

In the CEOF analysis (Wheeler and Hendon 2004), a standard EOF analysis is performed using three variables – OLR, U850, and U200. Each variable is meridionally averaged and normalized individually before being merged. The use of the combined field is motivated by the observation that the large-scale convective and circulation anomalies are tightly coupled. In observations, the leading pair of CEOFs of intraseasonal (20-100-day bandpass filtered) anomalies explains more than 40% of total intraseasonal variability and represents an eastward propagation with periodicity of about 40 days.

We calculate the CEOFs using 15°S-15°N averaged 20-100-day band-pass filtered variables, following the protocol of the MJOWG (2009). This is slightly different from the original method used by Wheeler and Hendon (2004), who used unfiltered fields since they were developing an approach useful for real-time monitoring and prediction. OLR, U850, and U250 (instead of U200) are used in the CEOF analysis because of limited data availability of the CMIP5 models. Nine models are excluded from the CEOF analysis because at least one of the three variables required was unavailable.

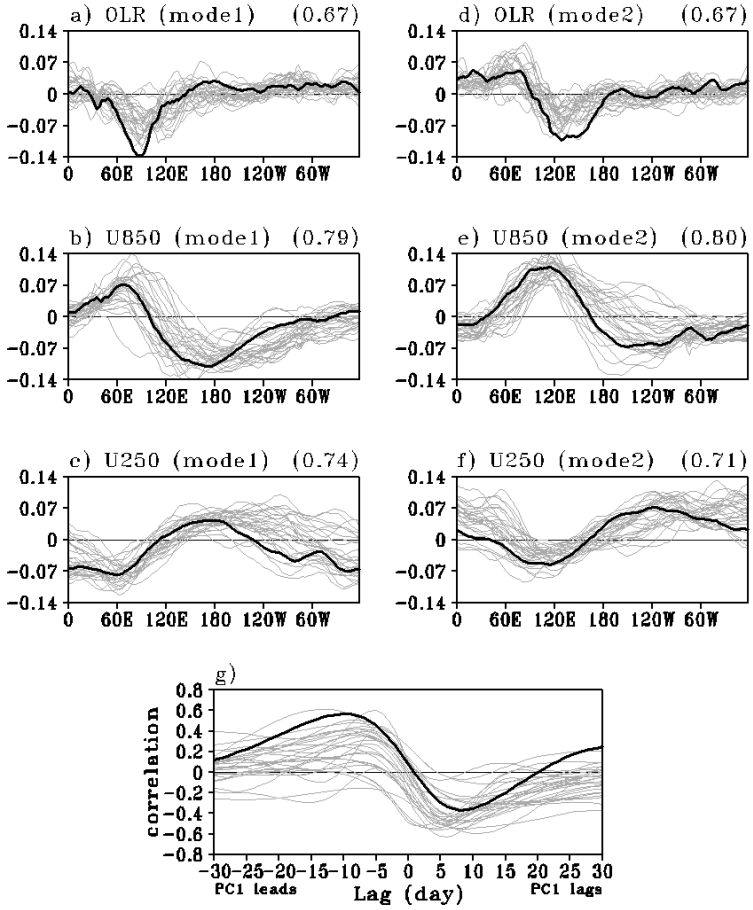

Figure 6.3. First two Combined EOF's eigenvector of 15°S-15°N averaged 20-100-day OLR, U850, and U250. a)-c) are first mode, and d)-f) are second mode. Sign and order of each Eigen mode are adjusted to be similar to observation. The values on the upper right of each plot indicate the mean of correlation coefficients between observation and each model. g) Lead-lag correlation of first two PC time series formulated by projecting the unfiltered anomaly data onto the Combined EOF's eigenvector. The thick black curves and thin grey curves indicate Observation and CMIP5 simulations, respectively.

Figure 6.3 shows the first two CEOFs from the observations and models, noting that the sign and order of the model eigenmodes are adjusted to best match observations. In observations, the first (second) CEOF mode captures a convective signal (negative OLR) centered at about 90°E (130°E) with associated low-level convergence and upper-level divergence. Most CMIP5 models simulate reasonably well the first two CEOF patterns, especially the circulation anomalies (mean values of spatial correlation coefficients along longitude between observations and each model are about 0.67, 0.79 and 0.73 for the OLR, U850 and U250, respectively). The magnitude of the peak convective signal over the warm pool tends to be weaker in the models compared to observations (Fig. 6.3a, d). Figure 6.3g also shows the lead-lag correlation of first two CEOF principal component time series (PCs) formulated by projecting the unfiltered anomaly data onto the CEOF's eigenvector. Because we use unfiltered anomalies to calculate PCs, it is not guaranteed that the PCs have the intraseasonal time scales. If a model has a variability of a shorter-than-intraseasonal time scale whose spatial patterns of OLR, U850, and U200 resemble that of the MJO, PCs and lag-correlation

between them would show the shorter time scale. In other words, using unfiltered anomalies in the calculation of PCs is a stricter test for GCMs than using filtered anomalies. In observations, the first CEOF mode (convection center over the Indian Ocean) leads the second CEOF mode (convection center over the west Pacific) by about 10 days, indicating the eastward propagation of MJO from Indian Ocean to Western Pacific. The models are in general able to capture the lead-lag relationship between the two leading modes, while they show large spread in values of maximum correlation, and the lag day at which the correlation maximizes. Most models simulate lower correlations between the leading PCs than observed.

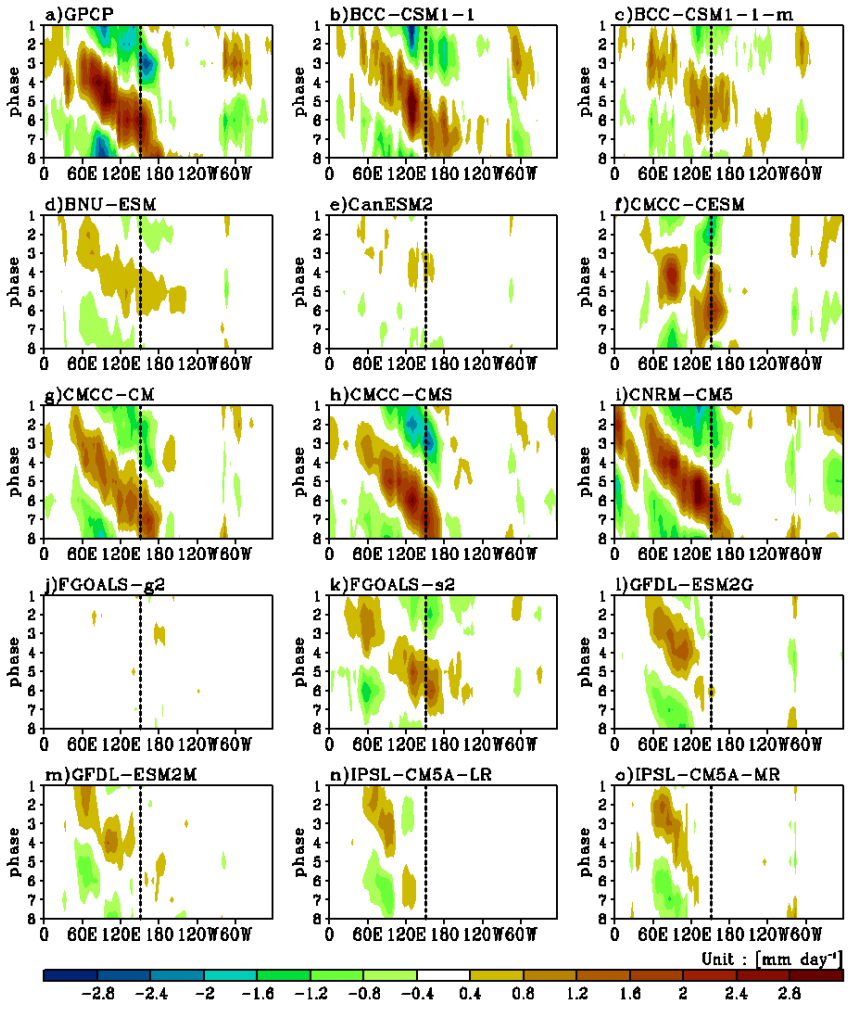

Figure 6.4. Hovmöller diagrams of MJO phase composited 20-100-day precipitation averaged 10°S-10°N. The MJO phase composites are based on the PC time series formulated by projecting the 20-100-day filtered anomaly data onto the CEOF's eigenvector shown in figure 3. The vertical dotted lines in each plot indicate the 150°E longitude.

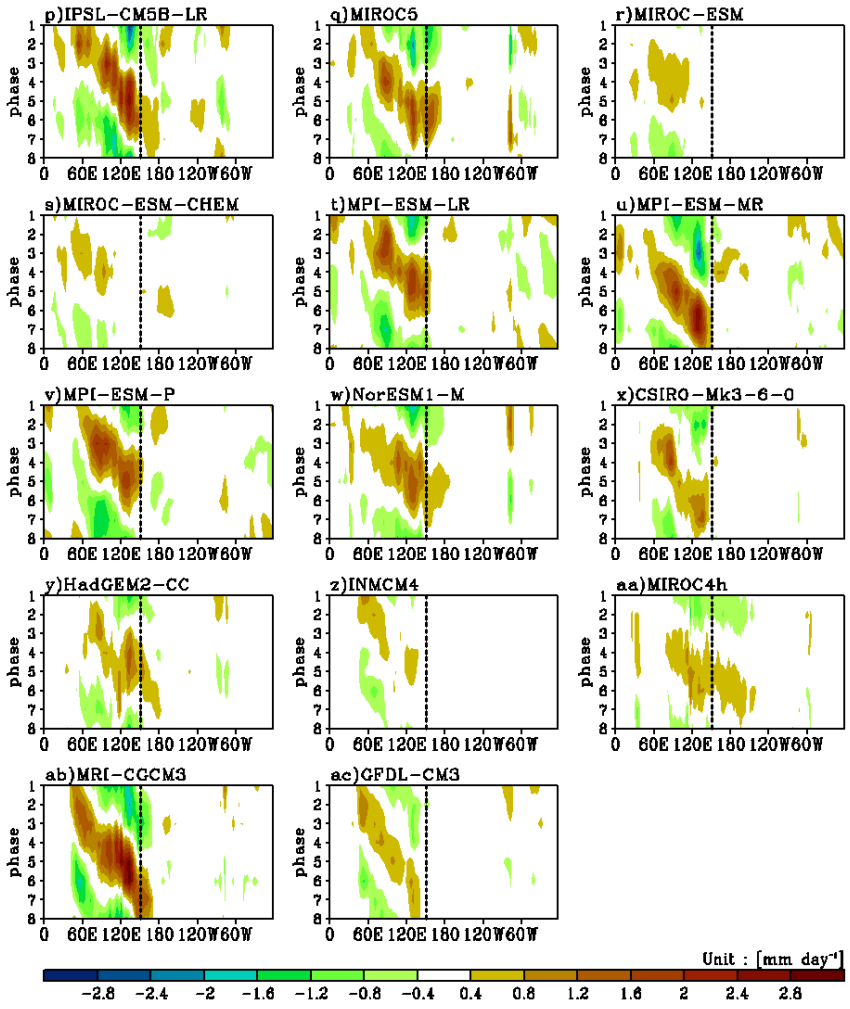

Figure 6.4. (continued).

In order to visualize the propagation of the MJO represented in each model, Fig. 6.4 shows the hovmöller diagrams of MJO-phase composited 20-100-day precipitation averaged 10°S-10°N. The MJO phase composites are based on the phase-space plots of the PC time series formulated by projecting the 20-100-day filtered anomaly data onto the CEOF's eigenvector, as described in MJOWG (2009). In observations, the MJO rainfall signal propagates from Indian Ocean to Western Pacific, whereas many CMIP5 models fail to produce coherent eastward propagation of MJO rainfall signal compared to observed. Some models struggle to get signal into Western Pacific (BCC-CSM1-1-m, BNU-ESM, FGOALS-s2, NorESM1-M, HadGEM2-CC, MIROC4h), some models have standing oscillation over Maritime Continent (GFDL-ESM2G, GFDL-ESM2M, IPSL-CM5A-LR, IPSL-CM5A-MR, MIROC-ESM, MIROC-ESM-CHEM, INMCM4), and some models show very weak signal over all longitude (CanESM2, FGOALS-2g). For example, when considering the 150°E as a criteria region, only about 6-8 out of 28 CMIP5 models propagate MJO rainfall signal east of 150°E reasonable well (BCC-CSM1-1, CMCC-CM, CMCC-CMS, CNRM-CM5, IPSL-CM5B-LR, MRI-

CGCM3). Hung et al. (2013) and Jiang et al. (2015) showed similar results using lead-lag correlation diagram of MJO time-scale filtered precipitation.

Four skill metrics are derived from the CEOF analysis. The first metric is the percentage variance explained by the two leading modes. In observations, the leading two CEOFs explain about 41% of the total variance (Figure 6.5a). These two modes also explain 59%, 39%, and 31% of the variance of U850, U250, and OLR respectively. The percentages of variance explained for individual variables are obtained by the spatial variance of power (square root of eigen value) weighted eigenvectors for individual variables. The sequence of variance explained by each variable of the CEOF is well simulated in CMIP5 models, but most CMIP5 models underestimate the magnitude of the variance explained by each variable, especially for OLR.

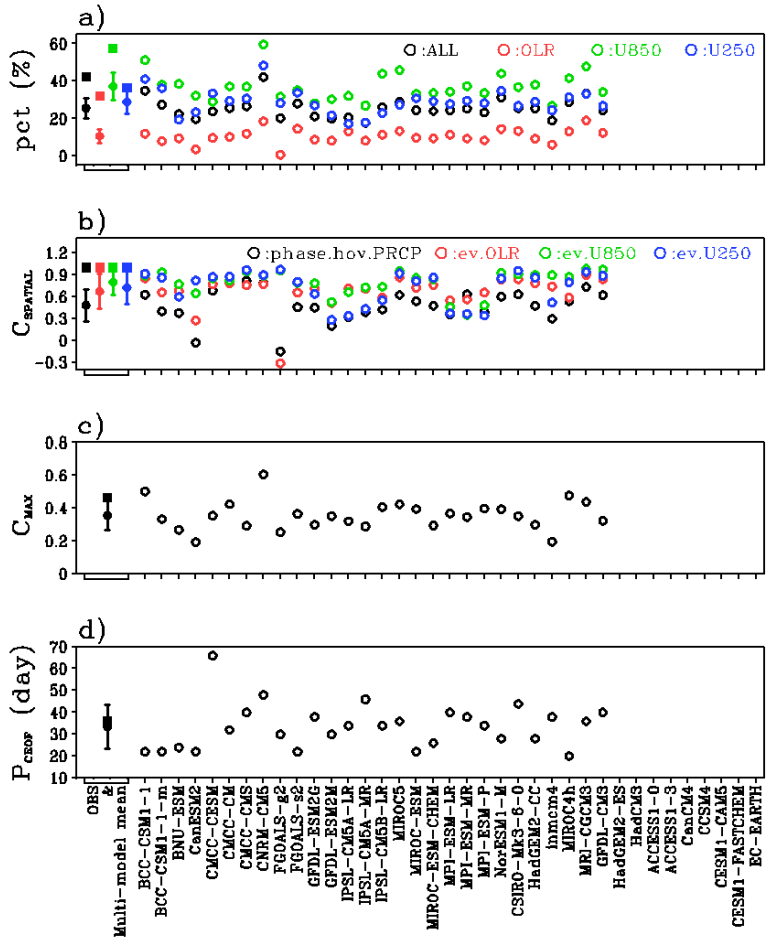

Figure 6.5. a) Percentage variance (pct) obtained from sum of first two combined EOF modes, b) spatial correlation between observation and models for MJO phase hovmuller diagram averaged 10°S-10°N and first two combined EOF's eigen modes, c) maximum correlation (C_{MAX}) between first two combined EOF's PC time series, and d) dominant eastward period from the first two combined EOF modes (P_{CEOF}). Closed squares, closed circles, and open circles indicate observations, multi-model means, and CMIP5 models, respectively. Vertical lines indicate inter-model spreads. Different color indicates each variable.

The second skill metric is obtained from the spatial correlation coefficients between observations and models for the hovmöller diagrams of MJO phase composited precipitation in Fig. 6.4 and for the first two CEOFs in Fig. 6.3. For the skill metric of the first two CEOFs, the spatial correlation coefficients of mode-1 and mode-2 are averaged to produce a single scalar metric. In the models, the lowest spatial correlation coefficient of the CEOFs appeared in the OLR among three variables. The FGOALS-g2 showed an especially large difference of correlation coefficient between OLR and other wind variables. The FGOALS-g2 showed weak coupling of precipitation with the wind field and moisture (Fig. 6.2c and Fig. 6.7a). The multi-model mean of the spatial correlation coefficients for the hovmöller diagrams of MJO phase composited precipitation is about 0.48.

The third and fourth skill metrics are derived from the lead-lag correlation between PCs of the two leading modes (Fig. 6.3g). The third metric, a measure of the coherency in the MJO propagation, is formulated by averaging the absolute values of maximum and minimum lead-lag correlation coefficients (c.f. Sperber and Kim 2012). The third metric will be referred to

C_{max}. The observed C_{max} is about 0.47, whereas the value of CMIP5 multi-model mean is about 0.36 indicating that most CMIP5 models' MJO propagation is not as coherent as observed. The fourth metric, an estimate of MJO periodicity from the CEOF analysis (P_{CEOF}), is formulated by twice the time interval between maximum lag-correlation and minimum lag-correlation. The observed P_{CEOF} is about 36 days, whereas the value of CMIP5 multi-model mean is about 34 days, which is similar to P_{WFPS} (Fig. 6.2d). The correlation coefficients between the modeled values for P_{CEOF} and P_{WFPS} are 0.58, 0.69, 0.63, and 0.58 for precipitation, OLR, U850, and U250, respectively (Table 6.3).

		Period from WFPS				Period from CEOF	Mean
		PRCP	OLR	U850	U250		
Period from WFPS	PRCP		0.82	0.77	0.59	0.58	0.69
	OLR	0.82		0.81	0.73	0.69	0.77
	U850	0.77	0.81		0.88	0.63	0.77
	U250	0.59	0.73	0.88		0.58	0.70
Period from CEOF		0.58	0.69	0.63	0.58		0.62

Table 6.3. Correlation coefficient between MJO skill metrics representing MJO period in CMIP5 models.

6.1.2 Process-oriented diagnosis

The process-oriented diagnostics aim to provide insights into how parameterizations of physical processes in GCMs can be modified to improve the MJO simulation. Here we study three process-oriented diagnostics (RHCP-, NGMS-, and GEF-diagnostics; see Section 1). Scalar metrics are derived from each process-oriented diagnostic to investigate their relationship with the MJO skill metrics.

To formulate the RHCP-diagnostic presented by Kim et al. (2014), the low-level (850-700hPa) RH composite based on precipitation percentile is performed over the Indo-Pacific warm pool (60°E-180°E, 15°S-15°N) with land masked out (Fig. 6.6).

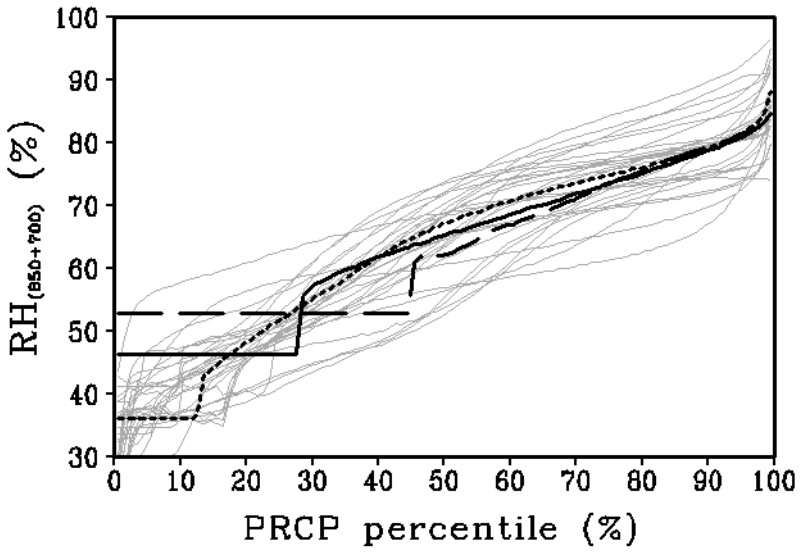

Figure 6.6. Relative Humidity Composite based on PRCP percentile (RHCP) averaged between 850hPa and 700hPa level. Indian Ocean area (60°E-180°E, 15°S-15°N) is used and land area is excluded in calculation. Thick black solid, long-dash, short-dash curves indicate GPCP (1997-2010), TRMM (1998-2010), ERA-int (1985-2004) precipitation respectively combined with ERA-interim RH, and thin grey curves indicate CMIP5 simulations.

In observations, the low-level RH increases as the precipitation percentile increases, indicating coupling between convection and low-level moisture. Most CMIP5 models exhibit a low-level RH increase as the precipitation percentile increases, but the RH for a given precipitation percentile can vary substantially compared to the observations. To objectively evaluate the relationship between convection and low-level moisture, the RHCP-metric is formulated as the low-level RH difference between upper 10% precipitation percentile and lower 20% precipitation percentile (Kim et al. 2014):

$$RHCP\ metric = \overline{RH}_{850+700}^{upper10\%} - \overline{RH}_{850+700}^{lower20\%}$$

The observed RHCP-metric ranges from 28.8 to 42.5, depending on the precipitation dataset used in the analysis (Fig. 6.7a). The large uncertainty of the observed RHCP-metric is caused by the uncertainty of the magnitude of weak precipitation (less than about the 45 percentile). Most CMIP5 models show RHCP-metric values that are within the uncertainty range of observed values (Fig. 6.7a).

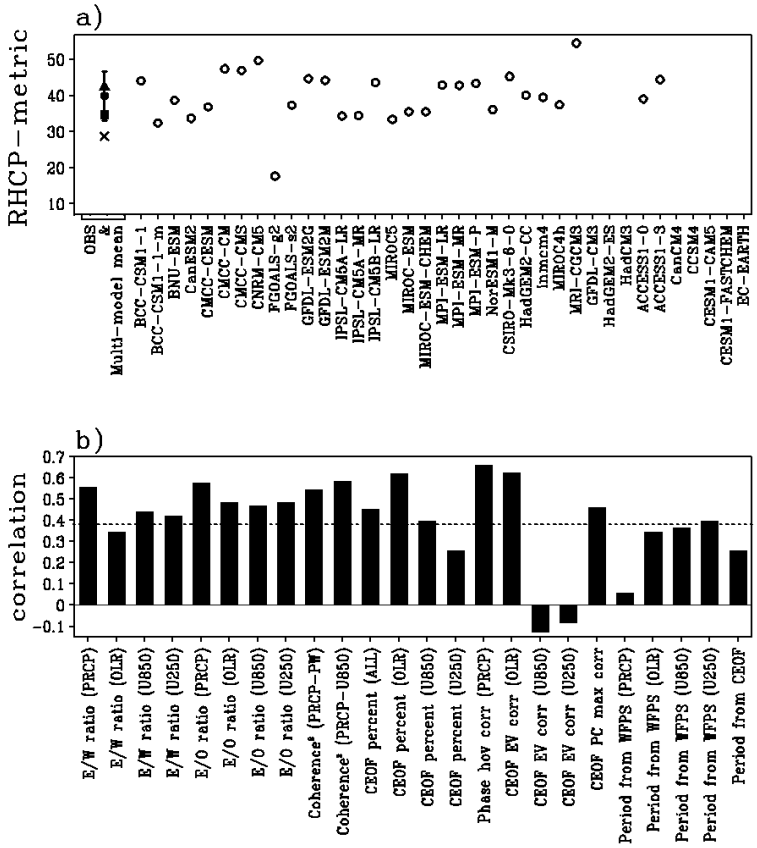

Figure 6.7. a) RHCP-metric for the observation and CMIP5 simulations. Closed square, X mark, closed triangle, closed circle, and open circles indicate GPCP (1997-2010), TRMM (1998-2010), ERA-int (1985-2004), multi-model mean, and CMIP5 models, respectively. Vertical lines indicate the inter-model spread. b) Correlation coefficient between RHCP-metric and MJO skill metrics. Dotted line indicates 5% significance level when 27models are used.

The correlation between the simulated RHCP-metric and various MJO skill metrics is assessed in Fig. 6.7b. The RHCP-metric is significantly correlated with most MJO skill metrics, including the E/W ratio and E/O ratio of precipitation, coh^2 of precipitation with precipitable water and U850, CEOF percentage variance of OLR, the spatial correlation between observations and models for the MJO phase hovmöller diagram, and for the CEOF eigenvector of OLR for which R~0.6. This indicates that models with stronger (weaker) coupling strength between low-tropospheric moisture and convection have a better (poorer) MJO. For models with too weak a coupling strength, improvement in this quantity would lead to a better MJO. Even considering the highest correlation score between this diagnostic and MJO skill, this only leads to an explained variance of about 35-40%, and thus additional parameterized quantities have to be investigated to more fully improve MJO fidelity.

In many previous studies, the gross moist stability (GMS) is presented to examine the relationship between convection and large-scale circulation. For example, Benedict et al. (2014) showed that the E/W ratio of precipitation is

more related to the vertical component of normalized GMS (NGMS) than the horizontal component of NGMS. The relationship between vertical component of NGMS obtained from the mean state and various MJO skill metrics are examined in this study. The NGMS-metric is formulated using the time-mean vertical profiles of omega, moist static energy (MSE), and dry static energy (DSE) over the Indo-Pacific warm pool area (60°E-180°E, 15°S-15°N) with land masked out:

$$NGMS\ \ metric = \frac{< \bar{\omega} \frac{\partial \overline{MSE}}{\partial p} >}{< \bar{\omega} \frac{\partial \overline{DSE}}{\partial p} >}$$

where the over-bar indicates the time mean, angle bracket indicates the column vertical integration from 1000hPa to 100hPa, $MSE = CpT + gz + Lq$ is the moist static energy, and $DSE = CpT + gz$ is the dry static energy. The magnitude and shape of the mean vertical profile of omega is diverse across the CMIP5 models, and the MSE of all levels is underestimated in most CMIP5 models (Fig. 6.8). The NGMS-metric is mainly influenced by the combination of mean vertical profiles of omega and MSE.

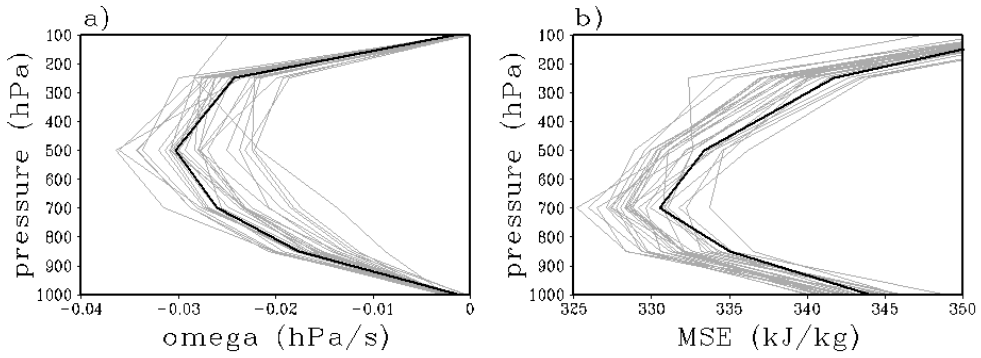

Figure 6.8. Vertical profiles of Indo-Pacific warm pool area (60°E-180°E, 15°S-15°N) averaged a) omega and b) Moist static energy (MSE) for the observation (thick black curve) and CMIP5 simulations (thin grey curves). Land area is excluded in calculation.

The NGMS-metric is about 0.25 for the observations and about 0.33 for the multi-model mean with many CMIP5 models overestimating the NGMS-metric (Fig. 6.9a). This indicates that most CMIP5 models more efficiently discharge MSE from the column through vertical convective motions compared to the observations. The simulated NGMS-metric has a significant negative correlation with half of the MJO skill metrics, including the E/W ratio and E/O ratio of most variables, P_{WFPS} of most variables, and P_{CEOF} (Fig. 6.9b). It indicates that a smaller NGMS, which means a less efficient discharge of MSE from the column through vertical convective motions, should result in a stronger MJO amplitude and improved propagation, and a slower and more realistic MJO propagation speed.

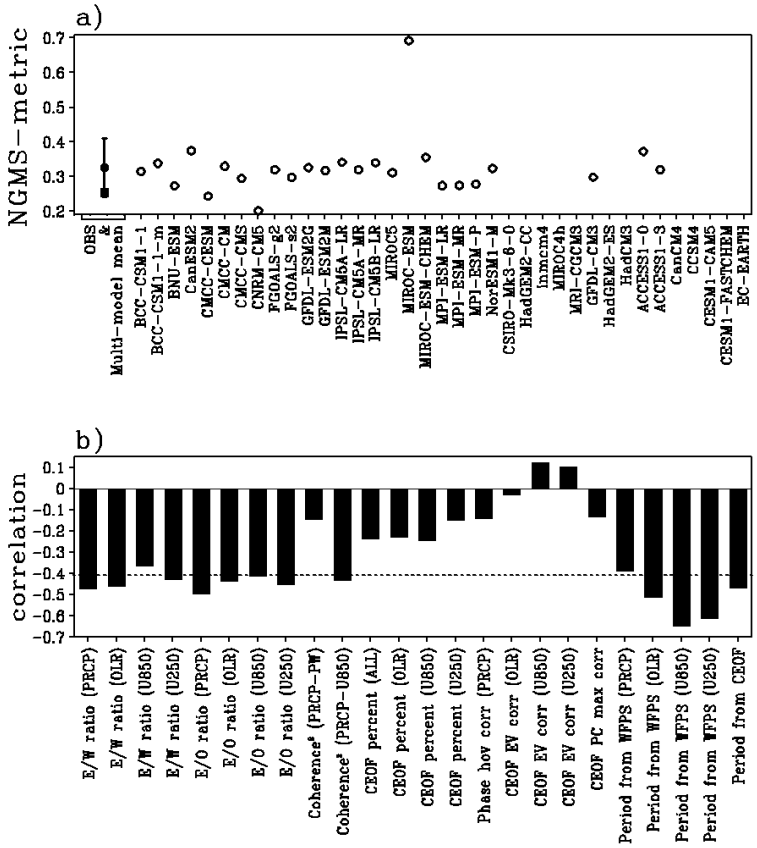

Figure 6.9. a) Normalized Gross Moist Stability (NGMS) metric for the observation and CMIP5 simulations. Closed square, closed circle, and open circles indicate observation, multi-model mean, and CMIP5 models, respectively. Vertical lines indicate the inter-model spread. b) Correlation coefficient between NGMS-metric and MJO skill metrics. Dotted line indicates 5% significance level when 23models are used.

For the third process-oriented diagnostic we use the GEF-diagnostic presented by Kim et al. (2015). It is calculated over the Indo-Pacific warm pool area (60°E-180°E, 15°S-15°N) with land masked out, as the ratio of column-integrated longwave radiative heating to column-integrated latent heating and is calculated on each precipitation anomaly bin (Fig. 6.10):

$$GEF = \frac{-OLR\ anomaly}{L \times PRCP\ anomaly}$$

where the $L = 2.5 \times 10^6\ J\ kg^{-1}$ is latent heat of condensation. The surface longwave anomaly is assumed to be small, hence the OLR anomaly is used as a measure of the column-integrated longwave radiative heating anomaly. In observations and in models, the maximum GEF tend to appear in relatively weak precipitation anomaly regimes, and the GEF decreases as the precipitation anomaly increases. This indicates that the cloud-longwave radiation feedback is larger in the weak precipitation anomaly regime than that in the strong precipitation anomaly regime. All CMIP5 models underestimate the GEF in the weak precipitation anomaly, but the GEF in the strong precipitation anomaly is relatively well simulated.

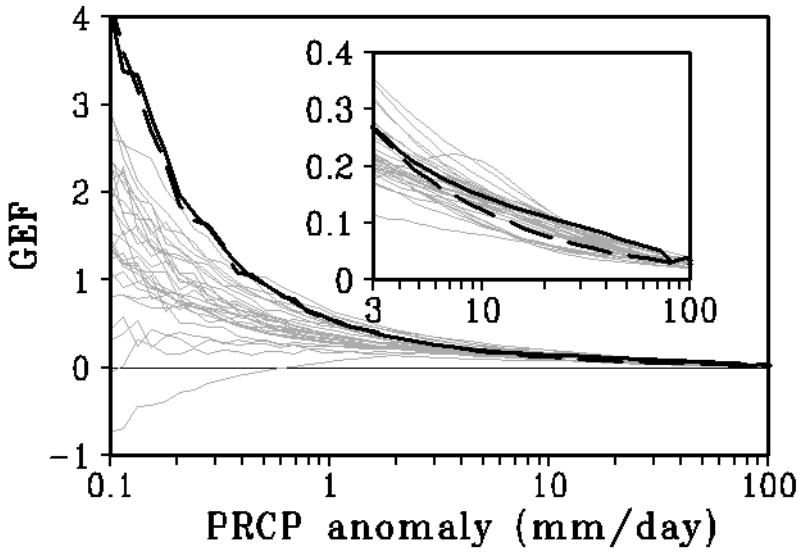

Figure 6.10. Greenhouse Enhancement Factor (GEF) diagnostics for the observation (AVHRR and GPCP (1997-2010): thick black curve, AVHRR and TRMM (1998-2010): long-dashed curve) and CMIP5 simulations (thin grey curves). Indo-Pacific warm pool area (60°E-180°E, 15°S-15°N) is used and land area is excluded in calculation. Note that precipitation anomaly is in log-scale. The inset plot is expanded plot with different range of x and y axis.

Kim et al. (2015) found that the maximum correlation between the E/W ratio of precipitation and the GEF appeared when the latter was quantified using only the weak precipitation anomaly regime. Accordingly, they formulated the GEF-metric as the weighted average of GEF over 1-5mm/day precipitation anomaly regime. The GEF-metric is about 0.31 for the observations and about 0.25 for the multi-model mean, with most CMIP5 models underestimating the GEF-metric (Fig. 6.11a). The correlation between the simulated GEF-metric and various MJO skill metrics is presented in Figure 6.11b. Compared to the RHCP- and NGMS-metric, the GEF-metric does not show as robust a relationship with the MJO skill metrics. The GEF-metric is most correlated with the E/W ratio of precipitation and the E/O ratio of precipitation and OLR. This suggests that the MJO in the CMIP5 models has the possibility to improve with an increase of longwave radiative heating in the weak precipitation anomaly regime. To increase the longwave radiative heating in the weak precipitation anomaly regime, the parameterizations of cloud properties and cloud-radiation interaction need to be modified. Kim et al. (2015) showed that the model with strong longwave radiative heating in the

weak precipitation anomaly has a larger cloud fraction, larger cloud ice water content, lower cloud liquid water content, and larger precipitable water.

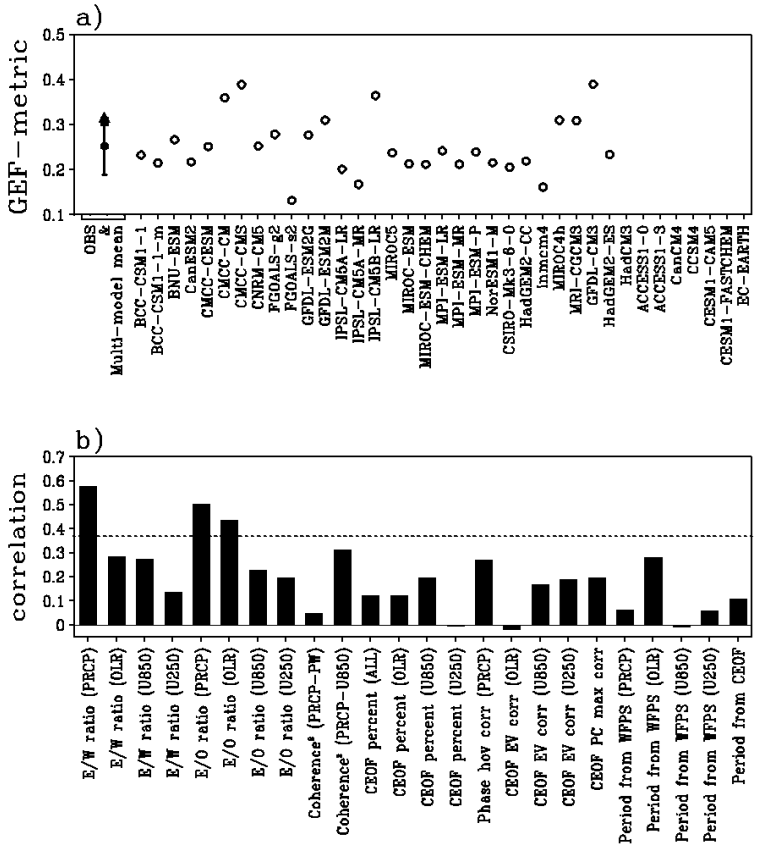

Figure 6.11. a) GEF-metric for the observation and CMIP5 simulations. Closed square, closed triangle, closed circle, and open circles indicate observation (AVHRR and GPCP (1997-2010)), additional observation (AVHRR and TRMM (1998-2010)), multi-model mean, and CMIP5 models, respectively. Vertical lines indicate the inter-model spread. b) Correlation coefficient between GEF-metric and MJO skill metrics. Dotted line indicates 5% significance level when 28models are used.

6.2 MJO simulation in developed MP-CGCM

The 50km resolution atmosphere-ocean coupled GCM with comprehensive cloud microphysics and appropriate vertical mixing (MP-CGCM) is developed based on MP-AGCM. Same parameterizations are implemented to the MP-AGCM and MP-CGCM.

The MJO simulation of the MP-CGCM is evaluated by intercomparison with CMIP5 models. Figure 6.12 shows November-April wavenumber-frequency power spectra of 10°S-10°N averaged precipitation and 850hPa zonal wind for the observation, CMIP5 models, previous SNUCGCM and developed SNUCGCM with comprehensive cloud microphysics and appropriate vertical mixing. The previous SNUCGCM poorly simulates the MJO, whereas the developed SNUCGCM well simulate the MJO compared to observation and CMIP5 models.

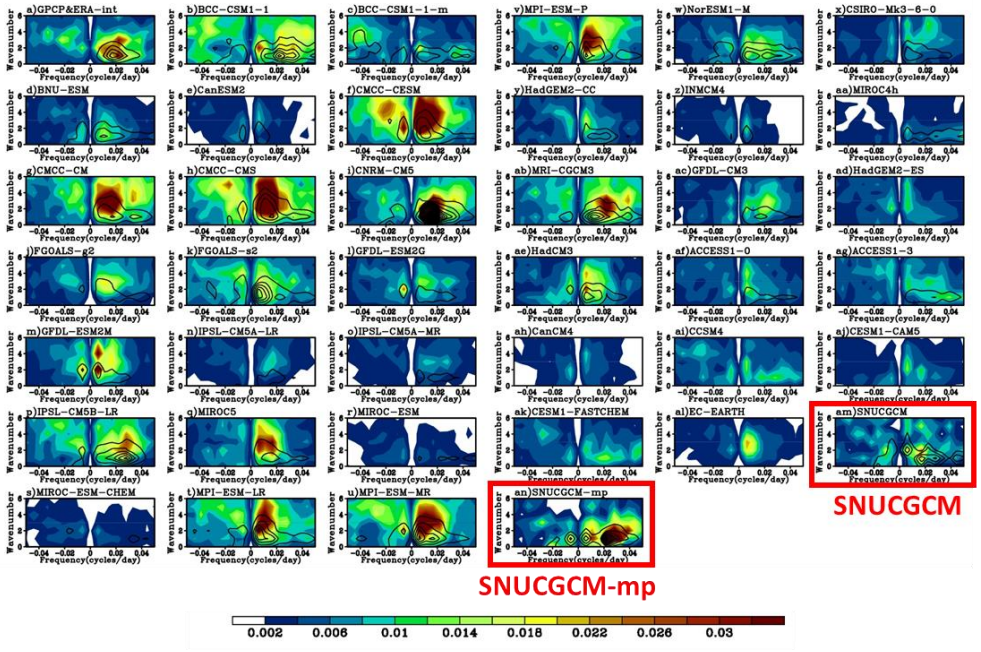

Figure 6.12. November-April wavenumber-frequency power spectra of 10°S-10°N averaged precipitation (shaded) and 850hPa zonal wind (contoured with 0.015 interval) for the observation, CMIP5 models, SNUCGCM and SNUCGCM-mp. Power spectra were calculated for each year and then averaged over all years of data. Units of power spectra for the precipitation and 850hPa zonal wind are $mm^2\,day^{-2}$ and $m^2\,s^{-2}$ per frequency interval per wavenumber interval, respectively.

To examine the important processes to simulate the strong MJO in SNUCGCM-mp compared to SNUCGCM, two process-oriented diagnostics are conducted. One is the RHCP-metric which examines the convective-moisture coupling strength. Another is the GEF-metric which examines the longwave radiation feedback. In the RHCP metric (Fig. 6.13), the SNUCGCM underestimates the convective-moisture coupling strength compared to observations and CMIP5 models, whereas the SNUCGCM-mp relatively well simulates it. It indicates that the comprehensive cloud microphysics improves the convective-moisture coupling in GCMs.

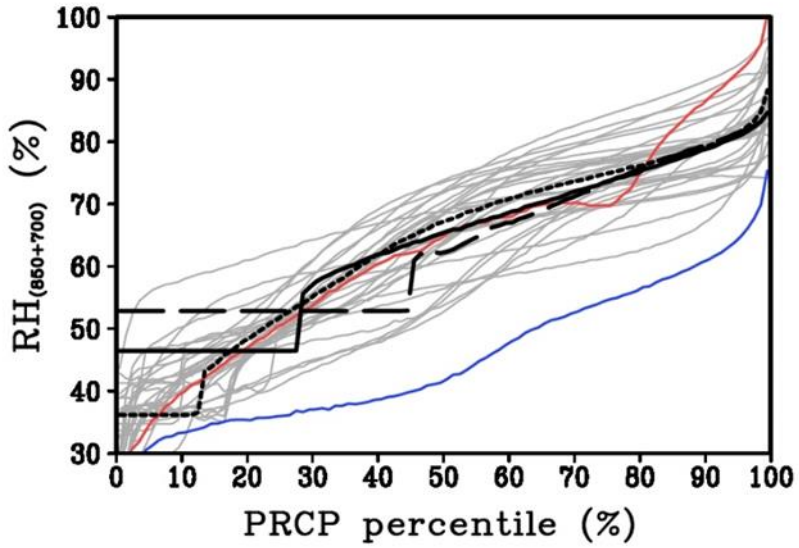

Figure 6.13. Relative Humidity Composite based on PRCP percentile (RHCP) averaged between 850hPa and 700hPa level. Indian Ocean area (60°E-180°E, 15°S-15°N) is used and land area is excluded in calculation. Thick black solid, long-dash, short-dash curves indicate GPCP (1997-2010), TRMM (1998-2010), ERA-int (1985-2004) precipitation respectively combined with ERA-interim RH, thin grey curves indicate CMIP5 simulations, blue curve and red curve indicate the SNUCGCM and SNUCGCM-mp, respectively.

In the GEF-metric (Fig. 6.14), the SNUCGCM underestimates the longwave radiation feedback compared to observations, whereas the SNUCGCM-mp relatively well simulates it. It indicates that the comprehensive cloud microphysics improves the longwave radiation feedback in GCMs. The improvement of the longwave radiation feedback would be related to more hydrometeors. The SNUCGCM-mp has 6 hydrometeors (water vapor, cloud liquid water, cloud ice water, rain water, snow, and graupel) as a prognostics variable, whereas the SNUCGCM has only 2 hydrometeors (water vapor and cloud water) as a prognostics variable.

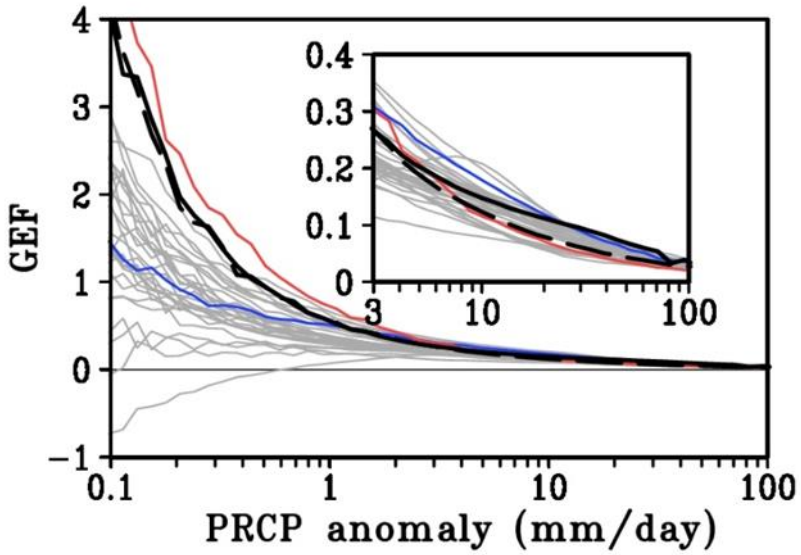

Figure 6.14. Greenhouse Enhancement Factor (GEF) diagnostics for the observation (AVHRR and GPCP (1997-2010): thick black curve, AVHRR and TRMM (1998-2010): long-dashed curve), CMIP5 simulations (thin grey curves), SNUCGCM (blue curve) and SNUCGCM-mp (red curve). Indo-Pacific warm pool area (60°E-180°E, 15°S-15°N) is used and land area is excluded in calculation. Note that precipitation anomaly is in log-scale. The inset plot is expanded plot with different range of x and y axis.

7 Summary and Discussion

7.1 Summary

The 50km GCM with modified cloud microphysics and shallow convection was developed by Kang et al. (2015). The cloud microphysics is modified based on GCE simulations with different horizontal resolutions. To overcome the resolution dependency of cloud microphysics, the condensation RH criteria and terminal velocity are modified. In the 50km resolution GCM, the convection scheme and large-scale condensation scheme are replaced by the modified cloud microphysics, and the shallow convection scheme is added to compensate a weak vertical mixing in sub-grid scale. Developed GCM shows the significant improvements in simulation of the heavy precipitation, the MJO propagation and moisture distribution varied with MJO time scale.

However, the developed GCM with modified cloud microphysics and shallow convection overestimates low-level cloud water and cloud fraction, and underestimates the mid-level specific humidity and upper-level cloud ice. It indicates that this model is required more additional vertical mixing. For the

appropriate vertical mixing to the 50km GCM with modified cloud microphysics, the shallow convection and scale-adaptive deep convection are implemented. Appropriate ratio of unresolved sub-grid scale vertical transport to total vertical transport is obtained from the 3-dimensional CRM with 1km horizontal resolution simulation. The moist static energy equation is used to assess the ratio of unresolved sub-grid scale vertical transport to total vertical transport. Implementation of scale-adaptive deep convection induces well simulation of vertical profiles of temperature and moisture.

The final goal of this study is development of coupled GCM with comprehensive cloud microphysics and appropriate vertical mixing. Based on understanding of cloud microphysics in AGCM with comprehensive cloud microphysics, a coupled GCM with comprehensive cloud microphysics was developed. A coupled GCM with comprehensive cloud microphysics shows better performance in the mean precipitation simulation compared to conventional coupled GCM and the MJO simulation compared to conventional coupled GCM and CMIP5 models.

7.2 Discussion on important issues for 50km GCM with cloud microphysics

7.2.1 Model time step

In general, the model time step decreases as the model resolution increases to avoid blowing up. But, decreasing model time step can induce a different result because the physics parameterizations are set to previous time step. Figure 7.1 shows the precipitation mean state for TRMM, AGCM with 200km, 100km, and 50km resolution. Δt of 200km simulation is 40 minutes, 100km simulation is 20 minutes, and 50km simulation is 10 minutes. As the model resolution increases and time step decreases, the precipitation strength becomes weak in globally. Figure 7.2 shows the Mean state of convective precipitation and large-scale precipitation for same simulations with Fig. 7.1. The convective precipitation is not much changed, but the large-scale precipitation is decreased as the model resolution increases and time step decreases. It indicates that the large-scale precipitation is sensitive to model resolution and time step.

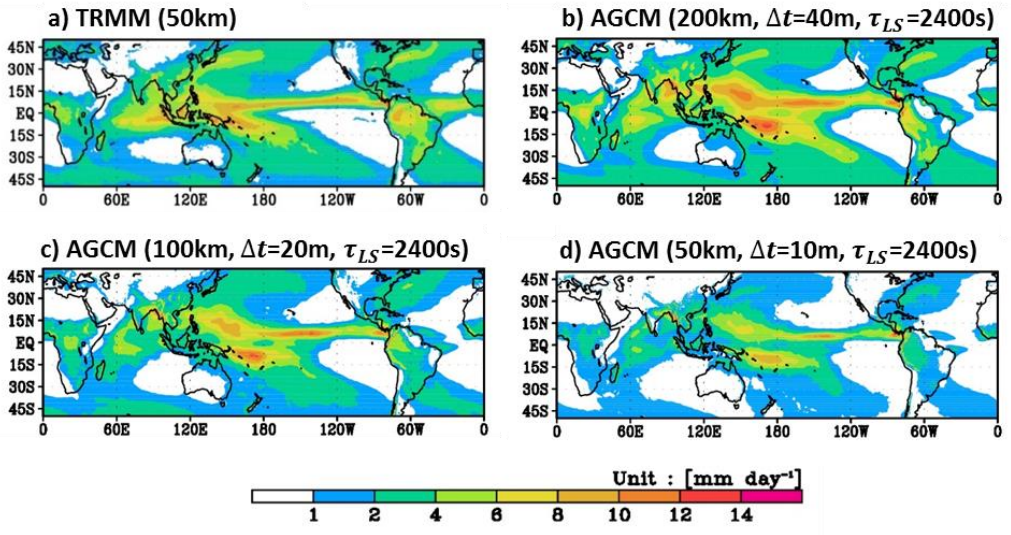

Figure 7.1. Precipitation mean state for a) TRMM, b) AGCM with 200km resolution, c) AGCM with 100km resolution, and d) AGCM with 50km resolution. Δt of 200km, 100km, and 50km simulations are 40 minutes, 20 minutes, and 10 minutes, respectively. Auto-conversion time scale of 200km, 100km, and 50km simulations are same with 2400s. 10 years data used for the TRMM and 5 years data used for the AGCM. TRMM was interpolated to 50km resolution.

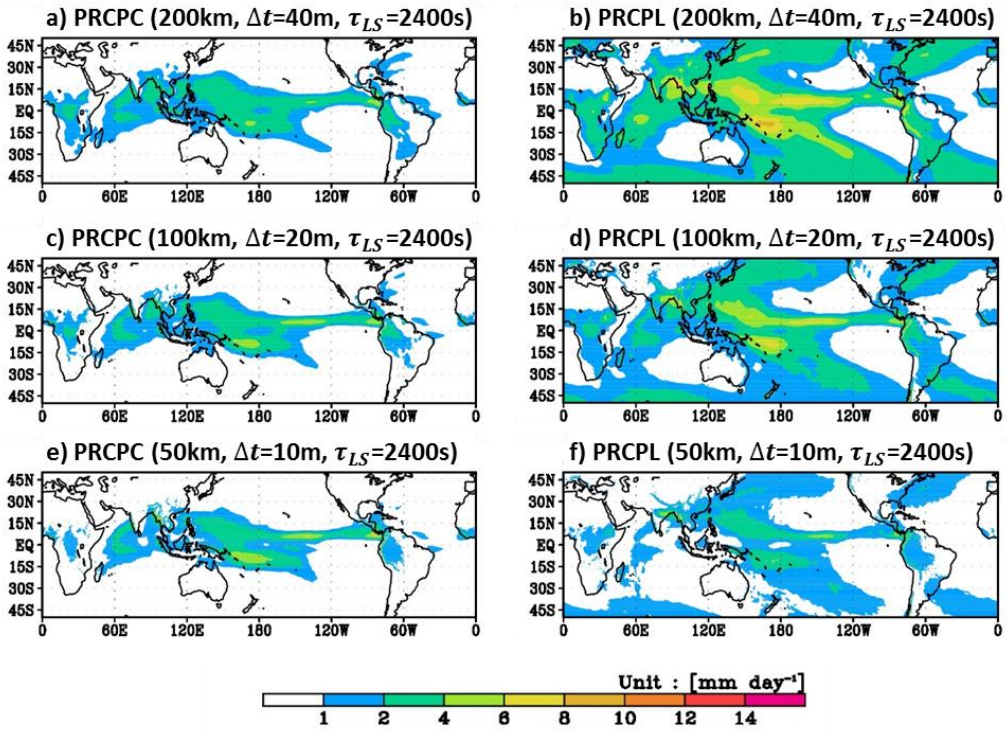

Figure 7.2. Mean state of a),c),e) convective precipitation and b),d),f) large-scale precipitation for a),b) AGCM with 200km resolution, c),d) AGCM with 100km resolution, and e),f) AGCM with 50km resolution. Δt of 200km, 100km, and 50km simulations are 40 minutes, 20 minutes, and 10 minutes, respectively. Auto-conversion time scale of 200km, 100km, and 50km simulations are same with 2400s. 10 years data used for the TRMM and 5 years data used for the AGCM. TRMM was interpolated to 50km resolution.

A key parameter for the large-scale precipitation is the auto-conversion time scale for large-scale condensate. Lau and Wu (2003) presented that the auto-conversion time scale for warm rain is approximately 400-800s based on analysis of TRMM data. In this model, the auto-conversion time scale was fixed as a constant 2400s. Figure 7.3 shows the precipitation mean state for TRMM, AGCM with 200km, 100km, and 50km resolution. Δt of 200km, 100km, and 50km simulations are 40 minutes, 20 minutes, and 10 minutes, respectively. Auto-conversion time scale of 200km, 100km, and 50km simulations are 2400s, 1200s, and 600s, respectively. As the model resolution increases and time step decreases, the precipitation strength does not become weak when the auto-conversion time scale was decreased as the model time step decreases. It indicates that the auto-conversion time scale is important and sensitive parameter for high resolution models. In other words, the auto-conversion time scale can be an uncertainty in parameterization process. Implementation of the comprehensive cloud microphysics to high resolution models is worth approach to reduce the uncertainties in parameterization, such as auto-conversion time scale.

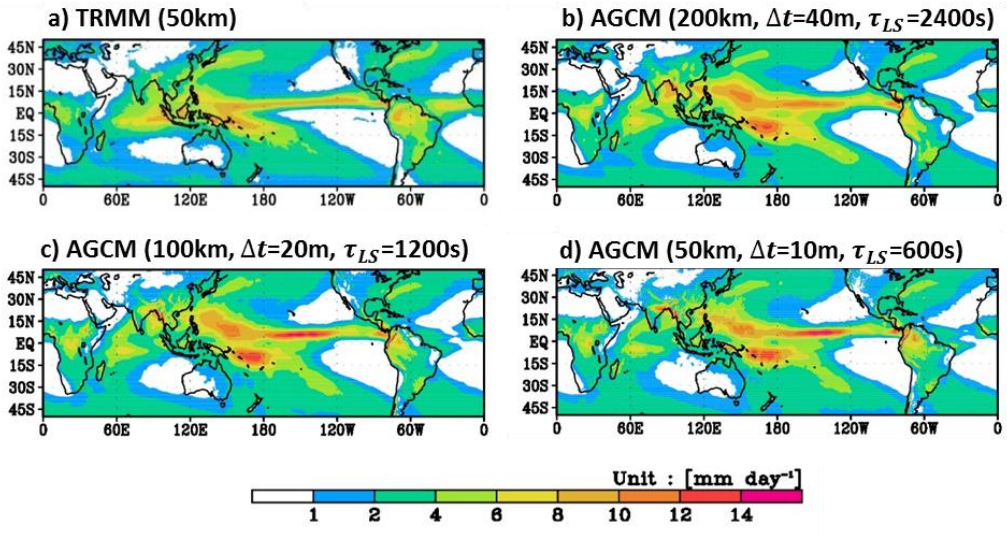

Figure 7.3. Precipitation mean state for a) TRMM, b) AGCM with 200km resolution, c) AGCM with 100km resolution, and d) AGCM with 50km resolution. Δt of 200km, 100km, and 50km simulations are 40 minutes, 20 minutes, and 10 minutes, respectively. Auto-conversion time scale of 200km, 100km, and 50km simulations are 2400s, 1200s, and 600s, respectively. 10 years data used for the TRMM and 5 years data used for the AGCM. TRMM was interpolated to 50km resolution.

7.2.2 Condensation RH criteria

In coarse resolution GCMs (order of 100km), the large-scale condensation is parameterized based on the fractional saturation because the grid-mean RH is rarely exceeded 100%. When grid-mean relative humidity exceeds a criteria value, the fractional saturation occurs. The sub-grid fractional condensation concept is adapted from Le Treut and Li (1991).

$$a_c = \begin{bmatrix} 0 \\ \dfrac{(1+b)\bar{q}_t - \bar{q}^*}{2b\bar{q}_t} \\ 1 \end{bmatrix}, \text{for} \begin{bmatrix} (1+b)\bar{q}_t \le \bar{q}^* \\ (1-b)\bar{q}_t < \bar{q}^* < (1+b)\bar{q}_t \\ (1-b)\bar{q}_t \ge \bar{q}^* \end{bmatrix}$$

$$\bar{q}_c = \begin{bmatrix} 0 \\ a_c\dfrac{(1+b)\bar{q}_t - \bar{q}^*}{2} \\ \bar{q}_t - \bar{q}^* \end{bmatrix}, \text{for} \begin{bmatrix} (1+b)\bar{q}_t \le \bar{q}^* \\ (1-b)\bar{q}_t < \bar{q}^* < (1+b)\bar{q}_t \\ (1-b)\bar{q}_t \ge \bar{q}^* \end{bmatrix}$$

a_c and $\bar{q}_c$ indicate the cloud fraction and cloud water formulated by fractional saturation, respectively. $\bar{q}_t$ and $\bar{q}^*$ indicate the grid-mean total water vapor and saturated grid-mean total water vapor, respectively. b indicates the variation rate of water vapor in a gird.

$$b = \varepsilon\lambda^{-1}\left(\frac{kz}{1+kz/\lambda}\right)$$

ε is constant of variation rate, λ is mixing length (~300m), k is Von Karman constant (~0.4), z is geopotential height.

The ε is a key parameter to control the fractional saturation in this scheme. As the model resolution increases, the ε should be decreased because the high resolution GCMs has possibility to have higher grid-mean relative humidity than low resolution GCMs. Figure 7.4 shows the precipitation mean state for MPAGCM with RHC 80% ($\varepsilon = 0.2$), MPAGCM with RHC 95% ($\varepsilon = 0.05$), and vertical profiles of cloud water from the Cloudsat data and model simulations. Two simulations show similar spatial pattern in the precipitation mean state, but the vertical profile of cloud water is improved in the RHC 95% simulation.

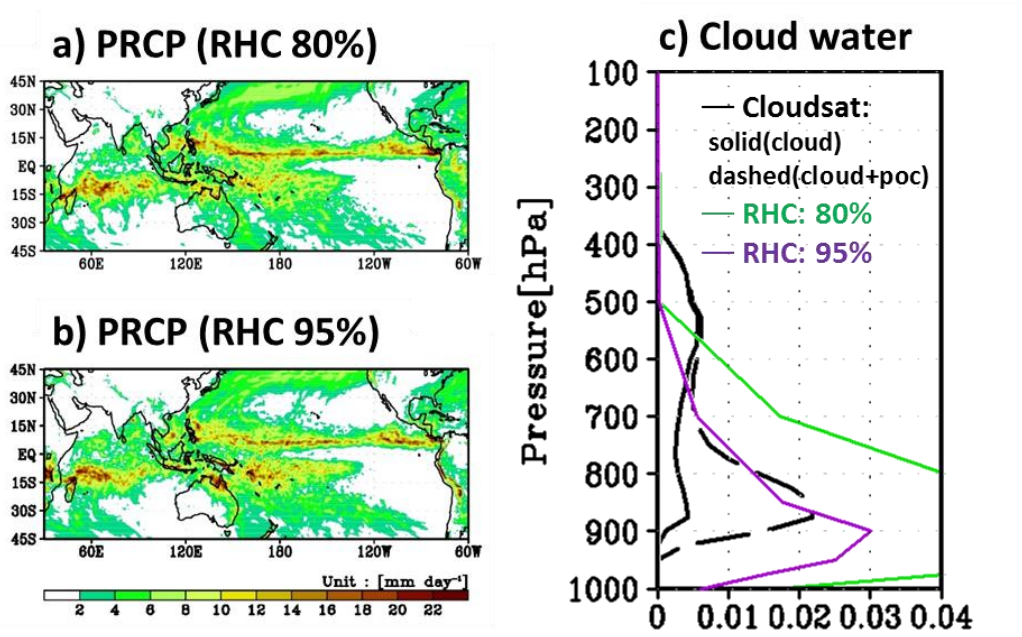

Figure 7.4. Precipitation mean state for a) MPAGCM with RHC 80%, b) MPAGCM with RHC 95%, and c) vertical profiles of cloud water from the Cloudsat data and model simulations. Black solid line in Cloudsat indicates only cloud, and black dashed line indicates cloud plus precipitation or convection.

7.2.3 Grid-mean Cloud microphysics

The cloud microphysics of cloud resolving model does not treat fractional saturation because the horizontal resolution of cloud resolving model is fine enough to explicitly resolve the clouds. The cloud fraction of cloud resolving model is one or zero. For implementation of the cloud microphysics of cloud resolving model to the GCMs, the fractional saturation and cloud fraction should be considered because the GCMs have coarse horizontal resolution.

In conventional GCMs, the state variables (or grid-mean variables) are calculated by dynamics and physics schemes and updated to the next time step. In the GCM with cloud microphysics of cloud resolving model, the cloud microphysics is calculated using the grid-mean variables. However, it was not suitable for original cloud microphysics of cloud resolving model which is developed to be calculated using in-cloud variables. Therefore, the original cloud microphysics is modified to suitable for grid-mean cloud microphysics using modification of terminal velocity.

Another possible method for implementation of cloud microphysics of cloud resolving model to the GCMs is using the in-cloud variables for the cloud microphysics. To make the in-cloud variables in GCMs, the cloud fraction is required, but the parameterization of cloud fraction has uncertainty. Park et al. (2014) presented the method for correction of the parameterized cloud fraction using criteria value of in-cloud variables. However, it still remains as another challenging problem.

References

Arakawa, A., 2004: The cumulus parameterization problem: Past, present, and future. *J. Climate*, 17, 2493–2525.

Arakawa, A. and C. M. Wu, 2013: A unified representation of deep moist convection in numerical modeling of the atmosphere. Part I. *J. Atmos. Sci.*, 70, 1977-1992.

Arakawa, A. and C. M. Wu, 2015: Reply to ''Comments on 'A Unified Representation of Deep Moist Convection in Numerical Modeling of the Atmosphere. Part I'''. *J. Atmos. Sci.*, 72, 2566-2567.

Arakawa, A. and W. H. Schubert, 1974: Interaction of a cumulus cloud ensemble with the large-scale environment. Part I. *J. Atmos. Sci.*, 31, 674–701.

Bernie, D.J., Guilyardi E, Madec G, Slingo JM, Woolnough SJ, Cole J., 2008: Impact of resolving the diurnal cycle in an ocean–atmosphere GCM. part 2: a diurnally coupled CGCM. *Climate Dynamics*, 31, 909-925.

Benedict, J. J., and D. A. Randall, 2009: Structure of the Madden-Julian Oscillation in the Superparameterized CAM. *Journal of Climate*, 66, 3277-3296.

Benedict, J. J., E. D. Maloney, A. H. Sobel, and D. M. W. Frierson, 2014: Gross Moist Stability and MJO Simulation Skill in Three Full-Physics GCMs. *Journal of the Atmospheric Sciences*, **71,** 3327-3349.

Bonan, G.B., 1996: Land surface model (LSM version 1.0) for ecological, hydrological, and atmospheric studies: technical description and user's guide, *NCAR Technical Note NCAR/TN-417+STR*, 1-159.

Boyle, J., Klein SA. 2010: Impact of horizontal resolution on climate model forecasts of tropical precipitation and diabatic heating for the TWP-

ICE period. *Journal of Geophysical Research*, 115, 1–20.

Bretherton, C. S., P. N. Blossey, and M. Khairoutdinov, 2005: An energy-balance analysis of deep convective self-aggregation above uniform SST, *J. Atmos. Sci.*, 62, 4273–4292.

Chen, C.-T., Knutson T. 2008: On the verification and comparison of extreme rainfall indices from climate models *Journal of Climate*, 21, 1605–1621.

Chikira, M., and M. Sugiyama, 2010: A cumulus parameterization with state-dependent entrainment rate. Part I: Description and sensitivity to temperature and humidity profiles. *J. Atmos. Sci.*, 67, 2171–2193.

Dai, A., 2006: Precipitation characteristics in eighteen coupled climate models. *Journal of Climate*, **19**, 4605–4630.

Danabasoglu, G., Large WG., Tribbia JJ, Gent PR, Briegleb BP, McWilliams JC., 2006: Diurnal coupling in the tropical oceans of CCSM3. *Journal of Climate*, 19, 2347–2365.

DeMott, C. A., D. A. Randall, and M. Khairoutdinov. 2007: Convective precipitation variability as a tool for general circulation model analysis. *Journal of Climate*, 20, 91-112.

Grabowski, WW. 2001: Coupling cloud processes with the large-scale dynamics using the cloud-resolving convection parameterization (CRCP). *Journal of Atmospheric Science*, 68, 978-997.

Gregory, D., and P. R. Rowntree, 1990: A mass flux convection scheme with representation of cloud ensemble characteristics and stability dependent closure. *Mon. Wea. Rev.*, 118, 1483–1506.

Hayashi, Y., 1982: Space-time spectral analysis and its applications to atmospheric waves. *J. Meteor. Soc. Japan*, **60,** 156–171.

Ham, Yoo-Geun, Jong-Seong Kug, In-Sik Kang, Fei-Fei Jin, and Axel Timmermann, 2010: Impact of diurnal atmosphere-ocean coupling

on tropical climate simulations using a coupled GCM. *Climate Dynamics*, 34, 905-917.

Held, I. M., R. S. Hemler, and V. Ramaswamy, 1993: Radiative-convective equilibrium with explicit two-dimensional moist convection, *J. Atmos. Sci.*, 50, 3909–3927.

Hendon, H. H., C. Zhang, and J. D. Glick, 1999: Interannual variation of the Madden–Julian oscillation during austral summer. *J. Climate*, **12**, 2538–2550.

Holtslag, A., and B. Boville, 1993: Local versus nonlocal boundary-layer diffusion in a global climate model. *Journal of Climate*, 6, 1825-1825.

Hung, M.-P., J.-L. Lin, W. Wang, D. Kim, T. Shinoda, and S. J. Weaver, 2013: MJO and convectively coupled equatorial waves simulated by CMIP5 climate models. *J. Climate*, **26**, 6185–6214.

Iorio, J., Duffy P., Govindasamy B., Thompson S., Khairoutdinov M., Randall D., 2004: Effects of model resolution and subgrid-scale physics on the simulation of precipitation in the continental United States. *Climate Dynamics*, 23, 243–258.

Jiang, X., and Coauthors, 2015: Vertical structure and physical processes of the Madden-Julian oscillation: Exploring key model physics in climate simulations. *Journal of Geophysical Research: Atmospheres*, **120**, 4718–4748.

Kang, In-Sik, Young-Min Yang, Wei-Kuo Tao, 2015: GCMs with implicit and explicit representation of cloud microphysics for simulation of extreme precipitation frequency. *Climate Dynamics*, 45, 1-2, 325-335.

Kang, In-Sik, Min-Seop Ahn, Young-Min Yang, 2016: A GCM with cloud microphysics and its MJO simulation. *Geoscience Letters*, 3, 16.

Khairoutdinov, M., and K. Emanuel, 2013: Rotating radiative-convective

equilibrium simulated by a cloud-resolving model, *J. Adv. Model. Earth Syst.*, 5, 816–825.

Kim, D., and Coauthors, 2009: Application of MJO simulation diagnostics to climate models. J. Climate, **22**, 6413–6436.

Kim, D., and Coauthors, 2014: Process-Oriented MJO Simulation Diagnostic: Moisture Sensitivity of Simulated Convection. *Journal of Climate*, **27,** 5379-5395.

Kim, D., Kug J.-S., Kang I.-S., Jin F.-F., Wittenberg AT, 2008: Tropical momentum transport in the SNU coupled GCM. *Climate Dynamics*, 31, 213-226.

Kim, D., Kang I.-S., 2012: A bulk mass flux convection scheme for climate model: description and moisture sensitivity. *Climate Dynamics*, 38, 411–429.

Kim, D., M.-S. Ahn, I.-S. Kang, and A. D. Del Genio, 2015: Role of Longwave Cloud–Radiation Feedback in the Simulation of the Madden–Julian Oscillation. *Journal of Climate*, **28,** 6979-6994.

Klemp, J.B., Wilhelmson R.B., 1978: The simulation of three-dimensional convective storm dynamics. *J. Atmos. Sci.,* 35, 1070-1096.

Kuo, Y. J., 1974: Further studies of the parameterization of the influence of cumulus convection on large-scale flow. *J. Atmos. Sci.*, 31, 1232–1240.

Kwon, Y., and S. Hong, 2016: A mass-flux cumulus parameterization scheme across gray-zone resolutions. *Mon. Wea. Rev.* doi:10.1175/MWR-D-16-0034.1, in press.

Lau, K. M., and H. T. Wu, 2003: Warm rain processes over tropical oceans and climate implications, *Geophys. Res. Lett.*, 30(24), 2290.

Lau, K. M., Sui CH., Tao W.-K., 1993: A preliminary study of the tropical water cycle and its sensitivity to surface warming. *Bull Amer Meteor Soc*, 74, 1313–1321.

Le Treut, H., and Z.-X. Li., 1991: Sensitivity of an atmospheric general circulation model to prescribed SST changes: feedback effects associated with the simulation of cloud optical properties. *Climate Dynamics*, 5, 175-187.

Li, F., Rosa D., Collins W.D., Wehner MF, 2012: "Super-parameterization": a better way to simulate regional extreme precipitation? *Journal of Advances in Modeling Earth Systems*, 4, 1–10.

Lin, J,-L., and Coauthors, 2006: Tropical intraseasonal variability in 14 IPCC AR4 climate models. Part I: Convective signals. *Journal of Climate*, **19**, 2665–2690.

Lin, S.-J., 2004: A "vertically Lagrangian" finite-volume dynamical core for global models, *Mon. Weather Rev.*, 132, 2293-2307.

Lin, Y.-L., Farley RD, Orville HD., 1983: Bulk parameterization of the snow field in a cloud model. *J. Clim. and Appl. Meteorol.*, 22, 1065-1092.

Liu P, Satoh M, Wang B, Fudeyasu H, Nasuno T, Li T, Miura H, Taniguchi H, Masunaga H, Fu X. 2009: An MJO simulated by the NICAM at 14- and 7-km resolutions, *Monthly Weather Review*, 137, 3254-3268.

Lorant, V., N. A. McFarlane, and J. F. Scinocca. 2006: Variability of precipitation intensity: sensitivity to treatment of moist convection in an RCM and a GCM. *Climate dynamics*, 26, 183-200.

Manabe, S., J. Smagorinsky, and R. F. Strickler, 1965: Simulated climatology of a general circulation model with a hydrological cycle. *Mon. Wea. Rev.*, 93, 769–798.

Miura, H., Satoh M, Nasuno T, Noda AT, Oouchi K. 2007: A Madden-Julian oscillation event realistically simulated by a global cloud-resolving model, *Science*, 318, 1763-1765.

MJOWG, 2009: MJO simulation diagnostics, Journal of Climate, **22**, 3006–3030.

Moorthi, S., and M. J. Suarez, 1992: Relaxed Arakawa–Schubert: A parameterization of moist convection for general circulation models. *Mon. Wea. Rev.*, 120, 978–1002.

Muller, C. J., and I. M. Held, 2012:, Detailed investigation of the selfaggregation of convection in cloud-resolving simulations, *J. Atmos. Sci.*, 69, 2551–2565.

Nakajima, T., Tsukamoto M, Tsushima Y, Numaguti A., 1995: Modelling of the radiative processes in an AGCM. *Clim Syst Dyn Model*, 3, 104–123

Noh, Y., Kim HJ., 1999: Simulations of temperature and turbulence structure of the oceanic boundary layer with the improved nearsurface process. *Journal of Geophysical Research*, 104, 15621–15634.

Oouchi, K., A.T. Noda, M. Satoh, H. Miura, H. Tomita. T. Nasuno, S. Iga., 2009: A simulated preconditioning of typhoon genesis controlled by a boreal summer Madden-Julian Oscillation event in a global cloud-system-resolving model. *SOLA*, 5, 065-068.

Pan, D. M., and D. A. Randall, 1998: A cumulus parameterization with a prognostic closure. *Quart. J. Roy. Meteor. Soc.*, 124, 949–981.

Park, S., Bretherton C.S., Rasch P.J., 2014: Integrating cloud processes in the Community Atmosphere Model, version 5. *Journal of Climate*, **27**, 6821–6856.

Rutledge, S. A., and P. Hobbs, 1983: The Mesoscale and Microscale Structure and Organization of Clouds and Precipitation in Midlatitude Cyclones. VIII: A Model for the "Seeder-Feeder" Process in Warm-Frontal Rainbands. *Journal of the Atmospheric Sciences*, **40,** 1185-1206.

Rutledge, S. A., and P. V. Hobbs, 1984: The Mesoscale and Microscale Structure and Organization of Clouds and Precipitation in Midlatitude Cyclones. XII: A Diagnostic Modeling Study of Precipitation Development in Narrow Cold-Frontal Rainbands. *Journal of the*

Atmospheric Sciences, **41,** 2949-2972.

Salby, M. L., and H. H. Hendon, 1994: Intraseasonal behavior of clouds, temperature, and motion in the Tropics. *J. Atmos. Sci.*, **51**, 2207–2224.

Satoh, M., Tomita H, Miura H, Iga S, Nasuno T. 2005: Development of a global cloud resolving model-a multi-scale structure of tropical convections. *Journal of the Earth Simulator*, 3, 11–19.

Scala, J.R., Garstang M., Tao W.-K., Pickering KE., Thompson AM., Simpson J., Kirchoff VWJH., Browell EV., Saschse GW., Torres AL., Gregory GL., Rasmussen RA., Khalil MAK., 1990: Cloud draft structure and trace gas transport. *Journal of Geophysical Research*, 95, 17015–17030.

Sperber, K. R., D. Kim, 2012: Simplified metrics for the identification of the Madden–Julian oscillation in models. *Atmos. Sci. Let.*, **13,** 187-193.

Su, H., Jiang J.H., Vane D.G., Stephens G.L., 2008: Observed vertical structure of tropical oceanic clouds sorted in large-scale regimes. *Geophysical Research Letters*, **35**, 1–6.

Sun, Y, Solomon S, Dai A, Portmann RW, 2006: How often does it rain? *Journal of Climate*, **19**, 916–934.

Tao, W.-K., Simpson J., 1984: Cloud interactions and merging: Numerical simulations. *Journal of Atmospheric Science*, 41, 2901–2917.

Tao, W.-K., Soong S.-T., 1986: A study of the response of deep tropical clouds to mesoscale processes: Three-dimensional numerical experiments. *Journal of Atmospheric Science*, 43, 2653–2676.

Tao, W.-K., Simpson J., 1989: A further study of cumulus interaction and mergers: Three-dimensional simulations with trajectory analyses. *Journal of Atmospheric Science*, 46, 2974–3004.

Tao, W.-K., J. Simpson, C.-H. Sui, C.-L. Shie, B. Zhou, K. M. Lau, and M. Moncrieff, 1999: Equilibrium states simulated by cloudresolving

models, *J. Atmos. Sci.*, 56, 3128–3139.

Tao, W.-K., Simpson J., Soong S.-T., 1991: Numerical simulation of a subtropical squall line over Taiwan Strait. *Mon Wea Rev*, 119, 2699–2723.

Tao, W.-K., and J. Simpson, 1993: The Goddard Cumulus Ensemble Model. Part I: Model description. Terrestrial, *Atmospheric and Oceanic Sciences*, **4**, 35-72.

Tao, W-K, Simpson J, Baker D, Braun S, Chou M-D, Ferrier B, Johnson D, Khain A, Lang S, Lynn B., 2003: Microphysics, radiation and surface processes in the Goddard Cumulus Ensemble (GCE) model, *Meteorol. and Atmos. Phys.*, 82, 97-137.

Tiedtke, M., 1984: The sensitivity of the time-mean large-scale flow to cumulus convection in the ECMWF model. *ECMWF Workshop on Convection in large-scale Models*, 297-316.

Tiedtke, M., 1989: A comprehensive mass flux scheme for cumulus parameterization in large-scale models. *Monthly Weather Review*, **117**, 1779–1800.

Taylor, K. E., R. J. Stouffer, and G. A. Meehl, 2012: An Overview of CMIP5 and the Experiment Design. *Bulletin of the American Meteorological Society*, **93,** 485-498.

Wehner, MF, Smith RL, Bala G, Duffy P. 2010: The effect of horizontal resolution on simulation of very extreme US precipitation events in a global atmosphere model. *Climate Dynamics*, 34, 241–247.

Wheeler, M., and G. N. Kiladis, 1999: Convectively coupled equatorial waves: Analysis of clouds and temperature in the wavenumber–frequency domain. J. Atmos. Sci., **56**, 374–399.

Wheeler, M. C., and H. H. Hendon, 2004: An all-season real-time multivariate MJO index: Development of an index for monitoring and prediction.

Mon. Weather Rev., **132,** 1917-1932.

Wilcox, E.M. and Donner LJ. 2007: The frequency of extreme rain events in satellite rain-rate estimates and an atmospheric general circulation model. *Journal of Climate*, 20, 53–69.

Yang, Young-Min, 2014: Development of a high resolution GCM with cloud microphysics and its impact on simulation of tropical precipitation. Ph.D. thesis in Seoul National University.

Yasunaga, K., and B. Mapes, 2012: Differences between more divergent and more rotational types of convectively coupled equatorial waves. Part I: Space–time spectral analyses. *J. Atmos. Sci.*, **69**, 3–16.

Zhang, C., and H. H. Hendon, 1997: Propagating and standing components of the intraseasonal oscillation in tropical convection. *J. Atmos. Sci.*, **54**, 741–752.

Zhang, C., M. Dong, S. Gualdi, H. H. Hendon, E. D. Maloney, A. Marshall, K. R. Sperber, and W. Q. Wang, 2006: Simulations of the Madden-Julian oscillation in four pairs of coupled and uncoupled global models, *Clim. Dyn.*, **27**, 573–592.

Zhang, G. J., and N. A. McFarlane, 1995: Sensitivity of climate simulations to the parameterization of cumulus convection in the Canadian Climate Center general circulation model. *Atmos.–Ocean*, 33, 407–446.

Zhang, G. J., J. Fan, and K.-M. Xu, 2015: Comments on ''A unified representation of deep moist convection in numerical modeling of the atmosphere. Part I.'' *J. Atmos. Sci.*, 72, 2562–2565.

Zhu, H., H. Hendon, and C. Jakob. 2009: Convection in a parameterized and superparameterized model and its role in the representation of the MJO. *Journal of the atmospheric sciences*, 66, 2796-2811.

국문 초록

본 연구의 주요목표는 50㎞ 해상도 전지구기후모형에 포괄적인 구름미세물리과정과 그에 적합한 연직혼합과정을 접합하는 것이다. 포괄적인 구름미세물리과정은 구름분해모형의 한 종류인 Goddard Cumulus Ensemble (GCE) 모형의 것을 도입하였다. 구름미세물리과정을 전지구기후모형에 적용하기위해 구름미세물리과정의 해상도종속성을 파악하였고, 부분적응결방법과 낙하종속도의 조절을 통해 구름미세물리과정의 해상도종속성을 완화시켰다.

50㎞ 해상도 전지구기후모형에 적합한 연직혼합과정을 이해하기 위해 대기대순환모형에서 다른 수평해상도를 가지는 실험들과 3차원 구름분해모형의 실험을 통해서 분석을 하였다. 대기대순환모형의 수평해상도가 증가함에 따라 명시적으로 계산되는 격자 규모 연직혼합과정이 증가하였다. 따라서, 이에 적합하도록 대류적운모수화를 통해 만들어지는 아격자 규모 연직혼합과정은 줄어들어야 한다. 3차원 구름분해모형의 1㎞ 수평 해상도 실험으로 모형의 수평해상도가 변함에 따라 전체 연직혼합과정중에 아격자규모 연직혼합과정이 차지하는 비율의 변화를 분석하였다. 3차원 구름분해모형실험을 통해 얻은 전체 연직혼합과정중에 아격자규모 연직혼합과정이 차지하는 비율은 대기대순환모형에서 모수화된 아격자규모 연직혼합과정을 적절하게 줄이는데 기준이 되는 값으로 사용되었다. 적운기저질량속은 모수화된

아격자규모 연직혼합과정을 적절하게 줄이는데 제어 변수로 사용되었다.

포괄적인 구름미세물리과정과 적합한 연직혼합과정을 접합시킨 50km 해상도 전지구기후모형에서 온도와 습도의 연직 구조, 강수 강도에 따른 빈도수, Madden-Julian Oscillation (MJO) 의 모의가 향상되었다. MJO 전문위원회 (MJOWG/MJOTF) 에서 개발된 MJO모의 진단 방법과 MJO모의에 주요한 영향을 미치는 과정들에 기반한 진단 방법이 본 연구를 통해서 개발된 모형에 적용되어 분석 되었고, 제 5차 대기해양접합모형 비교분석 프로젝트 (CMIP5)에 참여한 모형들과도 비교분석 되었다. 본 연구를 통해서 개발된 모형은 MJO 전파, 대류-수분 결합, 장파복사 되먹임 과정에서 향상을 가져왔다.

주요어:

고해상도 전지구기후모델링, 전지구기후모형, 구름분해모형, 구름미세물리과정, 규모-적응 모수화, Madden-Julian 진동

학 번: 2012-30894